ISTANBUL TECHNICAL UNIVERSITY ★ GRADUATE SCHOOL OF SCIENCE ENGINEERING AND TECHNOLOGY

MEMS Based Clamped-Clamped Resonant Magnetometer

M.Sc. THESIS by
Omid TAYEFEH GHALEHBEYGI

Department : **Electronics & Telecommunication Engineering**

Program : **Electronics Engineering**

Thesis Supervisor : **Assoc. Dr. Levent TRABZON**

December 2012

ISTANBUL TECHNICAL UNIVERSITY ★ GRADUATE SCHOOL OF SCIENCE ENGINEERING AND TECHNOLOGY

MEMS Based Clamped-Clamped Resonant Magnetometer

M.Sc. THESIS by
Omid TAYEFEH GHALEHBEYGI
(504091253)

Date of submission: **25th September 2012**
Date of defence examination: **18th December 2012**

Supervisor: **Assoc. Dr. Levent TRABZON**
Members of the examining committee: **Prof. Dr. Ali TOKER**
Assoc. Dr. Hüseyin KIZIL

December 2012

İSTANBUL TEKNİK ÜNİVERSİTESİ ★ FEN BİLİMLERİ ENSTİTÜSÜ

MEMS'e Bağlı olan rezonant magnetik ölçen sensorı

YÜKSEK LİSANS TEZİ
Omid TAYEFEH GHALEHBEYGI
(504091253)

Tezin Enstitüye Verildiği Tarih : 25 Eylul 2012
Tezin Savunulduğu Tarih : 18 Aralık 2012

Tez Danışmanı : Assoc. Dr. Levent TRABZON
Diğer Jüri Üyeleri : Prof. Dr. Ali TOKER
Assoc. Dr. Hüseyin KIZIL

ARALIK 2012

Omid Tayefeh Ghalehbeygi, a **M.Sc.** student of ITU **Graduate School of Science Engineering and Technology** student ID 504091253, successfully defended the **Master thesis** entitled "**MEMS Based Clamped-Clamped Resonant Magnetometer**", which he prepared after fulfilling the requirements specified in the associated legislations, before the jury whose signatures are below.

Thesis Advisor:	**Assoc. Dr. Levent TRABZON** İstanbul Technical University	....
Jury Members :	**Prof. Dr. Ali Toker** İstanbul Technical University	....
	Assoc. Dr. Hüseyin Kızıl İstanbul Technical University	....

Date of Submission: 25th September 2012
Date of Defense: 18th December 2012

To my Family,

ACKNOWLEDGEMENT

At first, I would like appreciate from my precious parents and invaluable brothers: Mahmud, Majid and Vahid who never left me alone and always support me whether financially or spiritually in every moment of my life. Also, I would like to say thanks a lot to my generous uncles Shamsaldin and Nuraldin Banaeinegad that with their suggestions and pay attention to my demands and decisions accompany me everywhere.

In addition, I would like to appreciate from persons that without of their presence I never overcame problems which has been along Master period. Hereby I would like to express my deep appreciation to my supervisor in Istanbul Technical University, dear Prof. Levent TRABZON, who did me a lot of favors and my thesis's advisor dear Prof. Laurent FRANCIS, who accepted me as his student to do my thesis under his supervision and especial thanks to Mr. Christian RENAUX and Dr. Petros Gkotsis who learned me a lot of things about cleanroom's rules and working with various devices and simulation softwares.

At the end, I would like really appreciate from everyone and specifically my dear friends in Turkey and Belgium, whom without of their favors, lonely I would not be able to overcome obstacles throughout these years.

September 2012

Omid TAYEFEH
GHALEHBEYGI
(Electronics Engineering)

TABLE OF CONTENTS

Page

ABBREVIATIONS

MEMS	**:** Micro-Electro Mechanical Systems
UCL	**:** Universite Catholique de Louvain
ABS	**:** Automotive anti-skid Breaking System
SQUID	**:** Superconducting Quantum Interference Device
RF	**:** Radio Frequency
AMR	**:** Anisotropic Magnetoresistance
GMR	**:** Giant Magnetoresistance
TMR	**:** Tunneling Magnetoresistance
SDT	**:** Spin-Dependent Tunneling
XBM	**:** Xylophone Bar Magnetometer
SEM	**:** Scanning Electron Microscope
TED	**:** Thermo-Elastic Damping
SOI	: Silicon-On-Insulator
LPCVD	: Low-Pressure Chemical Vapor Deposition
PECVD	: Plasma-Enhanced Chemical Vapor Deposition
CPD	: Critical Point Dryer

LIST OF TABLES

LIST OF FIGURES

Page

z

MEMS based Clamped-Clamped resonant Magnetometer

SUMMARY

This thesis explains the new and several designing membrane and beams, which have been designed by ourselves by cadence software. Furthermore, all of the structures were fabricated by MEMS-based, which are CMOS compatible characteristics.

In the beginning, by using of Cadence 3 numbers of masks were designed. First mask was designed to shape active layer. Second one is considered to metallization step and third one which was dark mask, was designed to be used in etching part, particularly when etching method was BHF release.

Each sample has been designed at different dimension, in view of length, width of membrane with the same thickness and various sizes of perforations, which have been allocated for etching purpose. The lengths of the resonators were designed in 10, 20, 30, 50, and 100 micrometer and for each specific ones the beam's width has been changed as follow 3, 5, 10, 20, 30, 40, 50, 60, 90, 100 micrometer. Finally 438 individual samples have been designed which surrounded in rectangular with 6.12 × 7.7mm2.

In fabrication part, initially, we implement our fabrication at first on bulk with depositing 80 nm polysilicon on oxidation layer which is used as insulator layer and sacrificial layer at end of process. After that, to reduce resistivity of polysilicon, phosphorous was doped in stove with 900˚C temperature for 30 minutes to reach 190 Ω/sq resistivity. We used many devices to calculate some properties of the each layer such as intrinsic stress. by finishing of this type of sensors we noticed that polysilicon could not be used because of the compressive stress, which is produced after doping of phosphorous. Because after etching all of the membranes or beams are buckled. Therefore, to overcome solving this problem, SOI wafer preferred due to the tensile stress was produced after doping phosphorous for an hour in 900˚C to reach 40 Ω/sq resistivity.

In this study, in order to etch polysilicon HF was utilized and for single crystal silicon (SOI-wafer) BHF (Buffered HF) was used. For drying these suspended structures with avoiding surface tension – the reason of the bending – we used from critical point drying (CPD) device.

This principle of working of this devise is depending on the properties of CO_2. To obtain the critical point of carbon dioxide, 31.1 ˚C temperature and 1072-psi pressure is required. With reaching CO_2 to this point of physical state, the interaction between suspended structures the environment adhesion become zero and beams stand straight.

Also along the fabrication most of the sensors has been simulated by two softwares COMSOL and Coventorware that in both of them simulation is done by finite element method (FEM). During the simulation many behavior of the each structure such as natural frequency, maximum current endurance before smashing, and their displacements, with and without of the initial stress and effect of the dimension of the perforation were defined.

For investigating first mode frequency, with varying four parameters of structures, their effects were demonstrated. At first, by fixing all parameters except beam's length, its effect on first mode resonance was examined. For instance at fixed 3 µm beam's width, for 10, 20, 30, 50, 100 µm beam's length their first mode resonance frequency became 12.6, 3.14, 1.39, 0.49, and 0.12 MHz, respectively. At second step, we tried to show that by changing beam's width, but fixing their length and perforation size, first mode resonance frequency did not differ. For example, for membrane with 30 µm length and 2.062 µm × 2 µm perforation sizes, by changing their beam's width from 5, 30, and 50 µm, their frequencies became unchanged around 1.36 MHz.

At third step, the effects of the perforation's size in two direction of beam on first mode resonance frequency were investigated. For instance, in beam with 100 µm length of beam × 50 µm width of beam samples, only by increasing perforation side which are rectangular at length direction of beam; 2.018 µm × 10.625 µm, 3/972 µm × 10.625 µm, and 10.813 µm × 10.625 µm, first mode resonance frequencies were shifted to higher frequencies 8.22×10^4 Hz, 9.21×10^4 Hz, and 1.32×10^5 Hz respectively. On the contrary, for samples with 50 µm length of beam × 100 µm width of beam, by increasing perforation side in width direction of beam; 2.062 µm × 2.018 µm, 2.062 µm × 3.972 µm, 2.062 µm × 10.813 µm, and 2.062 µm × 31.334 µm, first mode resonance frequencies were shifted to lower frequencies 1.38 MHz, 1.25 MHz, 0.915 MHz, and 0.515 MHz respectively.

At fourth step, the effect of built-in stress was probed on first mode resonance frequency. This effect only might be investigated on SOI wafer due to the positive value of stress. We can observe its effect on simplest beams, where without token into account of stress their first mode resonance frequencies were 12.6 MHz, 3.1 MHz, 1.4 MHz, 0.49 MHz, 0.12 MHz and for same samples with applying stress became 16.2 MHz, 5.9 MHz, 3.7 MHz, 2.1 MHz, and 1.05 MHz respectively.

For second main simulation, we did it on quality factor of structures on first resonance frequency of each sample. Here, simulation of quality factor of sensors was investigated in two condition; ambient pressure (1 bar) and vacuum pressure (1.4 millitorr). From the results of the simulations we can understand that why these types of sensors should be implemented in vacuum condition. Because as it is seen, for samples with 3 µm width and 10, 20, 30, 50, 100 µm beam's length, quality factors of theses sensors in ambient pressure were 37, 9, 6, 14, 5 and in vacuum pressure became 1.44×10^4, 1.12×10^5, 6.54×10^4, 3.07×10^4, and 2.37×10^4 respectively.

Another simulation was carried out to estimate maximum applicable current of each sample before collapsing. There are two limitations for surmising maximum current value, failure stress of silicon is 300 MPa and melting point of silicon is 1690˚C. Therefore, with increasing current flow when it crosses from one of these limitations we say this is maximum applicable current. This simulation implemented like first mode resonance frequency in all possible geometry of structures. For example, only with increasing beam's length for 3 µm fixed beam's width as follow 10, 20, 30, 50, 100 µm samples, maximum applicable currents are decreased 12.2, 6.8, 4.6, 2.8, and 1.4 mA respectively.

At same beam's length 30 µm and perforation size 2.062 µm × 2 µm, with increasing beam's width 5, 30, 50, 100 µm, maximum applicable currents are increased 4.7, 6.5, 27, 53 mA respectively. Eventually by fixing beam's size and by increasing perforation side in length direction of beam, this value of current is increased too and on opposite side in width direction of beam, it is decreased.

As end section of simulation, the dynamic force and static force on samples versus displacement were investigated. Obviously, for longer beams, amount of deflection is high and for identical samples in view of dimension, unrelated to their perforation size or direction, it is completely related to their masses. Lower weight structures have higher displacement clearly.

Finally, we implement practical measurement with Polytec 500 device to compare outputs with simulation results. The principle of working of this devise is on base of Doppler velocimetry and interfering waves. After comparing we noticed that, there is a common result between them on amount of first mode resonance frequency. On the other hand, there are some differences between them on displacement amount and quality factor due to the environment casual noise during measurement, some damping which were not included during simulation or heterogeny of under etching of anchor parts. For example, at 100 µm length × 100 µm width sample both of the results from simulation and practical outcomes exhibited first resonance frequency around 8×10^5 Hz, but for 0.15 nN force, displacement at simulation is 0.2 µm and in experimental is 2.3nm.

In conclusion, we investigated each sample's features such as; first mode resonance frequency, maximum applicable current, quality factor and displacement versus sample's geometric and their inside perforation size. Thus, we have lots of data, which can be utilized in future for similar sensors to have an idea about their probable features.

MEMS'e Bağlı olan rezonant magnetik ölçen sensorı

ÖZET

Bu çalışmanın amacı, çift tarafdan kenetlenmiş rezonans manyetik sensorların mikro veya nano boyutlarda üretim teknoloji yöntemlerinin incelenmesidir. Bu tez kapsamında, monolitik üretim teknolojisi içinde CMOS devre yapısına uyumlu, çeşitli MEMS sistemlerinin tasarımları, üretimleri ve simülasyonları yapılmıştır. Üretilen Mikrosistemlerin mekanik ve elektriksel karakterizasyonları da tamamlanmıştır.

İlk olarak Cadence yazılımı kullanılarak üç farkı maske tasarlanmıştır. İki maske pozitif (Light) maske ve biri negatif (Dark) maske olarak. 1. maske, aktif katmanın (silisyum ya da polisilisyum) şekillendirmesi için tasarlanmış. 2. maske metalizasyon (metal kaplama) yapmak için – 600 nm Alüminyum – kullanıldı. 3. Maske de aşındırma işleminde yöne bağlı olarak kullanıldı. BHF (Buffered Hidtoflorik Asit) kullanıldığında 3. Maske kullanılır, ama HF (Hidroflorik asit) ile işlemi yaptığınızda bu maskeye gerek kalmaz. Çünkü, Alüminyum, Al, BHF tarafından aşındırılır, fakat HF Al için etki etmez. Bu yüzden, 3. Maske kullandığında, çubukların üzeri hariç Si-pulun her tarafı fotoresist ile kaplandı.

Çalışma kapsamındaki MEMS yapılarından farklı geometrik boyutlarda (en ve uzunluk) fakat aynı kalınlıkta sensörler tasarlanmıştır. Aşındırma işleminin etkin ve verimli yapılabilmesi için çubuklar üzerinde delikler oluşturulmuştur. Sensörlerin boyları 10, 20, 30, 50, ve 100 µm olmak üzere her bir farklı uzunluk için farklı genişlik tasarlandı. 10 µm boya sahip çubuklar için 3, 5, 10, 20, 30, 40, 60 µm genişlikler, 20 µm boya sahip çubuklar için 3, 5, 10, 20, 30, 50, 90 µm genişlikler, 30 µm boya sahip çubuklar için 3, 5, 10, 20, 30, 50, 100 µm genişlikler, 50 µm boya sahip çubuklar için 3, 5, 10, 30, 50, 100 µm genişlikler, ve 100 µm boya sahip çubuklar için 3, 5, 10, 30, 50, 100 µm genişlikler genişlikler tasarlandı. Her bir ayrı uzunluk ve enli çubuklar için farklı boylarda aşındırma delikler tasarlandı ki, toplamda 438 adet farklı mikroyapı tasarlanıp üretildi. Her birinin toplam alanı 6,12x7,7 mm2'lik alana sığdırıldı.

Üretim iki farklı Si-pul (Si-wafer) kullanılarak gerçekleştirildi. Tek kristal ve SOI (Silicon-on-Insulator) türü Si-pullar üretimde kullanıldı. İlk olarak tek kristal Si-pulu üzerinde 400nm oksit tabakası büyütüldü, sonraki adımda 80nm Poly-Si kaplandı. Polisilisyum dirençini azaltmak için fosfor doplaması (doping) edildi ve 30 dakka içinde 900˚C sıcaklığında direnci 190 Ω/sq oldu. Bu esnada doping den önce ve sonra profilometre cihazindan kullanarak polisilisyumun eğrilik yarıçapını ölçerek, stres yüklenmesi hesaplandı. Heba oksidi aşındırıldıktan sonra, Poly-Si üzerinde oluşan kalıntı gerilmeler, negatif stres olduğu için basma stresidir ve Poli-Si kirişlerinde kalıcı deformasyonlara sebep olur. Bu yüzden, üretimde bu yaklaşım bırakılarak, SOI Si-pulu tercih edildi.

SOI kullanılarak geliştirilen proseste, ilk başta direncini azaltmak için fosfor doplaması yapıldı, ve 60 dakikada 900˚C sıcaklığında tavlanarak direnci 40 Ω/sq eld edildi. Profilmetreden ölçülen değerleri kullanarak, gerilmenin pozitif olduğu belirlendi ve bu da kalıcı deformasyonu ortandan kaldırarak, mikrosistemler üretildi.

Bu çalışmada, Polisilisyumu aşındırmak için HF ve tek kristal Silisyum (SOI-pulu) için BHF (Buffered HF), kullanıldı. Polisilisyum ve silisyumun köprü yapıların kurutulması sırasında, yüzey gerginliğine karşı, kritik Nokta Kurutma – CPD (Critical Point Dryer) – cihazı kullanılmıştır.

Bu cihazda çalışma şartları, CO2'nın özelliklerine bağlı olarak yapıldı. Karbondioksitin kritik noktasını elde etmek için, 31.1 ˚C sıcaklık ve 1072 Psi basınç gerekmektedir. Cihaz ile yapılan bu proses adımında köprü yapıların yüzeye yapışması engellenmiştir.

Tasarlanan her bir tip mikrosistem Sonlu Elemanlar Metodu ile COMSOL ve COVENTORWARE yazılımları kullanılarak simulasyonları yapılmıştır. Simulasyonda her yapının doğal birinci frekansı, maksimum akıma dayanıklılığı, kalite faktörü, ve deplasmanı incelenmiştir.

Birinci doğal frekansın simulyasonlarında, mikrosistemler dört farklı yönden incelendi. İlk olarak sabit genişlikde ve aynı koşullarda sadece çubukların uzunluğunu farklı alarak analiz yapılmıştır, örnek bulgu olarak 3 µm genişlik çubuklar için, 10 µm uzunluğa sahip çubuğun frekansı 12,6 MHz, 20 µm uzunluğa sahip çubuğun frekansı 3,14 MHz, 30 µm uzunluğa sahip çubuğun frekansı 1,39 MHz, 50 µm uzunluğa sahip çubuğun frekansı 0,49 MHz, 100 µm uzunluğa sahip çubuğun frekansı ise 0,12 MHz'dır.

İkinci adımda, aynı sabit koşullarda, sadece çubukların genişliğinin birinci doğal frekansa etkisi incelendi ve bunun doğal ferakanslarda etkisinin olmadığı belirlendi. Uzunluğu 30µm ve aşındırma deliklerin boyutları sırasıyla çubuğun uzunluk ve genişlik yönünde 2,062 µm × 2 µm olan bir çubuk için 3 farklı 5, 30, ve 50 µm genişlik için yapılan analizlerde birinci doğal frekansın 1,36 MHz olduğu tespit edilmiştir.

Üçüncü durumda, sabit boyutlarda aşındırma deliklerinin boyutlarını, çubuğun uzunluk ve genişlik yönünde değiştirerek birinci rezonans frekansa etkisi incelenmiştir. 100 µm uzunluk × 50 µm genişlik çubukların, aşındırma deliklerinin yanlarını genişlik yönünde sabit tutarak ve uzunluk yönünde artırarak yapılan analizde birinci rezonans frekansın artığı görülmüştür. Örnek olarak; 2,018 µm × 10,625 µm, 3,972 µm × 10,625 µm, ve 10,813 µm × 10,625 µm aşındırma delikleri için, birinci rezonans frekansları sırasıyla $8,22 \times 10^4$ Hz, $9,21 \times 10^4$ Hz, ve $1,32 \times 10^5$ Hz'dir. Aynı şekilde, aşındırma deliklerinin boyutları diğer yönde değiştirilerek analiz yapılmıştır. 50 µm uzunluk × 100 µm genişlikteki çubuklar için bu defa aşındırma deliklerin yanlarını uzunluk yönünde sabit tutmakla ve genişlik yönünde artırmakla, 2,062 µm × 2,018 µm, 2,062 µm × 3,972 µm, 2,062 µm × 10,813 µm, ve 2,062 µm × 31,334 µm delikler için sırasıyla birinci rezonans frekansın 1,38 MHz, 1,25 MHz, 0,915 MHz, ve 0,515 MHz değiştiği tespit edilmiştir.

Analizin dördüncü adımında, profilometre ile hesaplanmış gerilme değerini hesaba katarak birinci rezonans frekansın üzerindeki değişim çalışıldı. Bu durumda, SOI pulunun gerilme stresi pozitif olduğu için, çubukların birinci rezonans frekanslarının tamamı yüksek frekanslara kaydığı görüldü. Mesela, 12,6 MHz, 3,1 MHz, 1,4 MHz, 0,49 MHz, ve 0,12 MHz frekansları, sırasıyla 16,2 MHz, 5,9 MHz, 3,7 MHz, 2,1 MHz, ve 1,05 MHz frekanslara yükselmiştir.

Mikro çubukların kalite faktörü, birinci rezonansı frekansı açısından incelenmiştir. Analizler, 1 atmosfer ve 1,4 militorr değerinde vakum altında olmak üzere gerçekleştirildi. Simülasyon değerlerinden elde gelen bulgular gösterdiği gibi, mikro köprülerin vakum şartları içinde çalıştığı ispatlanmıştır. Örnek olarak, sabit 3 μm genişlik, ve 10, 20, 30, 50, ve 100 μm uzunluğunda çubuklarının kalite faktörleri oda basıncında sırasıyla 37, 9, 6, 14, ve 5'dir. Aynı yapıların kalite faktörlerinin değerleri 1,4 militorr basıncında sırasıyla $1,44 \times 10^4$, $1,12 \times 10^5$, $6,54 \times 10^4$, $3,07 \times 10^4$, ve $2,37 \times 10^4$ elde edilmiştir.

Mikro yapıların akıma karşı dayanıklıkları da araştırılmıştır. Çubukların nominal kalınlıkları 140 nm olduğu için, her mikrosistem için azami akım miktarını aşması sonucu ortaya çıkan gerilmeler veya ergime sıcaklığına yaklaşma sistemin geometrik yapısını değiştirmektedir. Silisyumun azami mukavemeti 300 MPa civarında ve özelliklerine göre ergime sıcaklığı 1690˚C'dır. Bu nedenle, çalışmamızda akım arttıkça ulaşılan ilk değer uygulanan akımın en üst değer olarak belirlenmesine sebep olmaktadır. Simülasyon sonuçlarında göründüğü mukavemet değeri belirleyici faktör olarak belirlenmiştir. Bu durumda, kırılma mukavemeti değerine karşılık gelen akım maksimum değer olarak belirlenmiştir. Farklı geometrilerde bu maksimum akım değeri üzerinde analizler yapılarak, sistemin davranışı belirlenmiştir. Aynı genişdeki çubukların 10, 20, 30, 50, ve 100 μm çubuk uzunluğuna karşı 12,2, 6,8, 4,6, 2,8, ve 1,4 mA olarak tespit edilmiştir.

Benzer şekilde, 30 μm uzunluğundaki numunelerde, genişlikler 5, 30, 50, ve 100 μm değiştirildiği zaman maksimum akım, sırasıyla 4,7, 6,5, 27, ve 53 mA olmaktadır. Göründüğü gibi, ne kadar çubuğun genişliği artırılırsa, o kadar büyük akımlara karşı dayanaklıdır. Aşındırma deliklerin etkisi birinci rezonans frekans çalışmasında yaptığımız gibi araştırdığımızda, 100 μm uzunluk × 100 μm genişliğe sahip numünede, çubuğun uzunluk yönünde aşındırma deliklerin yanlarını arttırmakla maksimum akımın arttığı belirlenmiştir. Aksi durumda, aşındırma deliklerinin yanlarını çubuğun genişlik yönünde artırarak yapılan analizde, maksimum akım miktarının azaldığı ortaya çıkmaktadır.

Analiz kısmında son olarak, mikrosistemlerin deplasmanları iki statik ve dinamik kuvvet durumlarına karşın incelenmiştir. Uzun çubukların esnek yapısı dolayısı ile yüksek bir deplasmana sahip olduğu görülmüştür. Dinamik veya statik kuvvete karşı deplasmanlar, çubuğun ağırlığına bağlıdırlar. Hafif çubuklar daha fazla deplasman yapmaya müsaitlerdir.

Son olarak simulasyon değerlerinin hepsi, deneysel sonuçlar ile birlikte karşılaştırıldı. Deneysel çalışmaları Polytec 500 – doppler fenomenler ve müdahale dalgalarıyla ölçen – cihazı ile yapıldı. Genelde, ölçüm ile simülasyon sonuçlarının birbirine yakın olduğu gözlenmekle beraber bazı parametrelerin modellenmesinde detay çalışma yapılması gerekmektedir. Birinci rezonans frekans parametresinin ölçümleri ile simülasyon analizi sonucunda belirlenen değerler birbirine yakın çıktığı görülmüştür. Bunun yanında deplasmanlar ve kalite faktöründeki ölçüm değerleri ile analiz değerleri arasında ölçüm sırasındaki gürültü, bazı sönümleme değerlerinin teorik olarak eklenmemiş olması ve/veya üretim ile ilgili olarak geometrik farklılıklar (homojen olmayan oksit aşındırılması) gibi etkenler dolayısı ile farklılık göstermiştir. Örnek olarak, 100 μm uzunluk × 30 μm genişlikteki mikrosistemde simule ve deneysel veriler açısından birinci rezonans frekansın değeri 8×10^5 Hz civarındadır, ama 0,15 nN için, deplasman değeri simülasyon açısında 0,2 μm olması gerekirken, karakterizasyon sonucu 2,3 nm'dir.

Bu tezde, her yapının birinci rezonans frekansları, maksimum akıma karşı dayanaklılığı, kalite faktörünün gerilim ile bağıntısı, ve özellikle mikrosistemin karakteristik parametrelerin çubuklar üzerinde olan deliklerin boyutları, çubuğun uzunluk yönünün ya da genişliğinin değiştirilmesi ile incelenmiştir. Deneysel ölçümler analiz sonuçları ile karşılaştırmalı biçimde değerlendirilmiştir. Bunun yanında, kapsamlı bir literatür çalışması yapılmıştır ve gelecekte yapılan bu tarz sensorların nasıl bir özelliğe sahip olmaları gerektiğini belirleyebiliriz.

1. INTRODUCTION

At recent decades, MEMS devices have evolved several branches of science and industry, pressure sensors, magnetometers, switches (2, 10). MEMS devices are also being discovered as a very useful tool in the bio-medical field (5, 17).

Magnetometers are sensors that are used in various environments and products of Industries especially, by Micro Electro Mechanical Systems (MEMS) technology modeled numerous sketches, which are packed into small dimensions, as well as integrates the mechanical and electronic components on a single chip. Therefore, this technology allows to be embedded in portable devices such as cell phone and digital watches. These sensors offer a variety of contactless sensing for measuring magnetic fields have the unique ability to reveal realities that cannot be perceived by the human senses.

For using these sensors, it is important to fabricate resonators with very high mechanical quality factors (Q), where this parameter is proportional to the ratio of the stored energy to the total dissipated energy per cycle of vibration. A low value of quality factor implies greater dissipation of energy and results in reduced sensitivity and increased power consumption. For improvement of quality factor the reasons, which interfere with that, should be verified. Into next section by defining of these energies dissipation mechanisms such as: anchor losses, air- damping, thermoelastic damping, etc. will be feasible to calculate it.

A challenge of the magnetic field sensors is the suppression of any background noise. Due to geological effects on Earth's magnetic field, the performance limit of the future magnetic field sensors will be the variations. In addition, adequate Magnetic sensor is the sensors that have these features: simple basic physics, higher quality factor and dynamic range, smaller size, low power consumption, output response offset and the temperature dependence.

In this thesis, resonant magnetic field sensors based on MEMS technology by exploiting Lorentz force, has been proposed, fabricated and characterized. During in this thesis precisely 438 sensors at different widths, lengths and etching holes that are affected on Quality factor and Natural frequency were investigated theoretically, simulated by Coventorware & Comsol, and experimented in the Microwave Laboratory of the University of Louvain La Neuve.

At the state of the art section, several Materials and designs types that have been utilized will be exhibited and each sensor trait will be discussed. Our design is simplest one, clamped-clamped beam, which is placed in a150 mT static magnetic field (B-ND magnets) where is applied AC voltage between two contacts and the beam's displacement that has been occurred by Lorentz force is measured in ambient air and different vacuum condition at around Natural frequency by using Laser Doppler velocimetry (Polytec MSA-500).

2. THE STATE OF THE ART

This section discusses recent progress in the most frequently used magnetic-field MEMS, which are perfectly compatible with microelectronic technologies, because of the silicon base technology and their different criteria such as sensitivity and resolution – in the last section a glossary defined all technical parts – will present.

This Thesis focused on the design of MEMS based magnetometer after defining of several recent articles and then from comparing several materials properties which is commonly used in these sensors.

2.1. Magnetic Sensors And Different Applications

From the invention of some conventional magnetometers like compass since 600 years ago until now, through the times always was in the improvement. Nowadays by MEMS technology, various magnetic field sensors are used in multiple areas.

For application of the magnetic sensors, two categories can be distinguished(16): Direct, what are those that only get information about the magnetic field whether strength or direction and Indirect sensors where is used as an intermediary carrier to measure quantity like tandem transducers.

For direct sensors, we can mention:

- Magnetic levitation control
- Attitude control of satellites
- Magnetometry: control of a magnetic apparatus such as classical and superconducting electromagnets; Instrumentation for particle accelerators as well as determination of the full magnetic field vector, its direction, and its gradient by detecting two or all three vector components,
- etc.

At tandem transducers, there may be several stages of transductions. Each conversion has some errors and each step may be amplified instinctively. Therefore, the selectivity and sensitivity of each step of transducer is very influential to approach precise and realistic output. Commonly the last step of transduction is transduced into electrical signal with maximum sensitivity, which is presented in this section.

Some common application is used daily from theses sensors are:

- Automotive anti-skid breaking system (ABS)
- Traffic detection when a ferromagnetic body is passing
- Position detection,
- etc.

2.1.1. Fluxgate magnetometer

Based on Faraday's Law, the fluxgate magnetometer uses magnetic induction through a variation of fluxgate intercepted by a bobbin produces electromotive force in it.

$$\varepsilon = -\frac{d\phi}{dt} \quad (2.1)$$

The Fluxgate consists of two coils wound around a ferromagnetic core with high permeability. The coils surrounding the ferromagnetic core have two different duties: one of them is intended for excitation and other one for measuring of electric current, which has been produced by prior coil. Initially, the excitation leads to saturation of the ferromagnetic material. The changing magnetic field id measured by the induced voltage across the measuring coil. Then, a new excitation is applied to magnetize the core in the opposite direction.

When a filed is present in the axis of the ferromagnetic bar, is oriented in the direction of the core field, saturation of core pressed faster and if it is opposite direction will be slower. From the phase shift between the signal measured at terminals of the measuring coil and the excitation signal magnetic field strength can be deduced.

Petridis (20) proposed a hybrid between the fluxgate magnetometer and the Hall effect magnetometer. The magnetic core is brought to circular saturation magnetization in a rotating way. This is induced by an excitation field, produced by four rotating planar coils. A Hall sensor, which is close to nucleus, sense flux density changes by the variation of the field and act as a measuring coil. The phase shift and the amplitude of the signal are calculated by the value and orientation of the field components and the vertical component is measured from the voltage offset of the Hall device.

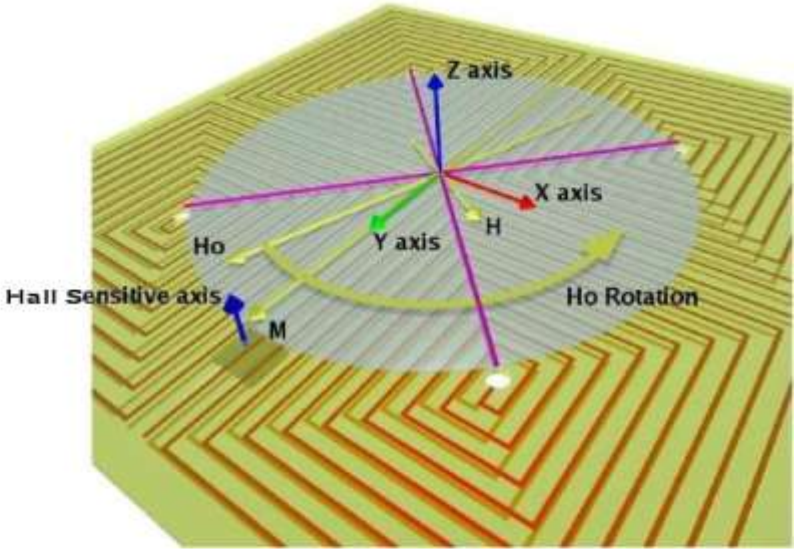

Figure 2. 1 Combination of Fluxgate and Hall Effect [6].

Into ferromagnetic elements, the magnetization effects on group of the material not individual atoms. Therefore magnetization or demagnetization field bring about changing of orientation of these groups, whilst this reorientation occurs by sudden jumps. In this state, the data become incomplete because the core saturation does not happen as well as a progressive variation reduces this effect and noise associated with it.

A variant of the fluxgate closed magnetic path, is presented by Won-Youl Choi (32). This design has a linear response over the range of ± 0.1mT. The advantages of the closed course ferromagnetic core are lower leakage magnetic flux core, easier saturation achievement, low excitation voltage required and higher sensitivity. However, in the case of a closed path, the direction of the field is less well-defined than in the case of a single bar.

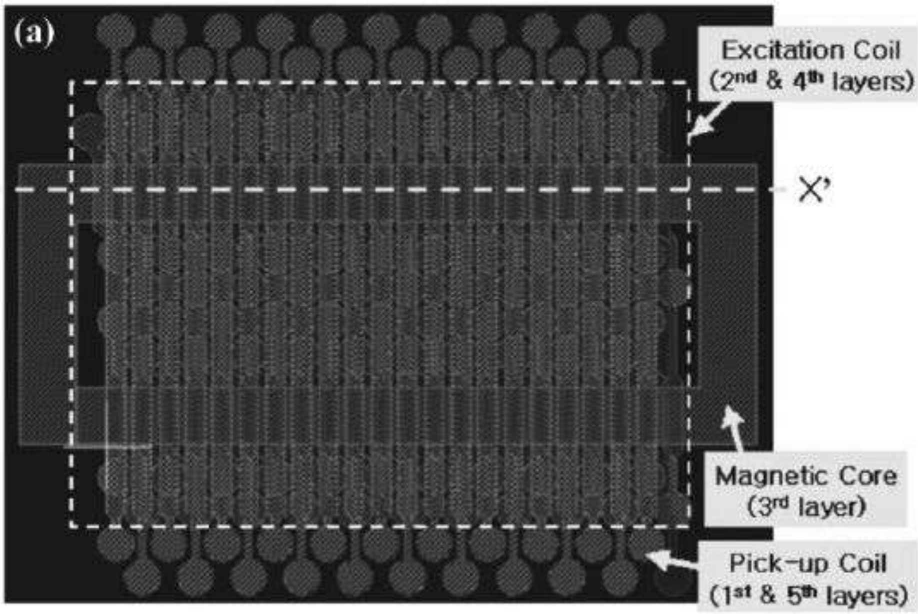

Figure 2. 2 Fluxgate ferromagnetic with closed path core [7].

One of the disadvantages of this case is miniaturization, because reduction of the size of the fluxgate magnetometer is most often at the expense of sensitivity of the sensor. For instance, in a miniature fluxgate, coils can have only a limited number of turns.

The fluxgate magnetometers have a resolution of about 0.1nT and are able to measure continuous variables or low frequency of magnetic field, at proximity of mT intensity.

Table 2. 1: Fluxgate Magnetometer

References	Sensitivity	Report
Petridis	$S_A^{(V)} = 2683V.T^{-1}$	$N_{ribbon,core} = 600nT^{-1}.Hz^{-1/2}$
Won-Youl Choi	$S_A^{(V)} = 780V.T^{-1}$	SNR = 10000

2.1.2. Superconducting quantum interference device (SQUID)

A superconducting quantum interference device (SQUID) is a mechanism used to measure extremely weak signals, such as subtle changes in the human body's electromagnetic energy field. Using a device called a "Josephson junction" in honor of its inventor; a SQUID can detect a change of energy as much as 100 billion times weaker than the electromagnetic energy that moves a compass needle. A Josephson junction is made up of two superconductors, separated by an insulating layer so thin that electrons can pass through. A SQUID consists of tiny loops of superconductors employing Josephson junctions to achieve superposition: each electron moves simultaneously in both directions. Because the current is moving in two opposite directions, the electrons have the ability to perform as qubits (that theoretically could be used to enable quantum computing). Note the SQUID Magnetometers type do not measure the absolute value of the magnetic field, but only field variations.

SQUIDs have been used for a variety of testing purposes that demand extreme sensitivity, including engineering, medical, and geological equipment. Because they measure changes in a magnetic field with such sensitivity, they do not have to encounter a system that they are testing.

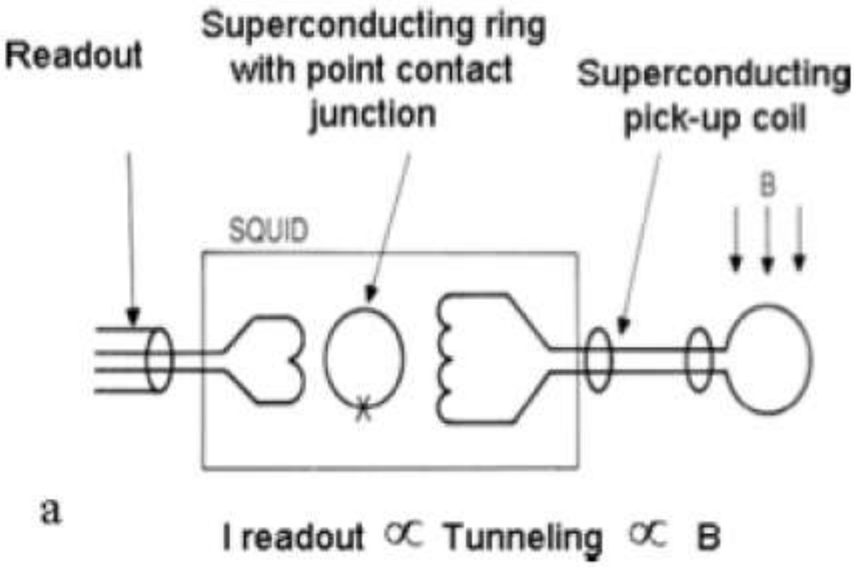

Figure 2. 3 Schematic of SQUID**(16)**.

SQUIDs are usually made of either a lead alloy (with 10% gold or indium) and/or niobium, often consisting of the tunnel barrier sandwiched between a base electrode of niobium and the top electrode of lead alloy. A radio frequency (RF) SQUID is made up of one Josephson junction, which is mounted on a superconducting ring. An oscillating current is applied to an external circuit, whose voltage changes as an effect of the interaction between it and the ring. The magnetic flux is then measured. A direct current (DC) SQUID, which is much more sensitive, consists of two Josephson junctions employed in parallel so that electrons tunnelling through the junctions demonstrate quantum interference, dependent upon the strength of the magnetic field within a loop. DC SQUIDs demonstrate resistance in response to even tiny variations in a magnetic field, which is the capacity that enables detection of such minute changes.

2.1.3. Hall effect sensors

Nowadays, the Hall Effect is widely used, it is based on the potential differences at the edge of a conductor when is set in magnetic field. This tension is appeared as a V_{Hall} (Hall Voltage) transversely to the direction of the current by the free electrons moving in the conductor at the speed of the $\vec{v}$, subjected to the Lorentz Force:

$$\vec{F}_L = q\vec{v} \times \vec{B} \quad (2.\ 2)$$

Depending on the orientation of this force, the changes are concentrated on one side of the driver. The exerting F in opposite direction for equilibrium generates Hall voltage. By the Coulomb force:

$$\vec{F} = q\vec{E}_{Hall} = -q\vec{v} \times \vec{B} \quad (2.\ 3)$$

Where E_{Hall} is the electric field resulting from the potential difference V_{Hall}.

For an identical current, the Hall Effect is more pronounced in semiconductors. Because in metal only one type of carrier “electron” is under effect but in semiconductor it is completely more complex where the carriers are generally both electrons and holes , which may be present in different concentrations and have different motilities.

These sensors consume 150 mW, and variable fields can be measured over a wide frequency up to 1MHz. Their magnetic field range, as was mentioned before, depend on the semiconductor used in the case of silicon and is between 1 – 100mT.

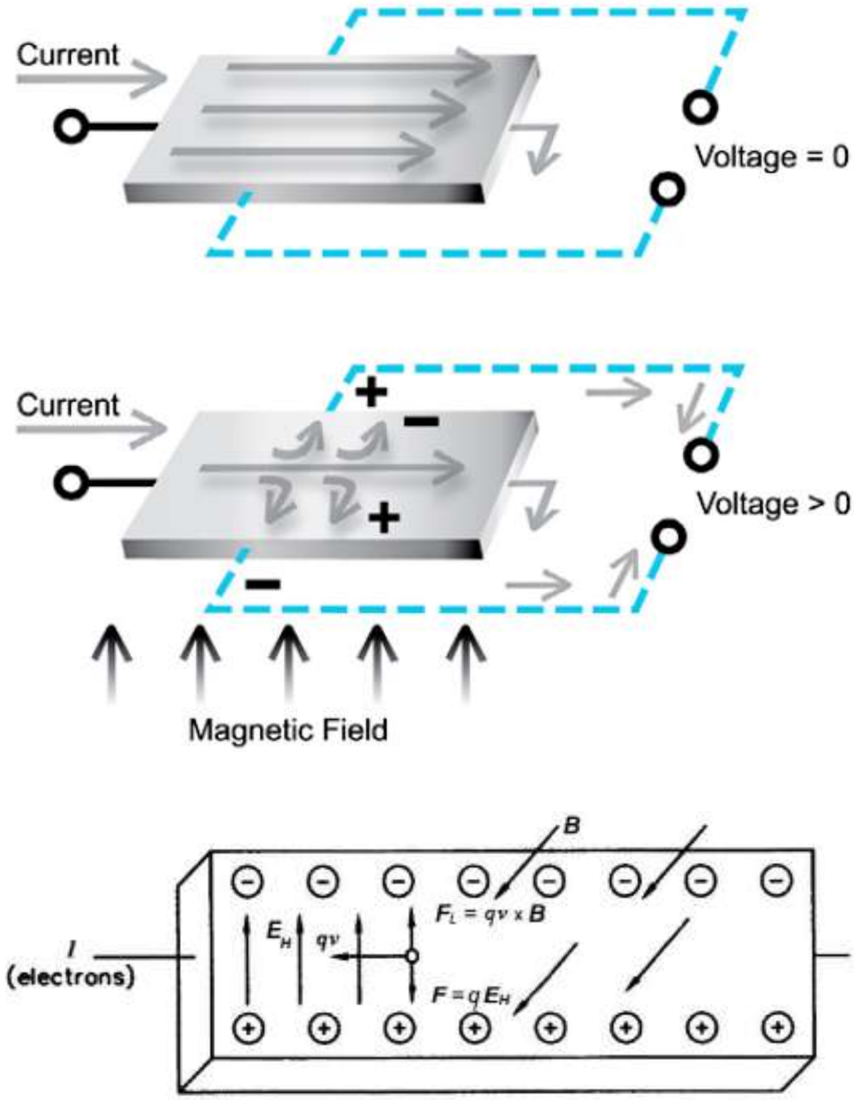

Figure 2. 4 Principle of Hall Effect**(16)**.

The wide use of this type of sensors is due to ease of production and encompassing of Hall device and interface electronics. By an integrated magnetic concentrator and new circuit architecture for the signal processing at Randjelovic (22) proposed microsystem, it is able to measure a weak filed around 6 mT with the resolution better than 0.1mT.

Noykov (18) proposed a configuration of 32 hall sensors arranged in a circle, used as a compass. This sensor measured the magnetic field orientation with a resolution of 0.5˚. This design consists of multiplexers to query each sensor individually, so for the measuring it need time into account of complete a full measurement of all sensors.

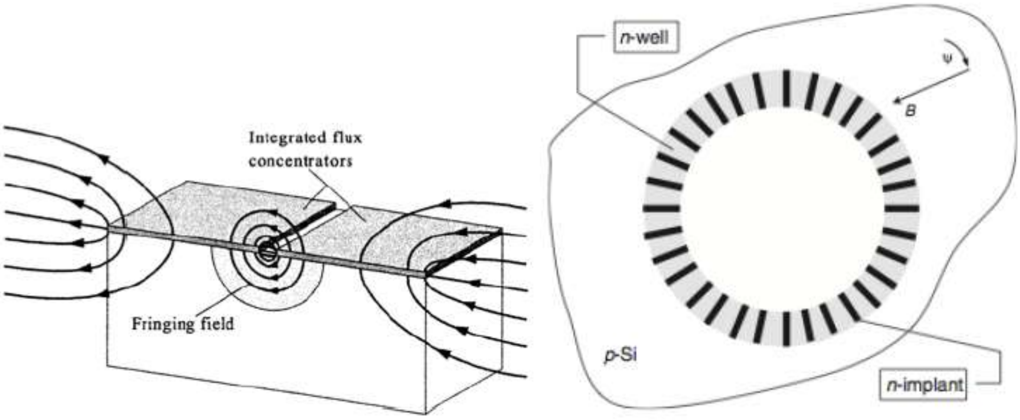

Figure 2. 5 Hall Sensor with high sensitivity by Randjelovic [8] *(Left)*, Circular configuration of magnetometers Hall-Effect [9] *(Right)*.

In the previous model, which has been proposed by Petridis where combining fluxgate magnetometer and Hall, described on fluxgate sensors, we note the sensitivity of the module Hall: $S_A^{(V)} = 25V.T^{-1}$

Table 2. 2: Hall Effect Magnetometer

Reference	Sensitivity
Randjelovic	$S_A^{(V)} = 420V.T^{-1}$
Noykov	$S_{AI}^{(V)} = 51\mu V \mu(A.T)^{-1}$ with

2.1.4. Anisotropic magnetoresistance (AMR) magnetometers

AMR is a phenomenon observed in thin films of certain materials, such as Alloys of Iron and Nickel. Their electrical resistance is not isotropic and has maximum value when the direction of the current is parallel to the external magnetic field.

$$\Delta R \alpha \cos^2(\phi_{mag} - \phi_{current}) \quad (2.\ 4)$$

Where $\phi_{mag} - \phi_{current}$ is the angle formed between the direction of the magnetic field and the electrical current direction.

The scope of this class of sensors can range from 5mT to one micro T, and dynamic range can be reached until 1 GHz. In the case of assemblies including a buckle against reaction, the resolution of 10nT is reported. The other advantages of these materials are smaller, higher spatial resolution and consume very little energy, less than 0.5 mW.

2.1.5. Giant magnetoresistance (GMR) magnetometers and spin-dependent tunneling (TMR) magnetometers

Theses magnetometers are made of several layers of magnetic materials, separated either by a thin layer of non-magnetic conductor (GMR) or insulating layer (TMR or SDT). The variation of electrical resistance of layers, depending on external magnetic field is the reason that they were named Giant Magnetoresistance.

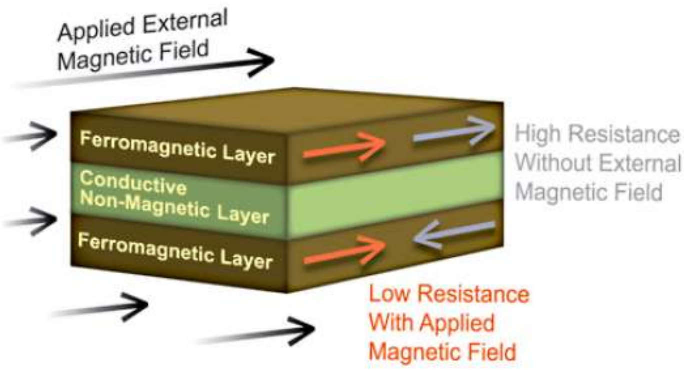

Figure 2. 6 Structure of GMR.

If the external magnetization oriented in the same direction of the layer's magnetization, the electrical resistance of previously mentioned layer would be low and if in the opposite direction will be high. These sensors are very sensitive to temperature variations, so they are mounted in a Wheatstone bridge to compensate temperature variants. They operate over a wide range of 10nT (1Hz) up to 0.1T.

GMR and SDT Sensors suffer from high noise, but their main advantage is small size (a few nanometers) which offers high resolution. Because of that, they replaced AMR sensors which were used in hard disk driver where have a size of a few millimeters.

2.2. MEMS Magnetometer

MEMS based Magnetometers can be distinguished on their transduction principle to two clusters, the majority of them use Lorentz force principle actuation, and rests of them are usually based on permanent magnets or ferromagnetic elements.

For the measuring of the amount of the magnetic field at the sensors are based on Lorentz force principle we need to extract this value by methods that are categorized three main fundamental way: Optical measurement, Piezoresistive and Capacitive.

Lorentz force and most of the magnetometers have infinite number of resonance frequencies, which can vibrate at these frequencies that is named vibration mode, too. Generally, first mode or frequency is the most used, because a sensor based on this mode has a larger output signal (amplitude vibration) that increases its sensitivity.

Usually to achieving this phenomena resonant magnetic field sensor is excited by source i.e. AC voltage at frequency equal to its first natural mechanical resonant frequency of beam, where maximum deflection happen. Hereby by three method of measuring, that is mentioned previously, we will able to attain external amount of magnetic field.

2.2.1. Sensor based on Lorentz force – piezoresistive sensing

The Piezoresistive detection is based on materials that their resistances vary subjected to a stress-induced acceleration, which is actuated by Lorentz force. Wheatstone bridge with two active Piezoresistive on vibrated region and two passive Piezoresistive on substrate usually carries out this detection. Figure 2.7 clearly indicate the subject.

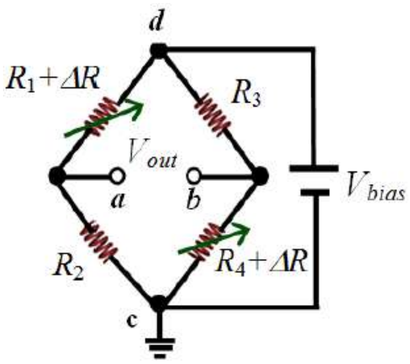

Figure 2. 7 Wheatstone bridge.

The resistances number 1 and 4 is active piezoresistive that their resistance variation is changed by:

$$\Delta R = G\varepsilon_x R \quad (2.\ 5)$$

Where G is the Gauge factor and ε_x is longitudinal strain.

The change in the resistance of the active piezoresistive lead to produces an output voltage (V_{out}) that is determined by:

$$V_{out} = \frac{\Delta R}{2R + \Delta R} V_{bias} \quad (2.\ 6)$$

Where V_{bias} is the bias voltage of the Wheatstone bridge.

The sensor Sensitivity (S) is acquire from the ratio of the output voltage to the external magnetic field (ΔB_x).

$$S = \frac{\Delta V_{out}}{\Delta B_x} \quad (2.\ 7)$$

The Beroulle (3) sensor has been based on a resonant frequency in the form of U attached to substrate. When the current is crossed from the beam subjected to a magnetic field (perpendicular to the plane of the beam), Lorentz force excited the beam and deflected it. Especially when current frequency oscillates at beam' natural frequency brings maximum deflection about. This deflection is sensed by piezoresistive, which has been mounted on the end of the two U shape terminals.

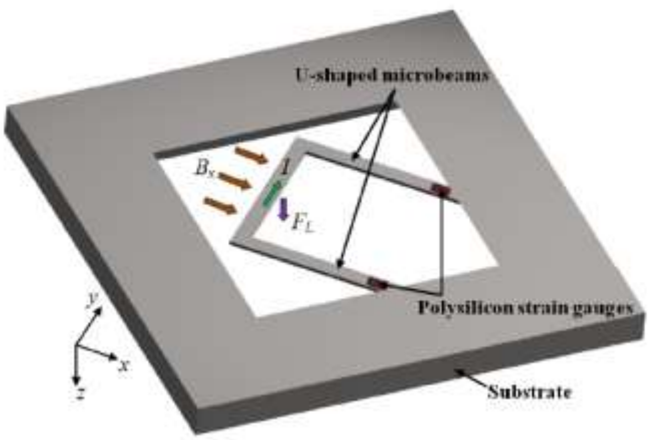

Figure 2. 8: Schematic of the operation principle of the Beroulle's resonant magnetic field sensor**(3)**.

In 2009, Herrera-May (9) proposed a system tray, with a high quality factor where current is passing throw from four bending microbeams and subject to the external magnetic field (B_x), Lorentz force originated which cause a seesaw motion on the microplate. Then these motions and bending of microbeams strain the two active piezoresistives, and by another two passive piezoresistive which have been mounted on substrate, cause output voltage in Wheatstone bridge circuit by changing resistances of active piezoresistives. Finally, the magnetic field magnitudes are detected by the electrical signal output of the Wheatstone bridge.

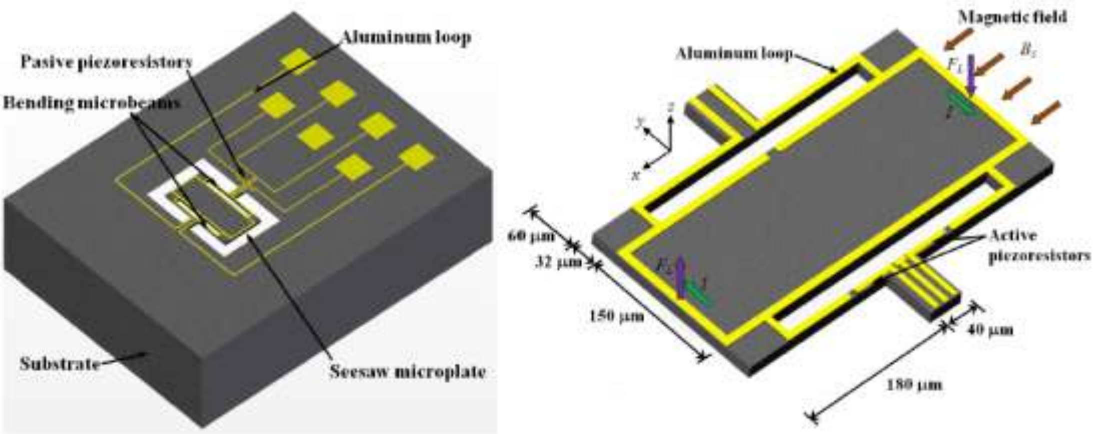

(a) (b)

Figure 2. 9: Schematic of the (a) structural configuration and (b) operation principle of the Herrera-May's resonant magnetic field sensor**(9)**.

The following year, Herrera-May suggested a similar concept with perforated surface for reducing air resistance (27). Because in this shape, air damping that is dominant factor for quality factor in ambient atmosphere, reduce energy losses significantly.

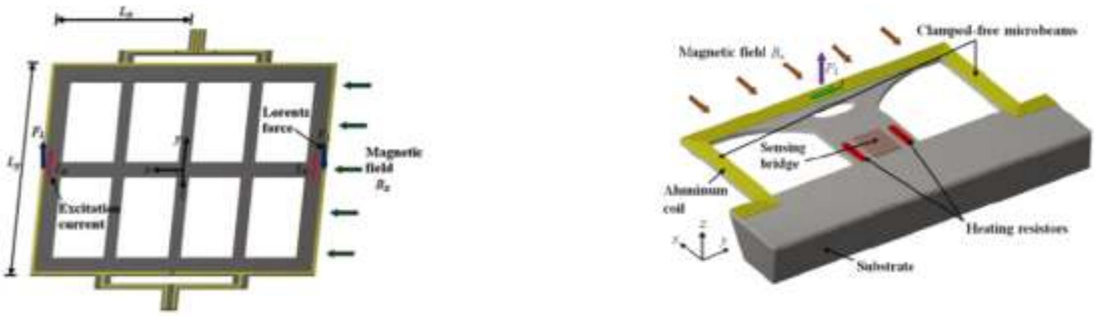

Figure 2.10: Schematic of the operation principle of the Herrera-May *(left)* and Sunier's *(right)* resonant magnetic field sensor**(27)**.

The last sensor is presented by Sunier (26), is a microbeams vibrate steadily at their resonant frequency due to the thermal actuation of two heating resistors. In this device, the Lorentz force constrains the tip of the microbeam and change their equivalent spring like additional spring force (F_L). This variation, which has been caused by Lorentz force principle lead to the variation of the resonant frequency, (Δf_{res}) is indicated by:

$$\Delta f_{res} = \frac{1}{2\pi}\left(\frac{k - F_L / x}{m}\right)^{\frac{1}{2}} \quad (2.\ 8)$$

Where k is spring constant, m is effective microbeam mass and x is the resonator position (deflection).

In conclusion, the resonant sensors with piezoresistive sensing require simple readout circuits (Wheatstone bridge), high sensitivity and low manufacture-cost. Although, they need a careful packaging, trimming, and compensation circuits for reducing the effect of the thermal fluctuations on their performance. The summary performance of mentioned sensors is available at table 2.3

Table 2. 3: MEMS Magnetometer with Piezoresistive Detection

Reference	Sensitivity	Resolution	Quality Factor
		Resonant Freq.	Consumption
Beroulle (3)	$S_A^{(V)} = 530mV.T^{-1}$	$B_{\min} = 10\mu T$	$Q = 59 @ p_{atm}$
		$f_o = 8.97kHz$	
Herrera-May (9)	$S_A^{(V)} = 0.403\mu V.\mu T^{-1}$	$B_{\min} = 143nT$	$Q = 842 @ p_{atm}$
		$f_o = 136.52kHz$	$P < 10mW$
Herrera-May (27)	$S_A^{(V)} = 1.2V.T^{-1}$	$B_{\min} = 80nT$	$Q = 93 @ p_{atm}$
		$f_o = 13.87kHz$	$P = 2.05mW$
Sunier (26)	$S_A^{(V)} = 60kHz.T^{-1}$	$B_{\min} = 1\mu T$	$Q = 600 @ p_{atm}$
		$f_o = 175kHz$	$P = 5mW$

2.2.2. Sensor based on Lorentz force – optical sensing

Optical sensing is usually based on laser interferometry, which principally detects it by Doppler Effect. Laser is illuminated to the part of the resonant system that will be deflected by Lorentz force principle subject to magnetic field and current flow. Then the reflected light beam is synchronously detected with a position sensitive detector. Consequently, by determining angle between the incident light and reflected beam from the surface of the resonator, magnitude of magnetic field is measured.

The resonant magnetic field sensors with optical readout system have immunity to Electromagnetic Interference as well as a reduction in their electronic circuitry and weight. Although the sensitivity of this measurement method undeniable, but the optical sensing presents some problems due to the intrinsic losses of the structural imperfections of the sensors and can require complex fabrication processes.

There are several examples of Xylophone Bar Magnetometer (XBM) which has been developed by Zanetti (33) and Wickenden (31), which their movement is detected by Laser as it is exhibited at Figure 2.11. The deflection of the XBM, which is induced by the Lorentz force, is estimated by pointing a Laser beam on the structure, partially coated with a reflective layer and reflecting beam, which is sensed by photosensitive sensor signal at detector. Essentially this measurement is yield from phase shift, which happen between output and input signal of Laser beam.

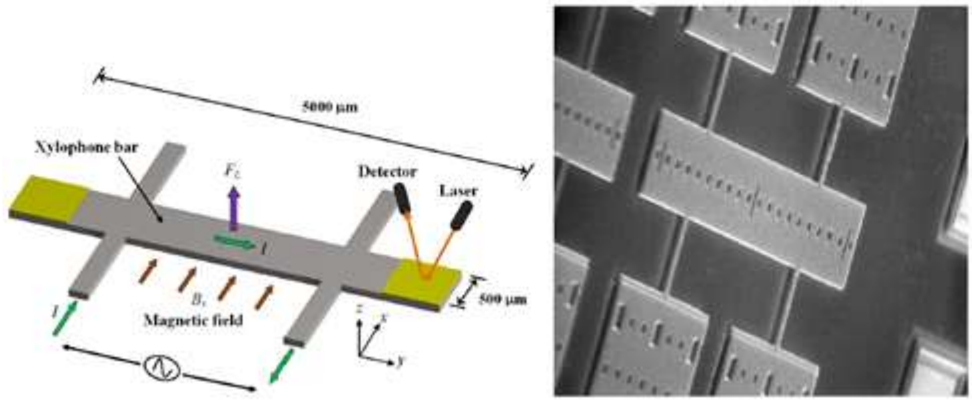

Figure 2.11: Concept of XBM Detection by Optical Sensing**(33)** (*left*), SEM Image of polysilicon XBM by Wickenden**(31)** (*right*).

There are other structures or systems, which are proposed, by Keplinger (15) and Herrera-May (8) that Figure 2.12 demonstrates it. Table2.4 demonstrates some results.

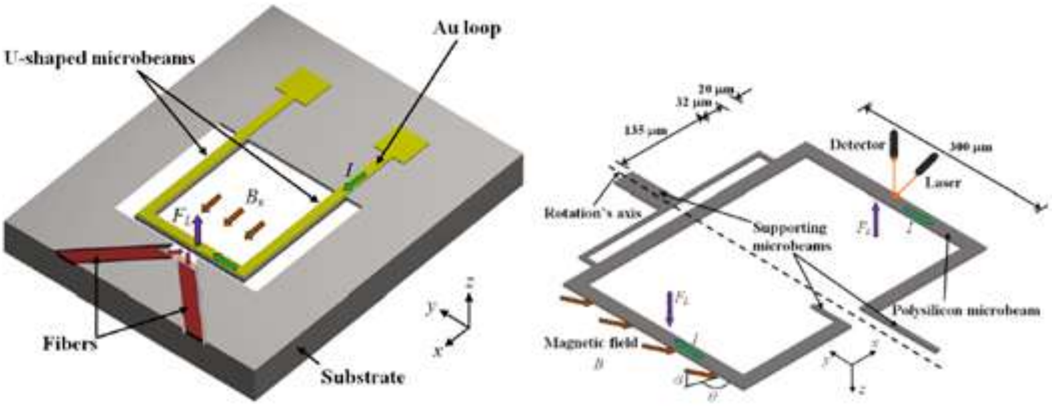

Figure 2.12: Schematic of operation principle of Keplinger(15) (*left*), and Herrera-May(8) (*right*) resonant magnetic field sensor.

Table 2. 4: MEMS Magnetometer with Optical detection

Reference	Sensitivity	Resolution	Quality Factor
		Resonant Freq.	Consumption
Zanetti (33)		$B_{\min} = 1nT$	$Q = 7000 @ p_{atm}$
			$P = 10mW$
Wickenden (31)		$B_{\min} < 1\mu T$	$Q = 700 @ 4.7 p_a$
		$f_o = 78.15kHz$	
Keplinger (15)		$B_{\min} = 10mT$	
		$f_o = 5kHz$	$P = 2.05mW$
Herrera-May (8)	$S_A^{(d)} = 530nm.T^{-1}$	$B_{\min} < 10mT$	$Q = 1.66 @ p_{atm}$
		$f_o = 19.4kHz$	$P = 1.2mW$

2.2.3. Sensor based on Lorentz force – capacitive sensing

The capacitive detection is based on the detection of small changes in capacitance between two plates due to the relative motion of the structure to each other. This method is used widely in application of accelerometers, as these sensors are inexpensive, have good performance in terms of noise and low power consumption (12).

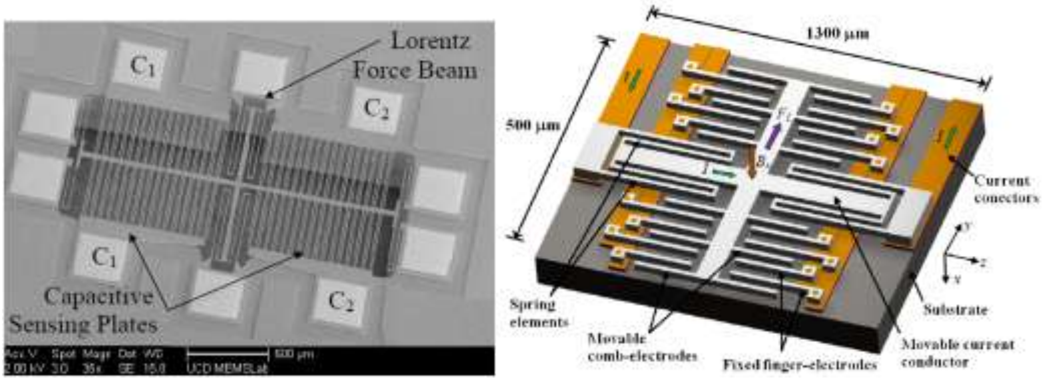

Figure 2.13: Schematic of SEM image of Thompson resonator**(28)** (*left*) and operation principle of Emmerich resonator**(6)** (*right*).

Thompson (28) and Emmerich (6) proposed prototype that are so similar to XBM as presented by Tucker (29). The main difference is, related to the geometry of the structures and their shapes. All capacitive fingers are arranged on a beam, perpendicular to the joining track and actuation path and by displacement of these fingers due to Lorentz force, bring about changing capacity at most, first mode frequency where we can able to achieve maximum displacement.

There is also a transposition of the balance, given by Kadar (13), wherein the electrodes are located on the surface of the balance and under a cover glass face to face them.

An another alternative structure is proposed by Ren (24) such that a low resistivity silicon structure is suspended by two torsional beam over the glass substrate and above the silicon a thin layer coil with thickness of 1 µm and width of 0.5 µm is deposited for excitation. This allows using same current for producing more torque and exploiting more displacement.

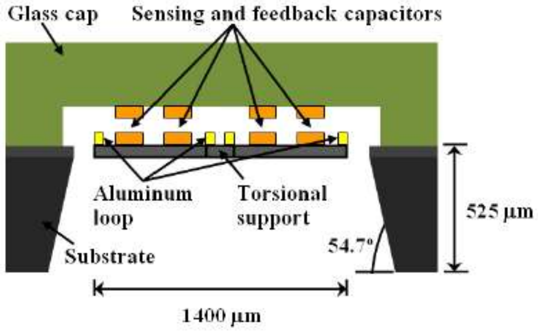

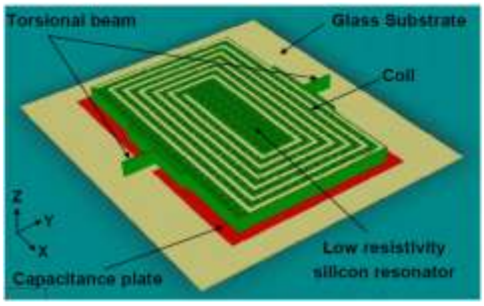

Figure 2.14: Schematic and features of sensors by Kadar**(13)** (*left*), and Ren**(24)** (*right*).

The last sensor is presented by Bahreyni (1), which is fabricated in a standard bulk micromachining without of any additional process. The operation principle of this sensor is based on shifting resonant frequency due to axial stress, which is constrained by crossbars and spring beams that have been connected to shuttle. During the sensor operation, the shuttle of the resonator is driven and kept under resonance by means of electrostatic actuation and sensing.

The amount of the shift in frequency is proportional to the current I_{XB}, Magnitude and direction of the existing magnetic field.

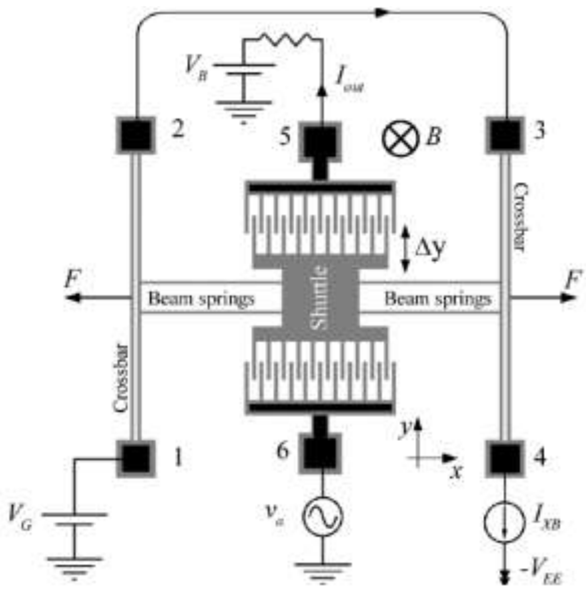

Figure 2.15: Schematic and operation principle of Bahreyni designed sensor**(1)**.

The resonant magnetic field sensors with capacitive sensing like other method suffering from such factors like parasitic capacitances in the connecting, which lead to measure signal complicatedly. For obtaining optimized output with high quality factor, its need complicated electronics and vacuum-package. Some of the parameters for each sensor that have been presented are available in table 2.5.

Table 2. 5: MEMS Magnetometer with Capacitive Detection

Reference	Sensitivity	Resolution / Resonant Freq.	Quality Factor / Consumption
Thompson (28)	$S_A^{(V)} = 31.4 mV_{rms}.T^{-1}$		$Q = 48.8 @ p_{atm}$
		$f_o = 8.46 kHz$	
Kadar (13)	$S_A^{(V)} = 500 \mu V.\mu T^{-1}$	$B_{\min} = 1nT @ vac.$	$Q = 700 @ 5 p_a$
		$f_o = 2.4 kHz$	$P \approx 1mW$
Tucker (29)		$B_{\min} = 1\mu T$	$Q = 1000 @ 5 p_{atm}$
		$f_o = 100 kHz$	$P = 7.5mW$
Bahreyni (1)	$S_A^{(d)} = 69.6 Hz.T^{-1}$	$B_{\min} = 217nT$	$Q = 15000 @ 2 p_a$
		$f_o = 27kHz$	$P = 2mW$
Emmerich (6)	$S_A^{(V)} = 820 \mu V.\mu T^{-1}$	$B_{\min} = 200nT$	$Q = 30 @ 101 p_a$
		$f_o = 1.3 kHz$	$P = 2mW$
Ren (24)	$S_A^{(V)} = 0.4V.\mu T^{-1}$	$B_{\min} = 30nT$	$Q = 2530 @ 10 p_a$
		$f_o = 27kHz$	$P = 2mW$

3. MAGNETOMETER CONCEPT

3.1. Operation Principle

As in previous section, we perceive that a resonant structure presents an amplified response to an excitation source of supply with frequency equal to the natural mechanical resonant frequencies of the structure. A structure commonly has infinite number of resonance frequencies but most efficient one is first resonance where 90% of vibration, happen in this mode. There are also other structures, which operate at second harmonic vibration (19).

Therefore, when a resonant structure operates at their modes (especially first mode) can achieve larger output signal, which is excited by electrostatic forces or Lorentz forces and higher sensitivity.

Previously, several structures such as Cantilever (clamped-free), torsional etc. have been investigated. Our design is clamped-clamped beam like figure 2.16. If an excitation current, (I) flows inside beam with L_y length in the direction of y with a frequency equal to the first beam-resonant frequency, while the magnetic field (B_x) is exposed to beam in direction of x, the Lorentz force (F_L) is generated in the z direction that lead to deflect beam and can be determined by:

$$F_L = IB_xL_y \quad (3.\ 1)$$

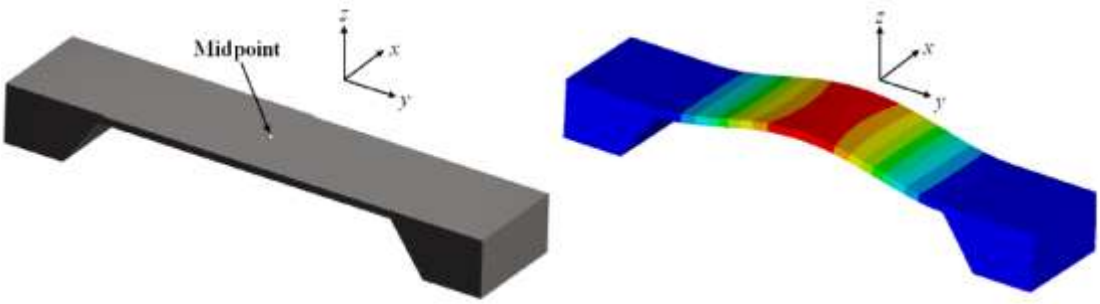

Figure 3. 1: Clamped-clamped beam.

The flexibility of Clamped-clamped beam in compare of other structures like cantilever is a little low. Hereby, the first frequency of beam happens at higher frequencies. Generally, the first resonance frequency concept by the Rayleigh method is introduced through the ratio of the maximum potential energy (U_{max}) to the maximum kinetic (T_{max}) energy of the structure (23). Then f_{res} is obtained by:

$$f_{res} = \frac{1}{2\pi}\left(\frac{U_{\max}}{T_{\max}}\right)^{\frac{1}{2}} \quad (3.\ 2)$$

With

$$U_{\max} = \int_L EI\left(\frac{\partial^2 z(y)}{\partial y^2}\right)^2 dy \quad (3.\ 3)$$

$$T_{\max} = \int_L \rho A(z(y))^2 dy \quad (3.\ 4)$$

Where L is the length of the resonant structure, E is the elasticity modulus, I is the cross-sectional moment of area, ρ is the density, A is the cross-sectional area, and z(y) is the function of the deflection of the resonant structure.

As it is seen from the formula, the first resonant frequency of a structure is directly proportional to its elasticity modulus and cross-sectional moment of area, and inversely proportional to its density and cross-sectional area.

In addition, residual stresses on the structure or built-in strain can affect its resonant frequency (11, 14). Therefor a variation in these parameters leads to changing in resonant frequency. Here another formula introduces first resonant frequency for clamped-clamped beam, which is more perceptible:

$$f_{res} = \frac{h}{2\pi L^2}\sqrt{\frac{42.7E}{\rho}\left(1+\frac{2}{7}\varepsilon\frac{L^2}{h^2}\right)} \quad (3.\ 5)$$

Where E and ρ are Young’s or elasticity modulus and density, h, L and ε are the thickness, the length and the built-in strain of the beam (11, 14).

3.2. Noise in Micromechanical Systems

Miniaturization of Mechanical sensors is not limited by non-ability to fabricate small structures. Mostly noise sets the limit for the smallest acceptable size. For instance, at resonant structure usually designers and researchers attempt to obtain higher resonance frequency or simply to lower the cost by incorporating more devices on a silicon wafer. In this section, we will discuss about noises that influence with frequency, which help us to understand noise limitation to design optimal sensor.

Noise:

Noise is random fluctuation of electrons, atoms, or molecules. For predicting of noise value, because of noise, it is not possible to measure it instantaneously. Hereby by knowledge of noise characterization, we can calculate it with probability distribution. For most physical noise sources, this probability follows the Gaussian distribution.

3.2.1. Noise qualification

"The rms-noise (Standard deviation value) characterizes the noise amplitude in time domain but gives no insight into what frequency the noise appears"(12).

The power spectral density $\overline{v}_n^{\,2}$ and spectral density $\overline{v}_n \equiv \sqrt{\overline{v}_n^{\,2}}$ show us how much noise per unit bandwidth, on average, there is on certain frequencies. Knowing the noise frequency spectrum allows calculating the effect of system bandwidth on total noise. The rms-noise is obtained by:

$$v_{rms} = \sqrt{\int \overline{v}_n^{\,2}(f)df} \quad (3.\ 6)$$

Where the integration is carried out over all the frequencies. The two most important frequency distributions for the spectral density are the white noise and the $1/f$ -noise.

3.2.2. White noise

This type of noise is independent from frequency and because of the spectral density is constant (in fact it exist in environment). Due to finite bandwidth in practical systems, this noise correspondingly is limited by capacitances, inductances and resistances with the shape of the transfer function of system.

3.2.3. 1/f noise

This noise is also known as flicker noise, too. As it is appear from subject, flicker noise id inversely proportional to the frequency. With increasing frequency, the effect of flicker noise on system will be lower. For MEMS devices, where advance measurement technique and Nano-scale are proposed, the mechanical $1/f$ noise is significant. The $1/f$ noise can be written as:

$$\overline{v}_{1/f} = \sqrt{\overline{v}_n{}^2 \frac{f_c}{f}} \quad (3.7)$$

Where f_c is the $1/f$ corner frequency determined as the frequency where the flicker noise and the White noise have equal magnitude as illustrated in Figure 3.2.

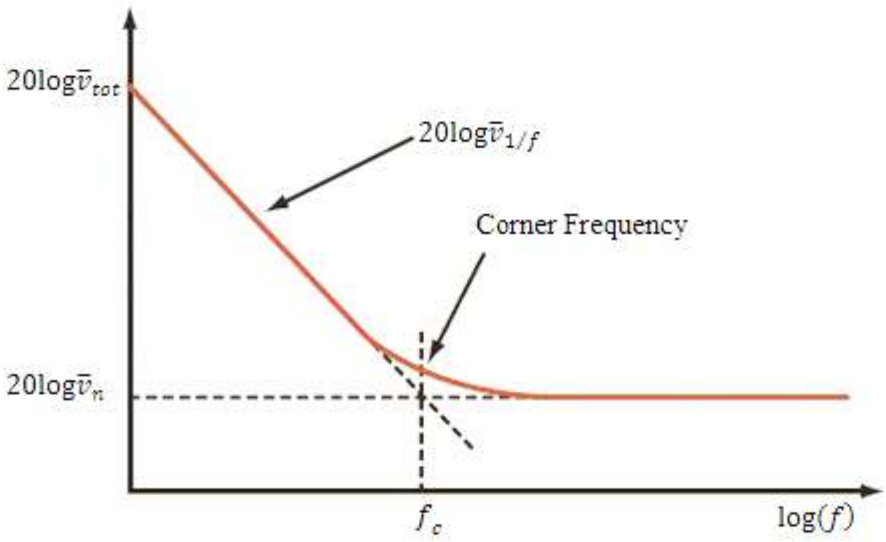

Figure 3. 2: Blew the corner frequency f_c, the flicker noise is greater than other noises.

Above diagram, define that $1/f$ noise is prevalent in low frequency, but it is not crucial limit. Because by proper scheme we can improve scheme, and design a resonator, which implement above the corner frequency, where the effort of reducing flicker noise can be costly and it is not economical.

3.3. Damping Vs. Quality Factor

Another important parameter in the performance of resonant structures is the damping effect that do not let resonator beam deflect more than maximum amplitude when it get excited by source energy. In the other definition if an undamped structure is allowed to vibrate freely, the magnitude of the oscillation is constant. In reality, however, energy is dissipated by the structure's motion and the magnitude of the oscillation decreases until the oscillation stops. This energy dissipation is known as damping.

The damping level is determined by its own quality factor, and the quality factor measures the amount of energy losses during operation of the resonant structure per cycle.

Then the total Q factor is equal to total energy stored in structure (E_M) to the energy lost per cycle (E_C) due to the damping effect:

$$Q = 2\pi \frac{E_M}{E_C} \quad (3.\ 8)$$

As we know, the equation of motion for a damped mechanical harmonic resonator is

$$m\ddot{x} + \gamma_{tot}\dot{x} + kx = F \quad (3.\ 9)$$

Where x is the displacement of mass m , γ_{tot} is the total damping coefficient, k is the spring constant and F is the excitation force (Lorentz Force). As it is seen, damping force is proportional to the mass velocity and damping coefficient is the sum of subset damping coefficient

$$\gamma_{tot} = \gamma_{anchor} + \gamma_{TED} + \gamma_{air} + \gamma_{Surface} + \gamma_{Other} \quad (3.\ 10)$$

The quality factor also can be defined as

$$Q_{tot} = 2\pi f_0 \frac{m}{\gamma_{tot}} \quad (3.\ 11)$$

We can also attribute a quality factor for each individual loss mechanism, so we can rewrite equation (3.10) like

$$\frac{1}{Q_{tot}} = \frac{1}{Q_{anchor}} + \frac{1}{Q_{TED}} + \frac{1}{Q_{air}} + \frac{1}{Q_{Surface}} + \frac{1}{Q_{Other}} \quad (3.\ 12)$$

3.3.1. Surface damping

The surface roughness, formation of the oxide layer, and surface contamination or doped impurities can reduce the resonator quality factor. In typical experiments the way to recognize this loss is, the quality factor is measured before and after baking treatment, if the quality factor is changed, this reduction is come back to surface losses. An especially surface loss is significant at nano-scale structure.

3.3.2. Thermoelastic damping (TED)

Thermoelastic damping, which arises when a material to cyclic stress, is an important factor when designing MEMS resonators. The stress brings about deformation, where materials heat under compressive stress and cool under tensile stress. Thus, due to the resulting heat flux, energy is lost to bring about this damping.

The magnitude of the energy loss depends on the vibrational frequency and the structure’s thermal relaxation time constant, which is the effective time that the material requires to relax after an applied constant stress or strain. Therefore, the effect of thermoelastic dissipation, and consequently the damping, is most pronounced when the vibration frequency is close to the thermal relaxation frequency.

Thermoelastic damping in vibrating beams was first studied by Clarence Zener (34). Let L be the length scale of the stress (and temperature) inhomogeneity, D the thermal diffusivity of the material and f the frequency of the resonator. Zener suggested the formula that governs the extent of dissipation (21).

$$\frac{fL^2}{D} \quad (3.\ 13)$$

When Eq. (3.13) is smaller than unity, the vibration is essentially isothermal and there is little dissipation. When this parameter is larger than unity, there is again little dissipation since the vibration is essentially adiabatic. Zener suggested that the maximum dissipation occurs when Eq. (3.13) is comparable to unity (21). A critical frequency can be identified:

$$f^* = \eta \frac{D}{L^2} = \eta \frac{k}{\rho C_p L^2} \quad (3.\ 14)$$

Where η is a constant of proportionality of order unity, k is the thermal conductivity, ρ is the density and C_p is the specific heat per unit mass at constant pressure.

For calculating Thermoelastic Damping (TED) analytically below equation is used:

$$Q^{-1} = \Delta \frac{\omega\tau}{1+(\omega\tau)^2} \quad (3.\ 15)$$

and

$$\Delta = \frac{E\alpha^2 T_0}{\rho C_P}, \tau = \frac{\rho C_P d^2}{k\pi^2} \quad (3.\ 16)$$

Where Δ is the relaxation strength, τ is the thermal relaxation time constant, T_0 is the absolute equilibrium temperature of the beam, E is Young's modulus with d as a thickness of beam and α is the coefficient of linear expansion. As it is clear from Eq. (3.15), damping is maximum when $\omega\tau$ is equal to unity then quality factor will be equal to $\Delta / 2$.

ThermoElastic Damping (TED) also is divided to its subset at higher frequency beside Zener damping which is discussed previously. Other parameters like as Intracrystalline Damping and Intercrystalline Damping will be add to description of TED in this situation (Higher Frequency around 10 GHz) (25).

Table 3. 1: properties of polysilicon in our experiment

Property	Value
Young's modulus (E) [Gpa]	160
Density (ρ) [kg/m³]	2330
Thermal expansion coefficient (α) [1/K]	2.60E-06
Thermal conductivity (kpoly) [W/mK]	90
Specific heat (Cp) [J/kg K]	712
Zero-stress temperature [K]	300

3.3.3. Anchor losses

When a MEMS device vibrates, some portion of the elastic energy propagates into the surrounding structure to which the device is attached. As previously mentioned, the lowest quality factors are obtained from clamp-clamp beam resonators (at cost of high frequency), because significant stress or strain is constrained by longitudinal and transverse vibration wave to supports.

A common assumption in much of the recent work analyzing anchor loss is that any energy leaving the device through the anchors never returns. Quantitative analysis of the anchor damping is unexpectedly difficult even with software like Coventorware. To model this loss of energy, the substrate is assumed to be semi-infinite in size. Elastic waves propagating from the attachment points, continue to infinity.

3.3.4. Material losses

The movement of the atomic level that results in heat is the source of the material losses and for each material; there is fundamental and individual limit for obtaining maximum quality factor. Material damping is influenced by temperature and resonant frequency. For justifying the dependency of the material damping is so complex, due to the vast number of physical mechanisms that contribute with it.

The intrinsic quality factor of the material damping can be defined by:

$$Q = \frac{E}{\mu_r \omega} \quad (3.\ 17)$$

Where μ_r and E are the viscosity and Young's modulus of the material respectively.

As it is seen from above Equation, we can rewrite it like:

$$f.Q = const. \quad (3.\ 18)$$

This is universal scaling law for material losses where f is frequency and Q is the quality factor. Table 3.2 for several materials has tabulated this law. As it is seen, single crystal and hard materials such as Lithium or Silicon have low intrinsic losses, while softer one have high losses such as metals or plastics.

Table 3. 2: the $f.Q$ -products for selected materials **(12)**.

Material	$E[GPa]$	$\rho[kg/m^3]$	$\mu_r[Ns/m^2]$	$f.Q[10^9]$
Aluminum	11	2700	1	1800
Epoxy	9	1210	2300	0.6
Fused Quartz	78	2200	3.1	4100
Gold	210	19700	78	420
Lithium	390	7300	0.7	91000
PVC	8	1380	490	2.6
Silicon	160	2320	2.5	10000

3.3.5. Air Damping

Viscous losses due to fluid flow (gas or liquid) commonly ambient air are often dominant loss mechanisms in MEMS structures. In account of reducing air damping most of MEMS devices are operated in lower pressure. Figure 3.3 illustrate the behavior of air damping in quality factor versus pressure. At pressure close to the atmospheric pressure, the quality factor is fixed and it means air damping is independent of pressure. This range is named *viscous regime*.

The transition from viscous regime to the *molecular regime* is characterized by the *mean free path* and subordinately *Knudsen number*.

In the atmospheric pressure, air mean free path is nearly 65 nm, which is small compared with the structure dimensions. Nevertheless, at lower pressure this value becomes comparable to characteristic device scale. At this region, air does not behave as viscous fluid constantly but interaction gas molecule and device molecule become loss mechanism.

Finally, at very low pressure, other loss mechanisms overcome to air damping and in this instance, quality factor is introduced by intrinsic losses why is titled *intrinsic regime.*

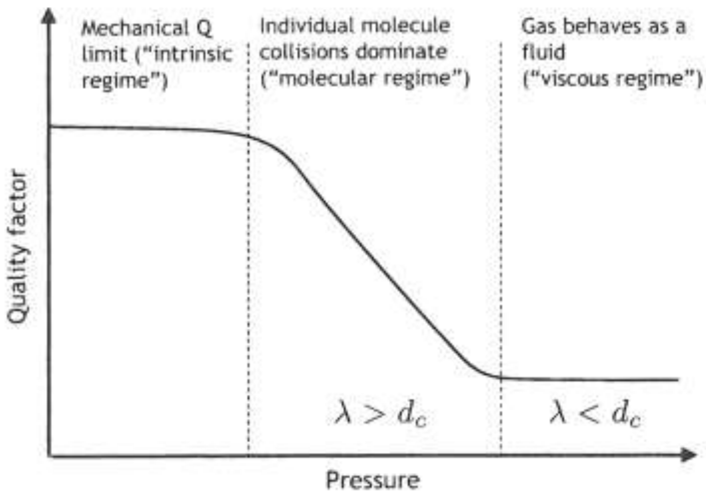

Figure 3. 3: The effect of Pressure on Quality factor**(12)**

3.3.5.1. Models for the air damping

In this section, air damping will be modeled. We should first define some topics like mean free path of gas molecules as a function of pressure and Knudsen number to characterize the transition from viscous to molecular regime. In continue, effective viscosity is introduced where into molecular regime, the classical continuum models are no longer valid. There are two important geometries that viscous damping is investigated. The Squeezed film effect, which is governed in parallel plate when a plate moves perpendicularly to its surface in many devices such as accelerometers and electrostatic resonators (Figure 3.4). The Couette flow models damping between two parallel plates when a plate moves horizontally to its surface (Figure 3.5).

In our sample, we just investigate squeezed film, because our structure is resonator and beam or membrane moves is perpendicular.

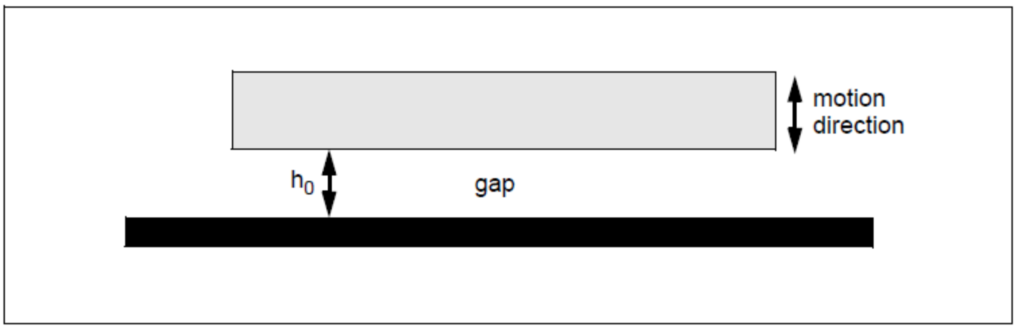

Figure 3. 4: Squeezed film Effect

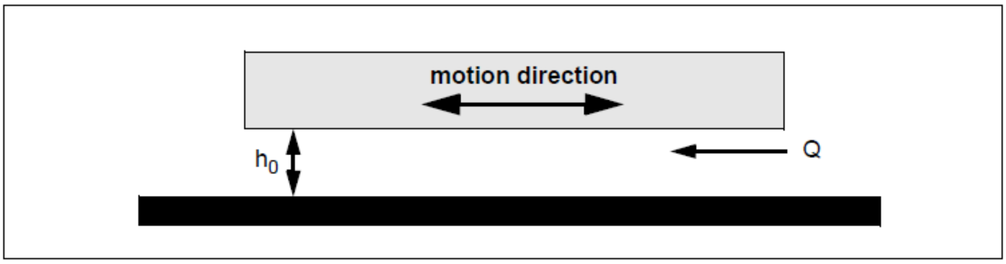

Figure 3. 5: Couetto flow

3.3.5.2. Mean free path & Knudsen number

As mentioned before gas velocity is independent of pressure in normal atmosphere pressure. This treat of gas velocity or viscosity is changed, when pressure is decreased and interactions between gas and device molecule become important. Then in this situation, the average distance of traveling of gas molecule before colliding with another molecule is introduced by λ (mean free path):

$$\lambda = \frac{1}{\sqrt{2}\pi {d_g}^2 n_V} \quad (3.\ 19)$$

Where d_g is the effective diameter of the gas molecules and n_V is the number of gas per unit volume. By using the ideal gas law, we can able to rewrite Equation (3.17) as:

$$n_V = N_A p / RT \quad (3.\ 20)$$

$$\lambda = \frac{RT}{\sqrt{2} {d_g}^2 N_A p} \quad (3.\ 21)$$

Where $N_A = 6.022 \times 10^{23}$ 1/mol is the Avogadro's number, $R = 8.3145$ J/mol.K is the universal gas constant, p is the pressure and T is the gas temperature. According to last Equation, the mean free path is inversely proportional to gas pressure.

The ratio of mean free path λ to critical device dimension d_c (in our sample it is gap distance between the beam and substrate) is defined as the Knudsen number

$$K_n = \frac{\lambda}{d_c} \quad (3.\ 22)$$

Or

$$K_n = \frac{\lambda_{PF}.P_{REF}}{P_{AMB}.d_c}$$

Where λ_{PF} , P_{REF} and P_{AMB} are mean free path, reference pressure, and operative pressure respectively. If the Knudsen number was greater than 1, the gas molecule collision with device is more probable than collision with other gas molecules and the gas begins to lose cohesive nature.

The gas flow is typically divided to three regimes:

a. In the *continuum region* $K_n < 0.1$ and the continuum flow models are valid.

b. In the *transition region* $0.1 < K_n < 10$, the gas molecular effects start to be significant and the continuum models need to be modified.

c. In the molecular region $K_n > 10$, the gas molecule interactions are no longer significant and continuum models cease to be valid.

For typical engineering problems, the characteristic length is much larger than the mean free path; therefore, the continuum approximation is always valid. However, this may not always be true in MEMS, especially for damping problems, because the typical film (gap) thickness is of the order of one micron or hundred nanometer and ambient pressure can be low. As the film thickness decreases, the mean free path of gas molecules becomes comparable to the film thickness. For example, the mean free path for air (at 25˚C and atmosphere pressure) is about 0.065µm. If the film thickness is 0.5µm, then K_n is 0.13, which is a transition regime. The mean free path may be decreased either by decreasing the ambient temperature or by increasing the ambient pressure.

3.3.5.3. Squeeze film damping

Figure 3.6 illustrate the squeeze film effect when two or one surface moves to each other. A typical situation in MEMS components consists in a fluid (air) that fills the space between two parallel flat electrodes. The first one is fixed (substrate), the second is moved by electrostatic force like Lorentz force with velocity v(f), which is function of frequency. As a gap between two plates is reduced, the volume is reduced, too. Then a little displacement of the mobile plate will provoke the entrance or the exit of a flux of gas. In both states, the viscosity of the fluid limits the flux of the gas; this brings to a pressure distribution on the superior electrode. Therefore a pressure force opposing to the motion of the mobile plate originates; this force is called Squeeze Film Damping method (35).

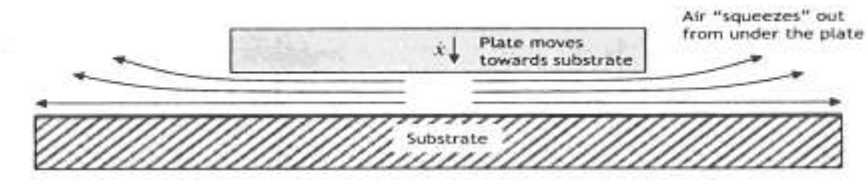

Figure 3. 6: Schematic of Squeeze film damping. As the plate moves toward substrate, air flows from under the plate**(35)**.

At Figure3.7, the behavior of the fluid has been modeled by a spring and a damper in parallel with a concentrated parameter, where also the mass m and the stiffness k of the MEMS appears besides the spring K_a and the damper C_a.

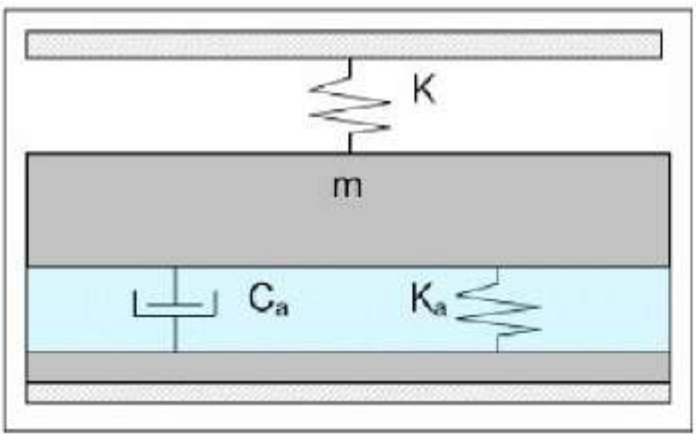

Figure 3. 7: Concentrated Parameters Model.

At low frequencies, air can escape with little resistance and the force is small then damping effect is prevalent. At high frequencies, the air is held captive by its own inertia. Essentially, there is not enough time for the air to move out of the way, as the structure oscillates. Then air is compressed and spring force become dominant. However, remember that the damping force itself is caused by viscous stresses.

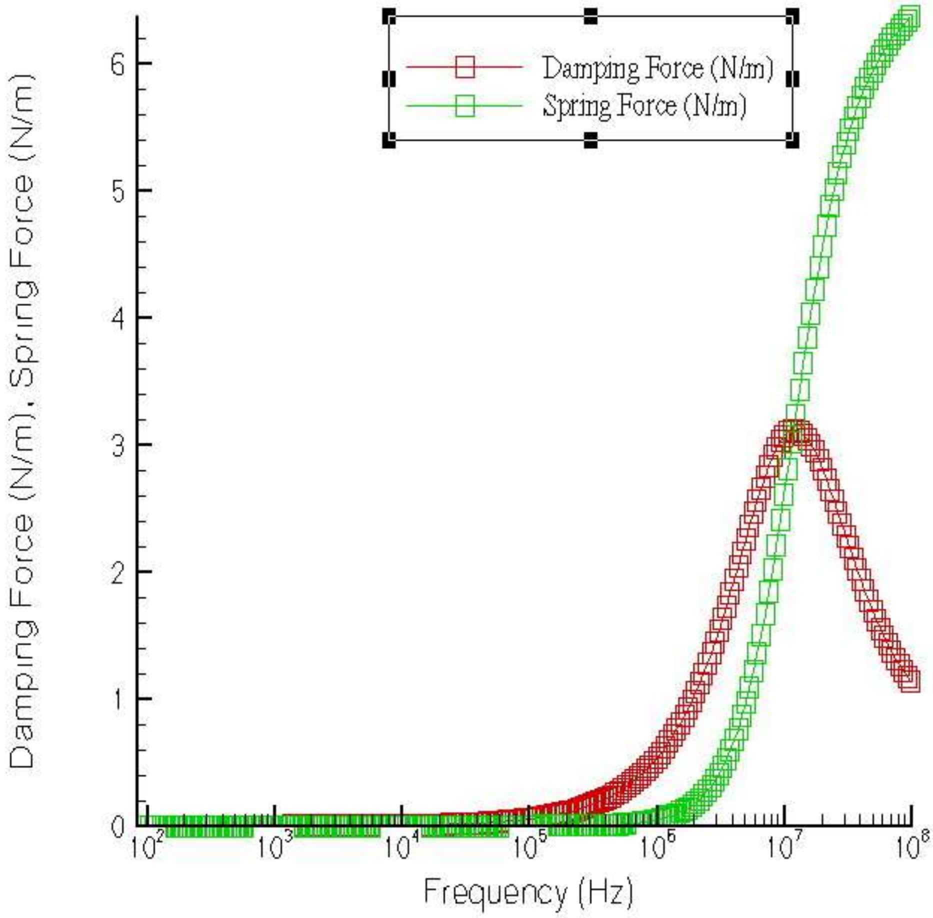

Figure 3. 8: Frequency characteristics of the damping force and spring force.

If the gas compresses and does not move much, then the damping force will be lower. This explains why the damping gets smaller as the frequency increases above several GHz. The frequency at which the stiff behavior prevails over the damp one is called *cut-off* (Figure 3.8).

Before calculating analytically Squeeze film damping coefficient and spring constant, we should introduce effective viscosity, which is, depend on gas pressure when Knudsen number is large. The effective viscosity for the Squeeze film damping in narrow gap is (30):

$$\mu_{eff} = \frac{\mu}{1 + 9.638 K_n^{1.159}} \quad (3.\ 23)$$

Where μ is the viscosity in normal conditions, in fact when $K_n << 0.1$. Nevertheless, at low pressure, when $K_n > 0.1$ with decreasing pressure as it is seen from Equation (3.21) viscosity is decreased.

Then by using of effective viscosity, we are able to define C_a and K_a formula in for a solid plate:

$$C_a = \frac{64\sigma pA}{\pi^6 d\omega} \sum_{m,n-odd} \frac{m^2 + c^2 n^2}{(mn)^2[(m^2 + c^2 n^2)^2 + \sigma^2 / \pi^4]} \quad (3.\ 24)$$

$$K_a = \frac{64\sigma^2 pA}{\pi^8 d} \sum_{m,n-odd} \frac{1}{(mn)^2[(m^2 + c^2 n^2)^2 + \sigma^2 / \pi^4]} \quad (3.\ 25)$$

Where m and n are odd integers, p is the pressure, $c = W / L$ is the ratio width to length of beam or membrane, ω Is the frequency of vibration and the squeeze number σ is:

$$\sigma = \frac{12\mu_{eff} W^2}{pd^2} \omega \quad (3.\ 26)$$

A high Squeeze number means that the gas in the narrow gap behaves like a spring and for a low amount, the gas acts as a damper.

3.4. Conclusion Of Concept

In this section, our specific clamped-clamped resonant magnetometer has been discussed. Possible formulas, problems, and limitations for each resonant magnetometer that always faced with them also have been mentioned, i.e. analytical formula for calculating resonant, quality factor calculation with their related formulas which are shown why most of this sensors implement in vacuum circumstance, etc.

4. FABRICATION OF MAGNETOMETER

For fabrication magnetometer, we tried at first to implement it with fine grain polysilicon as active layer. Because providing polysilicon layer on silicon oxide layer with silicon as a substrate is less expensive than stock SOI wafer. Therefore, we would like to explain steps of producing wafer with polysilicon layer and declare why SOI wafer were preferred.

For our process, we used three mask levels for SOI based technology: POLY, METALPAD, and CAVITY. However, at first when we wanted to implement it by polysilicon, we did not utilize CAVITY mask, but it will be discussed at BHF Release part.

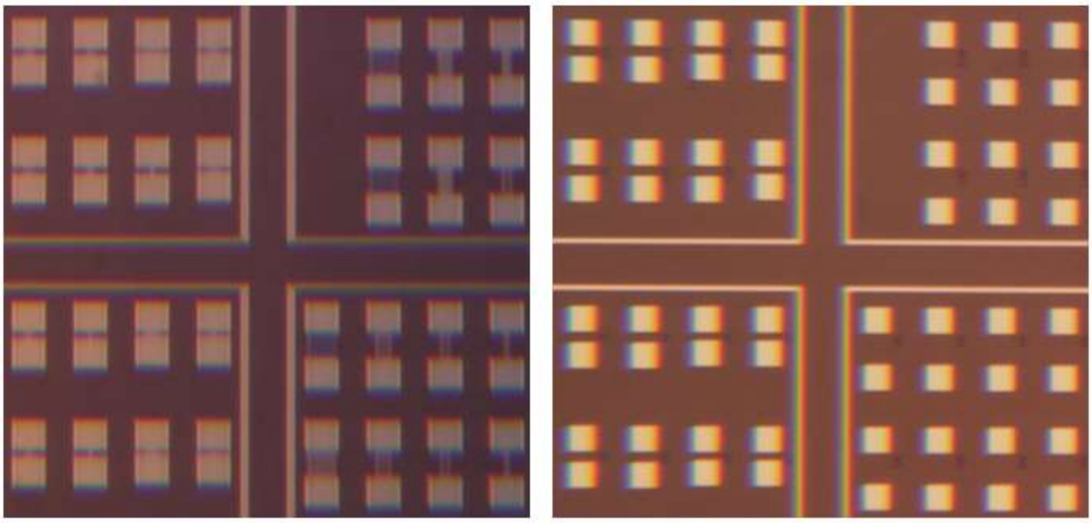

Figure 4. 1: Partial of two light masks, POLY (*left*), METALPAD (*right*) (the darker area is empty).

In this section, we will show how a wafer is provided individually by process flow and discuss about some features of specific structures and their characteristics.

4.1. Process Fabrication of Silicon wafer

4.1.1. Thermal oxide:

Silicon dioxide, SiO_2, is probably a more important material in silicon technology than silicon itself, because Silicon oxide, protect its surfaces and has functions as capacitor dielectric and isolation material. Even in some application like our process, it is used as insulator and sacrificial layer, too. Generally, Oxides are used alternatingly many times during silicon processing as a masking material for diffusion or etching, and as a cleaning method to reclaim perfect silicon surface.

Two basic oxidation schemes are used: wet (steam) and dry oxidation.

Wet oxidation: $Si (s) + 2H_2O (g) \rightarrow SiO_2 (s) + 2H_2 (g)$

Dry oxidation: $Si (s) + O_2 (g) \rightarrow SiO_2 (s)$

"Thermal oxidation is a slow process: dry oxidation at 900◦ C for 1 h produces 20nm thick oxide and wet oxidation for 1 h produces 170nm. Exact values are dependent on silicon crystal orientation: oxidation rate of <111> is somewhat higher than that of <100> silicon; highly doped silicon oxidizes faster than lightly doped material, and the higher the oxygen pressure, the higher the rate"(7).

At our testing, thicker oxides are used for device isolation and as masking layers for etching steps. By wet oxidation during three and half hours at 1000˚ C temperature approximately 400nm thickness of oxide was grown by LPCVD.

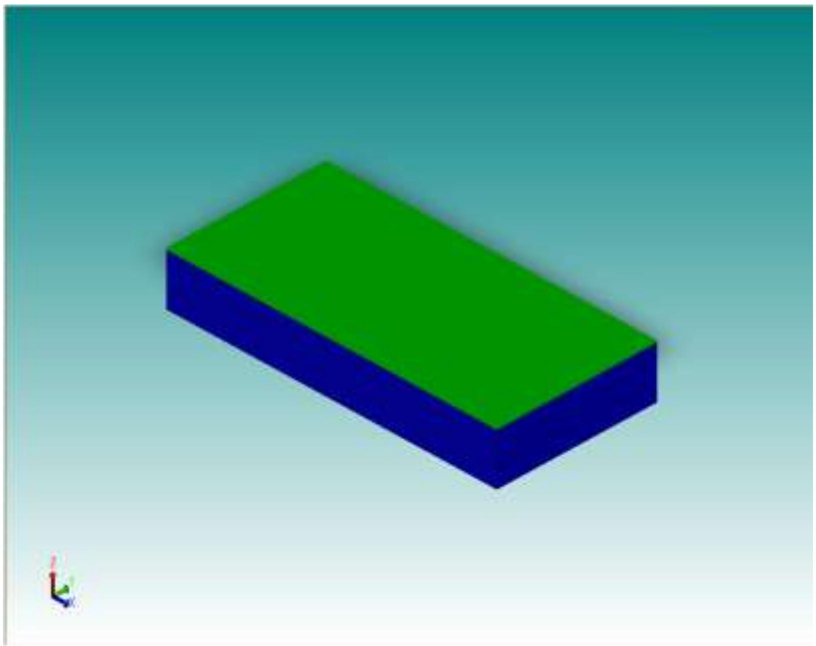

Figure 4. 2: Blue layer is substrate (silicon) and green layer is thermal oxide

4.1.2. Deposition & doping polysilicon:

Polysilicon (polycrystalline silicon) is chemical-vapor deposited by the silane decomposition reaction

$SiH4$ (g) → Si (s) + 2H2 (g) 630 ◦C, 400mTorr (rate ≈ 10 nm/min)

Polysilicon deposition can be done either in the correctly polycrystalline or in the amorphous (microcrystalline) regime. At 630˚ C, Grain size of film deposited is 30 to 300nm, which is similar to thicknesses in some applications like our work that is 80nm. For deposition between 580 and 600˚ C, grain size decreases and deposition at 570˚ C, results in amorphous film. These variations in temperatures affect surface morphology, final grain size after annealing and doping uniformity. Polysilicon deposition is done generally undoped and undoped polysilicon is not a conductor at all, so in some applications it can be used like an insulator. Therefore, if we want to use it as a conductor, it can be doped by ion implantation or thermal diffusion processes at 900 to 1000˚ C just like single crystal silicon. B_2H_6 gas is used for p-type doping and $POCl_3$ for n-type doping. However, there is the alternative method of using solid P_2O_5 wafers as like we used: phosphorous oxide wafers and silicon wafers are set in alternating positions in a wafer boat, and at 900˚C, temperature the phosphorus will evaporate from P2O5 wafers and dope the polysilicon. Dopants arrive on the wafer from the gas phase, and dopant supply is practically infinite.

Then for controlling the amount of doping experimentally, we held it in furnace 30 min and 1.8×10^{2} ohm/sq. was exhibited. High doping levels of 10^{21} cm^{-3} results in polysilicon resistivity of 500µohm-cm. Electron mobility in polysilicon is an order of magnitude less than in single crystalline materials, 10 to 50 cm^2/Vs. This is doping dependent, and strongly dependent on deposition and annealing cycles.

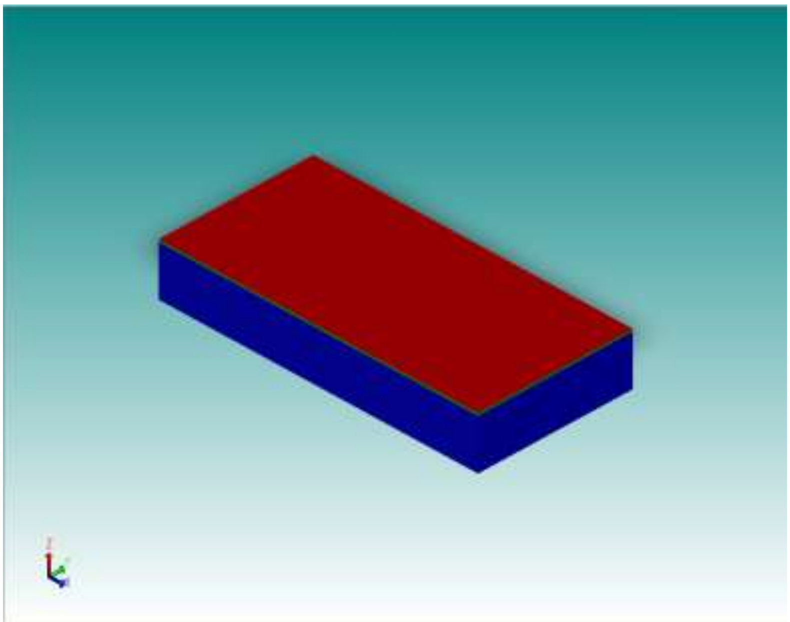

Figure 4. 3: Red layer nominate Polysilicon.

4.1.3. Optical Lithography

In any lithography, we have four major steps with specific features, there are:

a. Photoresist film which are negative or positive
b. Alignment of mask and wafer
c. Exposure of the photoresist
d. Photoresist developer

a.) During the all our process always, the type of the positive photoresist with light mask type has been used. Figure 4.4 illustrate these two types of mask and positive photoresist behavior.

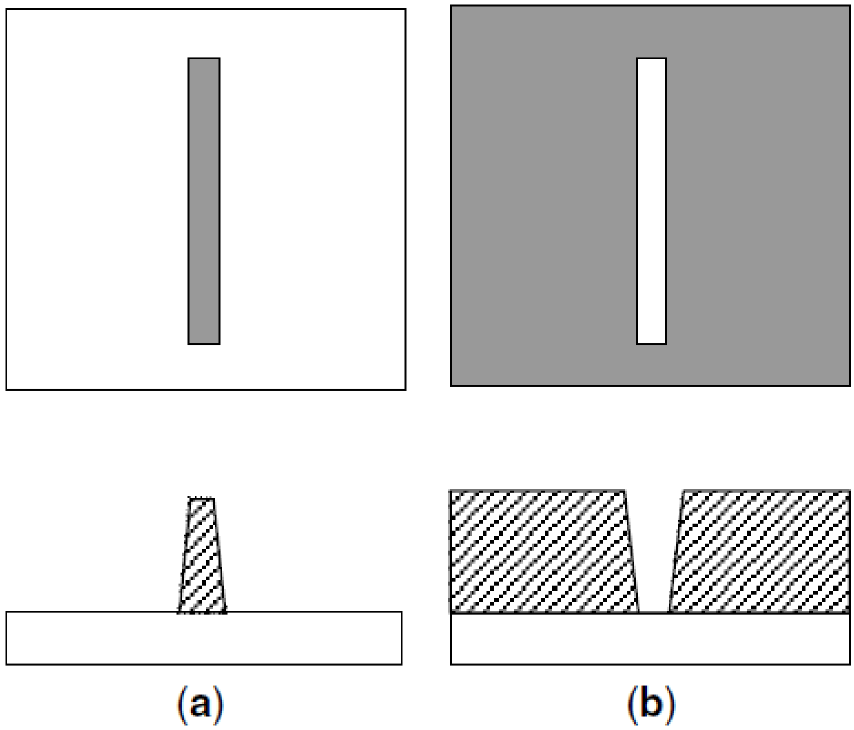

Figure 4. 4: Behavior of positive photoresist versus (a) Light Mask and (b) Dark Mask after development**(7)**

b.) Due to micro devices are built-up layer-by-layer, overlay of successive layers relative to previous layers is so important. Therefore, by specific spots on the wafer which has been created with first mask, (alignment marks or keys) alignment of remain mask is implemented on base of it. Figure 4.5 illustrate the samples of these marks as well.

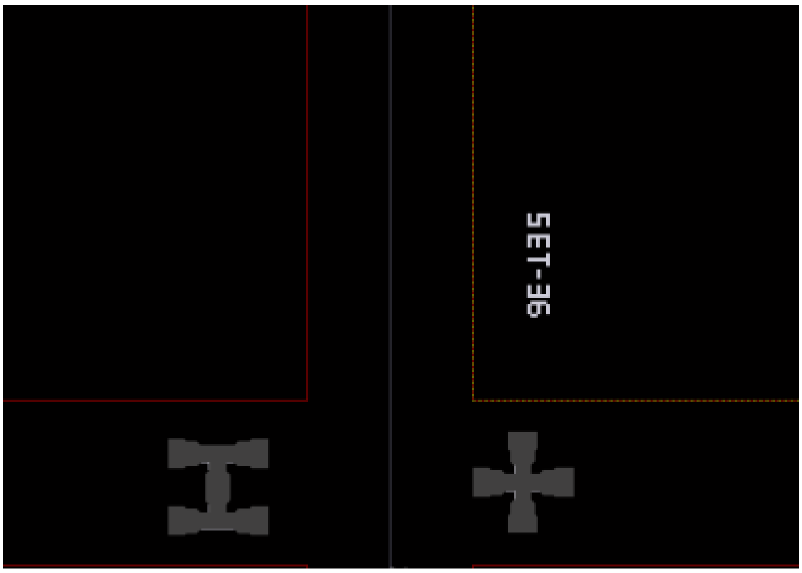

Figure 4. 5: Alignment Marks which is used in our trials.

Alignment is usually done on a wafer level, with two alignment marks as far from each other as possible, to increase theta (rotational) resolution (Figure 4.6).

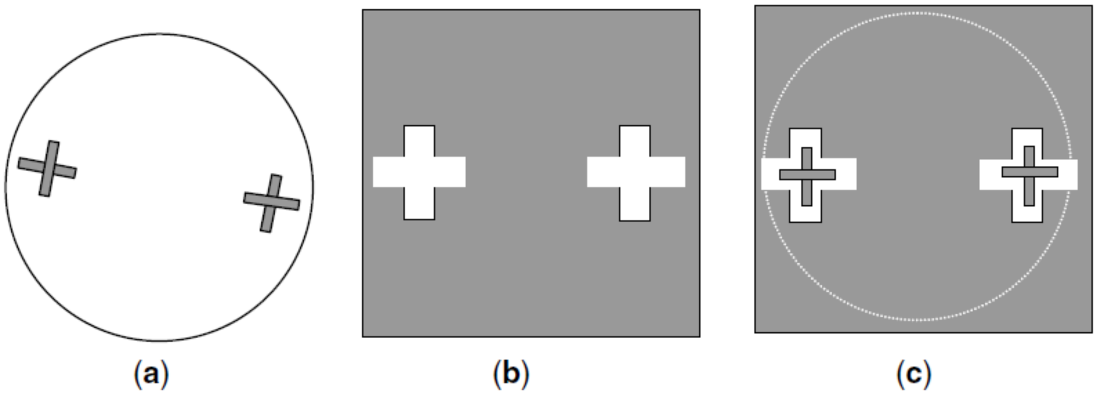

Figure 4. 6: Alignment operation: (a) wafer with alignment marks; (b) mask with alignment marks and (c) after linear translation and rotation of the wafer the alignment marks on wafer and mask coincide**(7)**.

c.) After the alignment, the specimen is exposed by UV radiation, but this

Exposing was different in our process where we used two type of the lithography method.

At Positive Lithography without of any changing in the process normally after alignment, UV radiation is exposed 3.2 seconds and it is ready to developing step. But, into Lift-off Lithography after the alignment, for 2 seconds UV is exposed to sample and after that wafer is baked at 120˚ C for one and half minute to become stiffer the area has been exposed. Then, after baking wafer is exposed again without of mask for 6 seconds by UV radiation. In this method, indeed we prepare wafer for the lift-off metallization process.

After lithography depends on process, there are various steps which Figure 4.7 illustrates some of them.

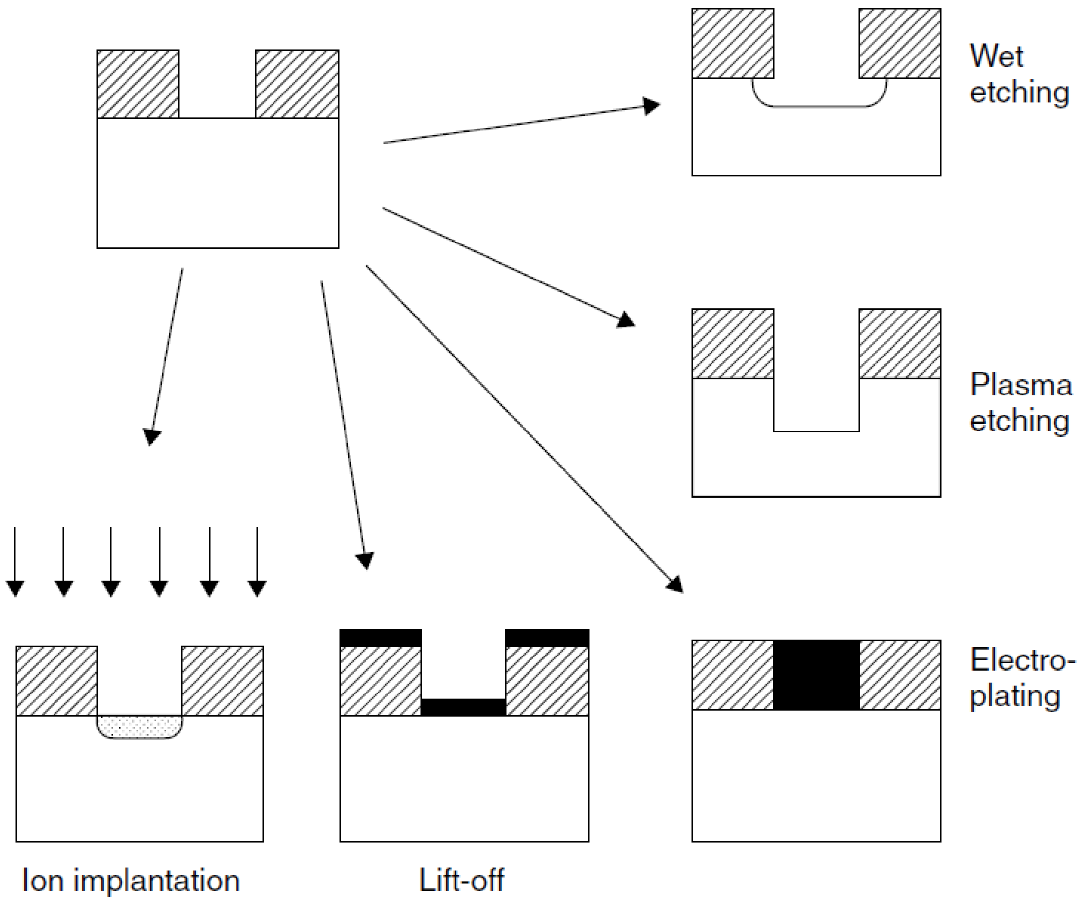

Figure 4. 7: Processing after lithography**(7)**

4.1.4. Lift-off metallization

During this step, metal layer completely covers silicon surface with identical thickness everywhere. Then followed by resist dissolution in solvent and lift-off, with all the metal that is not in contact with the former layer being removed (Figure 4.8).

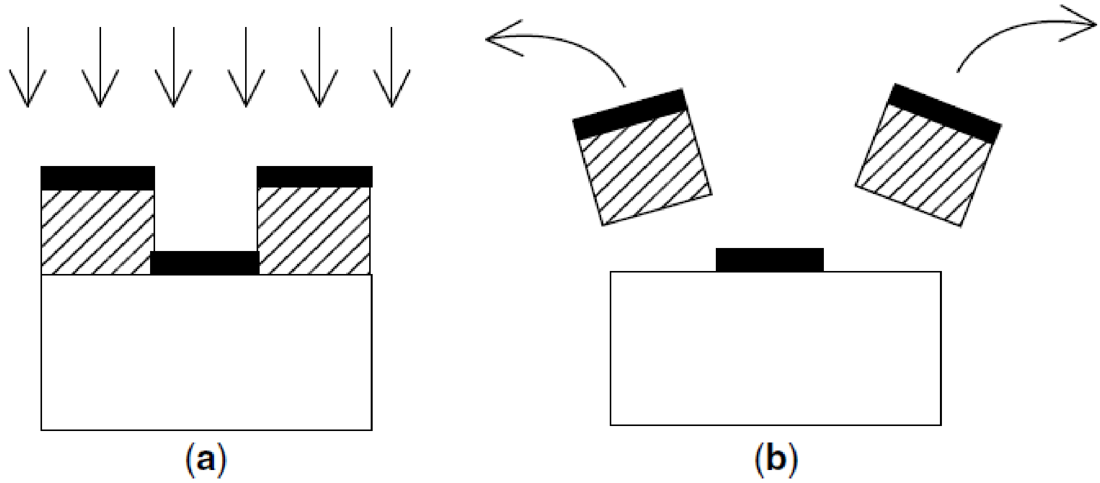

Figure 4.8: Lift-off process (a) metal deposition on resist pattern and (b) resist dissolution and metal lift-off**(7)**

In our case, we used Aluminum as contact layer of low resistivity layer, which is Polysilicon. We used HNO_3 Fuming acid for dissolve photoresist as well as for accelerating of dissolvent, Sonic Vibrator was very useful. However, in some structures, because of the continuity of metal over other layers after the lift off some of samples remained without of metal contact (Figure 4.9)

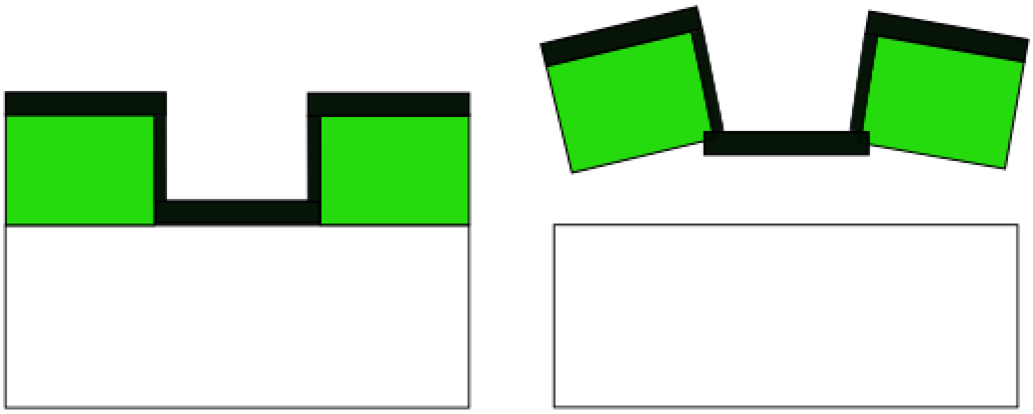

Figure 4. 9: Continuity of metal over layers, bring about lift off metal completely even from contact patch

In our case, AL thickness was 600 nm and as it has been illustrated in figure 4.10, they have been presented by yellow color on top of the polysilicon layer.

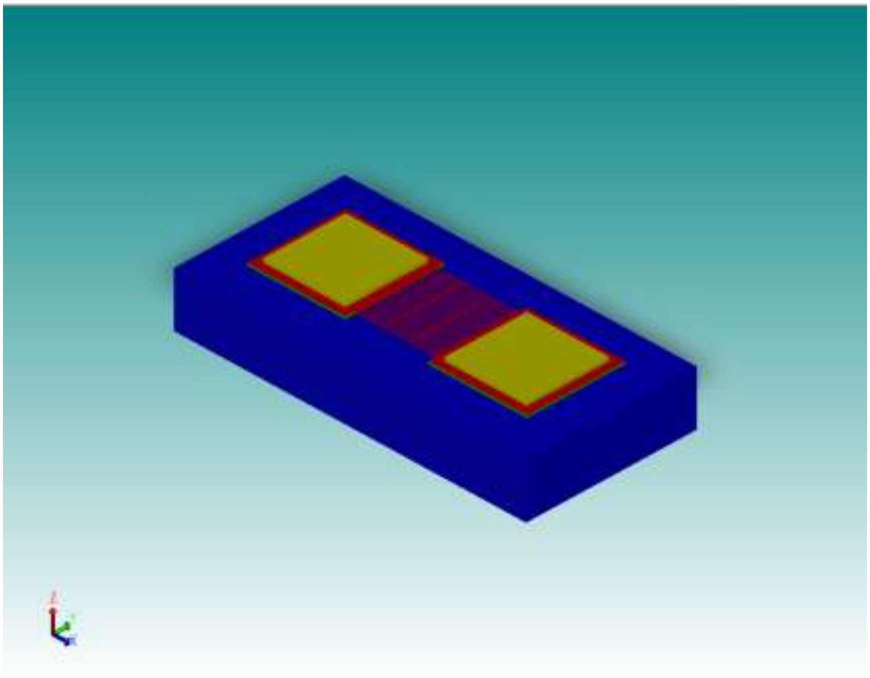

Figure 4.10: Yellow layer present Al Contact

4.1.5. HF releasing

Previously, we discussed about the any type of the oxides, but here those types are also very influenced at etching rate, too. For instance, higher deposition temperature usually leads to denser films to be deposited. Therefore, it becomes more resistant to etching and less prone to moisture absorption.

"Thermal oxide etch rate in hydrofluoric acid (HF) is always the same, irrespective of the furnace that was used to grow it. In CVD and in PECVD in particular, films can have HF etch rates varying enormously depending on the particular type of equipment and process conditions (power, flow rate and ratios, temperature)"(7).

As it was mentioned before at Thermal Oxide part, our oxidation is produced by LPCVD mechanism and after immersing our samples into pure HF for 1 minute, etching rate became $1.5-2\mu m/\min$. The bars, which are available on wafers, calculate the etching rate (figure 4.11). After the etching, some of them completely etched and remain, did not, so with knowing of bar's width dimension we are able to define etching rate.

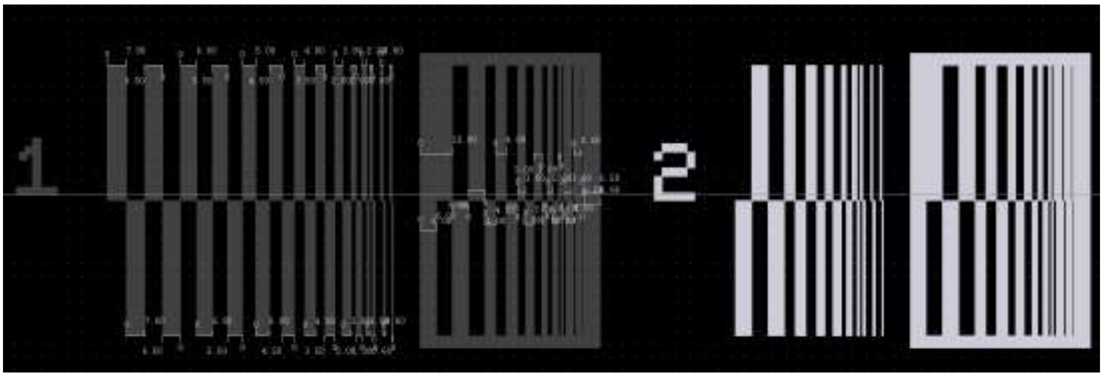

Figure 4.11: Etching bar definer, with definite dimension.

Pure HF release is one of the alternative methods at oxide etching where there is metal like Aluminum, because the rate of the etching Al goes up when HF concentration decreases and water has an active role in aluminum surface oxidation. For instance, 49% HF etches aluminum 38 nm/min, but HF:H2O (1:10) results in 320 nm/min rate(7).

4.1.6. Critical point dryer (CPD)

Air (evaporative) drying of specimens can cause severe deformation and collapse of structure - the fundamental cause of such damage being the effects of surface tension. The specimen is subject to considerable forces, which are present at the phase boundary as the liquid evaporates. The most common specimen medium, water, has a high surface tension to air; by comparison, that for Isopropyl Alcohol (IPA) is considerably lower. Then it is better to substitute a liquid with a lower surface tension for reduce damage, during air-drying.

However, the occurrence of what is known as 'continuity of state' suggests a drying technique for which the surface tension can be reduced to zero. If the temperature of liquefied gas is increased, the meniscus becomes flatter indicating a reduction in the surface tension. If the surface tension becomes very small, the liquid surface becomes very unsteady and ultimately disappears.

When this 'critical point' is reached, it is possible to pass from liquid to gas without any abrupt change in state. If a specimen had been in the liquid during this process it would have experienced a transition from a ‘wet’ to a 'dry' gas environment without being in contact with a surface, in this way avoiding the damaging effects of surface tension. This is termed Critical Point Drying (CPD), the basis of which are the classic experiments carried out over 100 years ago during investigations on the liquification of gases.

Critical point drying is an established method of dehydrating biological tissue prior to examination in the Scanning Electron Microscope. The technique was first introduced commercially for SEM specimen preparation by Polaron Ltd in 1971.

Perceptibly, below phase diagram exhibit the pressure to temperature ranges where solid, liquid and vapor exist. The boundaries between the phases meet at a point on the graph called the triple point. Along the boundary between the liquid and vapor phases, it is possible to choose a particular temperature and corresponding pressure, where liquid and vapor can co-exist and hence have the same density. This is the critical temperature and pressure.

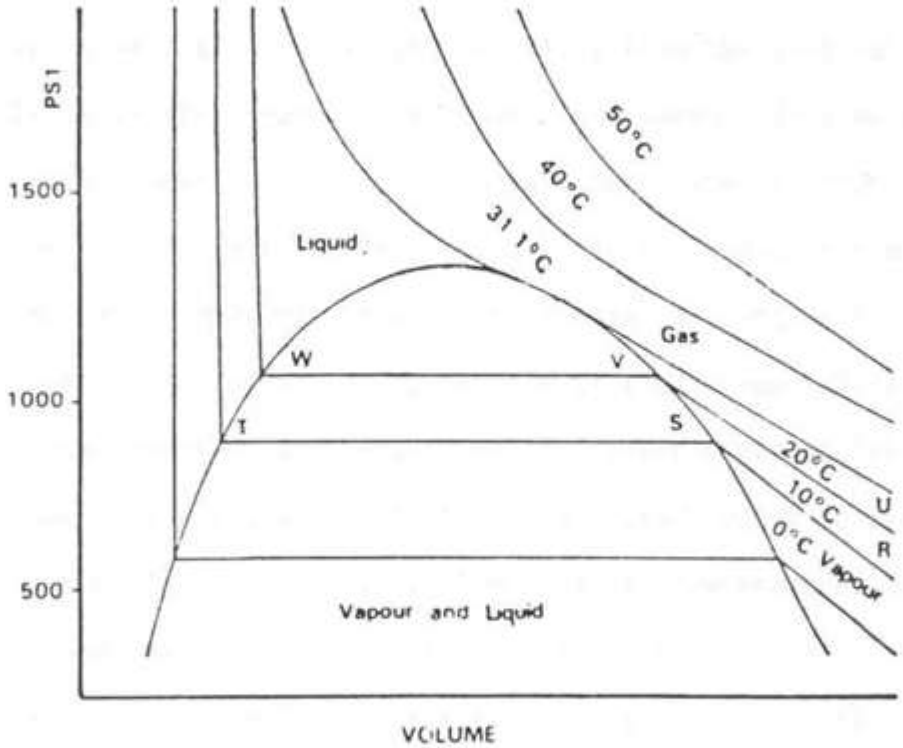

Figure 4.12: Phase Diagram of CO_2

Consider first the 10° C isothermal at low applied pressure. The CO2 is gaseous (vapor) and generally exhibits the characteristics of a gas (Boyle’s Law) over the range from 'r' to 's'. From point 's' a very slight increase in pressure results in a change from vapor state to the liquid state. This is the phenomena of saturation. From 's' to 't' the pressure is virtually constant while the volume is decreasing and at 't' the substance is all liquid. From point 't' the graph becomes almost vertical indicating significant application of pressures for very little change in volume, liquids being virtually incompressible.

This indicates that the densities of the saturated vapor and liquid are approaching each other, also the slight departure from the vertical 'w' shows the compressibility is greater than that at higher pressures. This shows that the properties of the liquid and gas states of the substance are becoming similar and will ultimately coincide. This in fact is realized at the 31.1°C isothermal, which does not show any horizontal discontinuity. The temperature at which this occurs is termed the Critical Temperature and has an associated Critical Pressure and Density and hence for a particular mass of gas, a Critical Volume. If a liquid was heated in a closed system so that the critical pressure could be attained, at the critical temperature, any visible meniscus would disappear; the surface tension would be zero and it would not be possible to distinguish between the properties of a liquid or a gas. We therefore have continuity of state. Above this temperature, the gas cannot be liquified by the addition of pressure and strictly speaking a substance should only be classified as a gas above its critical temperature, below this temperature where it could possibly be liquified by the application of pressure, it is more precisely termed a vapor.

Critical point drying relies on this physical principle. The water in biological tissue is replaced with a suitable inert fluid whose critical temperature for a realizable pressure is just above ambient. The choice of fluids is severely limited and CO2 is universally used today.

With CO2, a critical point of approximately 35°C can be achieved at a pressure of around 1,200psi. Therefore if the water is replaced with liquid CO2 and the temperature then raised to above the critical temperature, the liquid CO2 changes to vapor without change of density and therefore without surface tension effects which distort morphology and ultra-structure.

Since liquid CO2 is not sufficiently miscible with water, it is necessary to use an intermediate fluid, which is miscible with both water and liquid CO2. In practice, intermediate fluids commonly used are methanol, ethanol, amyl acetate and acetone.

Table 4.1 show critical constants for some common substances. Even the practical achievement of the critical conditions would not assist the biologist, as the specimens would suffer significant thermal damage if we attempted to apply the technique direct for the removal of water from specimens.

Table 4. 1: Critical Constant

Substance	Temperature ˚C	PSI
HYDROGEN	-234.5	294
OXYGEN	-118	735
NITROGEN	-146	485
CARBON DIOXIDE	31.1	1072
CARBON MONOXIDE	141.1	528
WATER	374	3212

The critical phenomena can be utilized as a drying technique as it achieves a phase change from liquid to dry gas without the effects of surface tension and is therefore suitable for delicate biological specimens.

4.2. Process Fabrication for SOI Wafer

4.2.1. SOI wafer

SOI wafer serves as a platform for companies and universities, to manufacture MEMS based structures cheaper. The standardized manufacturing process enables the fabrication of MEMS at low cost because several users share the same slice. This sharing enables a reduction in price, nevertheless imposes a strict set of rules.

The intact and SOI wafer is illustrated at Figure 4.13 SOI is the abbreviation of Silicon On Insulator. The slice consists of a superposition of three layers: Silicon, Oxide, and Silicon substrate (the last layer is now been systematically called substrate to avoid confusion). The thicknesses of these layers are shown in Table 4.2.

Table 4. 2: Layer Thickness of SOI wafer

LAYER	THICKNESS
Silicon	$140 \pm 5nm$
Oxide	$400 \pm 10nm$
Substrate	$400 \pm 5\mu m$

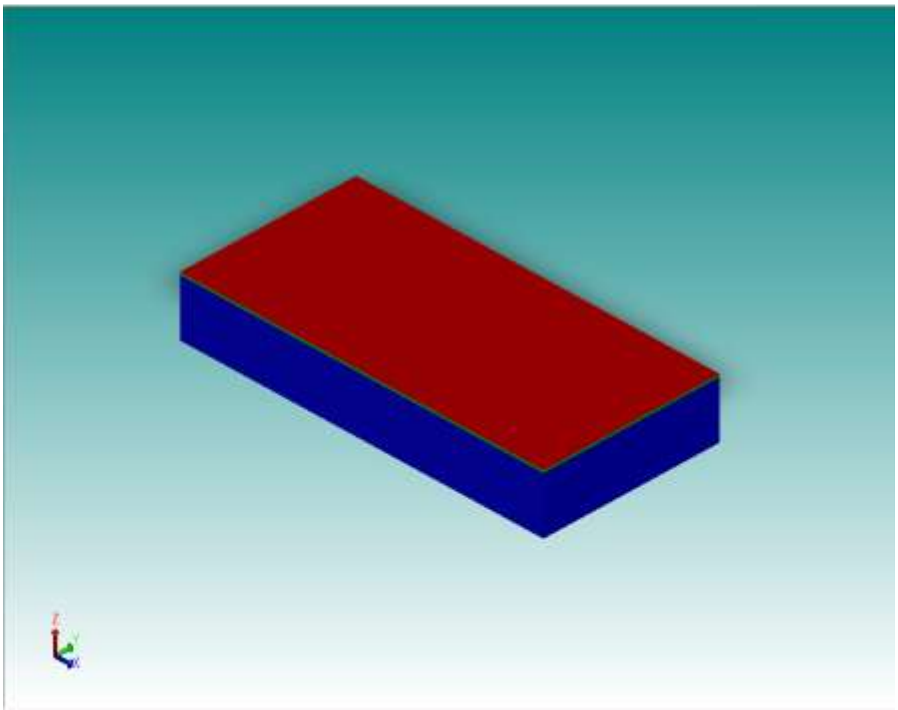

Figure 4.13: Substrate Blue, Oxide Green, and Silicon Red

As it is seen from SOI wafer we do not need anymore thermal oxidation and deposition part where was discussed in previous section But, other steps is implemented with minor differences identically. For instance SOI wafer processes, is started from doping phosphorous to increase conductivity of silicon layer and instead of 30 min (time that was kept polysilicon into doping furnace), 60 min is proposed.

The major differences between process flows of the bulk silicon with SOI wafer are using the third mask and consequently regarding to it releasing step. Therefore, in this section we express this step only.

4.2.2. BHF releasing

Before explain what the BHF (Buffered HF) is, it will better to mention why we used the third mask (CAVITY)!

Due to the high etch rate of HF, etching control is a little bit difficult, so BHF is other solvent of oxide with lower etching rate. Nevertheless, BHF is the solvent of Al, too. Hereby, we should avoid Al contact part from BHF and the best way is covering these areas with photoresist. As it is seen from figure 4.14, CAVITY mask is a dark mask and whole of structures are covered by photoresist except beam or membrane areas. So, expected under etch of membrane is attainable.

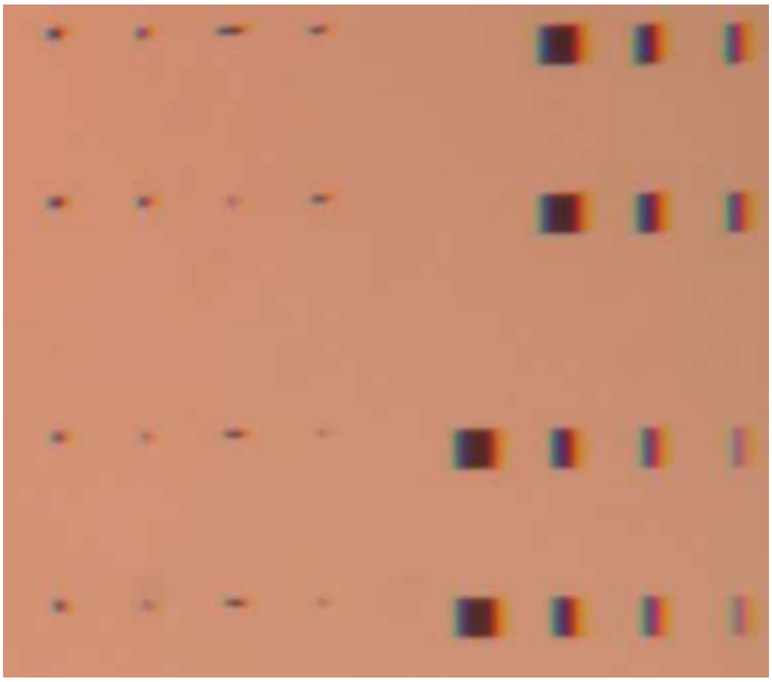

Figure 4.14: A partial of CAVITY mask

We used NH_4 40% : HF 49% (7 : 1) BHF for our experiments and we empirically calculated etching rate around 60nm - 65nm per minute for thermal oxidation of SOI wafer.

After immersing sample in BHF for 23 min the desired under etch was revealed (Figure 4.15). As it is observed, there is a taper shape at anchor region. The upper side has been etched 1.75µm and lower 1.90µm that shows it is enough. Because we design each perforation in membrane with maximum 2µm distance from each other and etching each one from both sides with this rate, we can be sure there is not any silicon oxide anymore under any membrane.

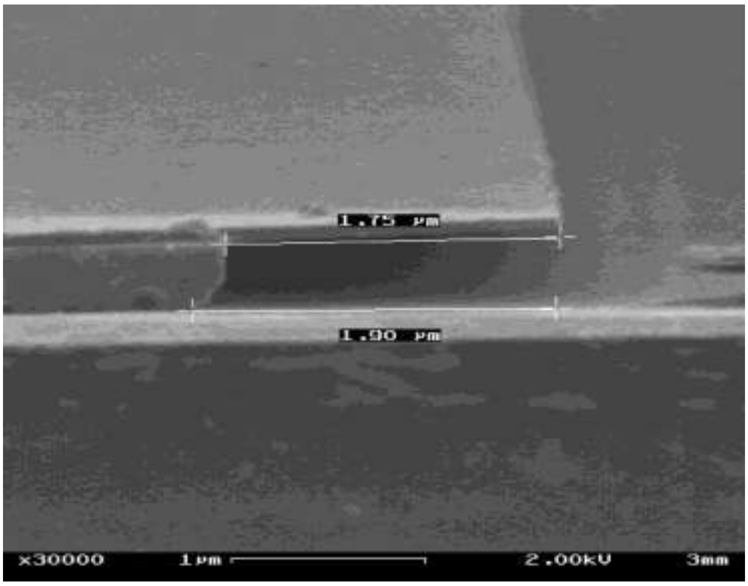

Figure 4.15: Etching silicon oxide with BHF solvent for 23 min

Figure4.16 shows the final state of the structures where photoresist also has been removed from everywhere. One of the obstacles was removing photoresist from wafer after CPD (Figure 4.17). As we know after the CPD we are not allowed to immerse sample in any liquid (because of the suspended membrane), so for removing photoresist we used plasma etching. However, after that all of the long sensors became ruined due to the high power electrical environment inside the chamber of Plasma.

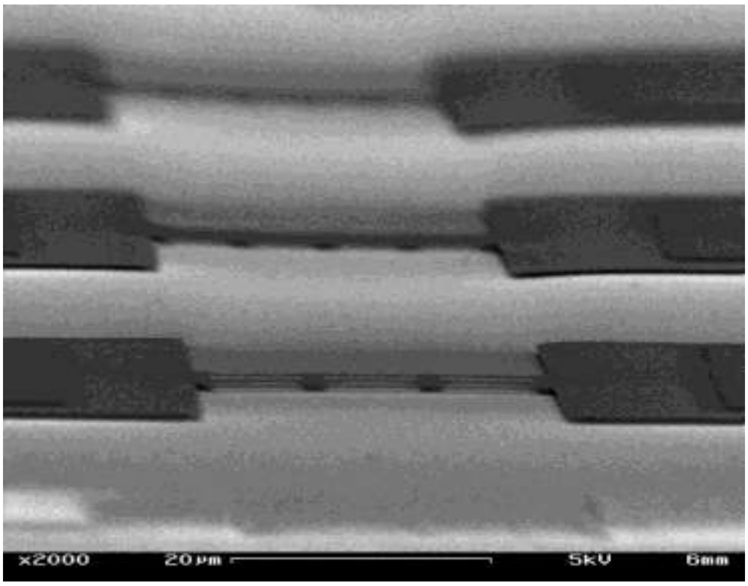

Figure 4.16: Completed state of the three structures.

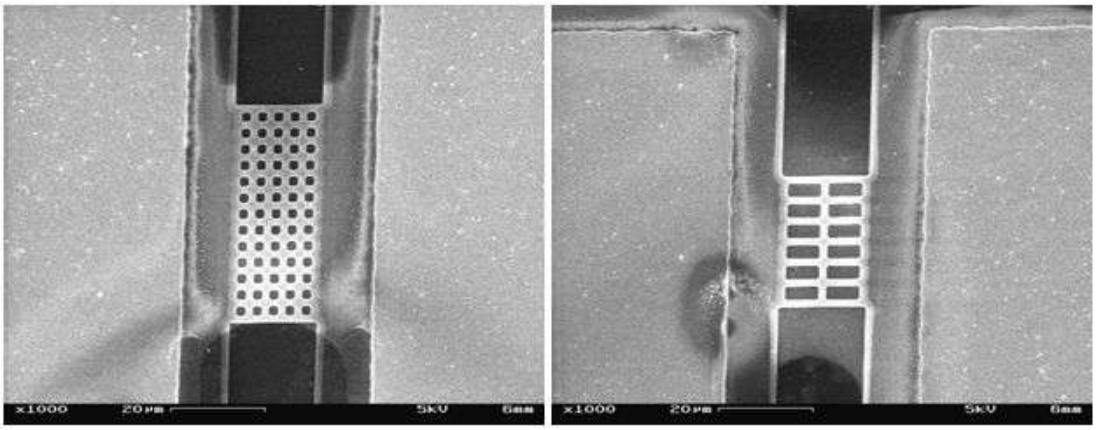

Figure 4.17: Without using Acetone there is still photoresist everywhere especially on membrane.

Therefore as a final way, we tried to remove it during BHF process. After BHF and rinsing sample with DI water we put it in acetone to remove photoresist and as a routine put it in methanol and thus to make ready to dry it with CPD.

Nevertheless, after CPD, there was black area or circular around some samples that demonstrated during the CPD, samples have burned (Figure 4.18).

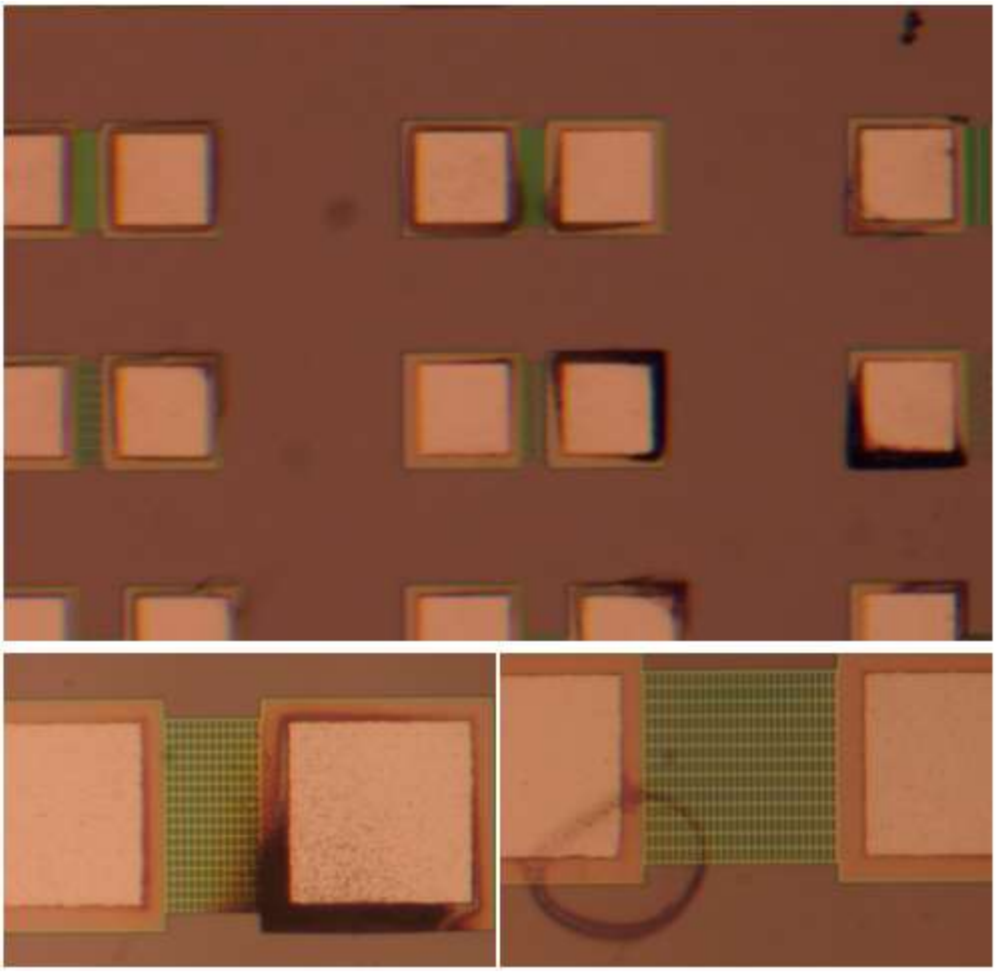

Figure 4.18: Burned area on surface.

We believe this region's reason is due to the methanol, which is still remain on surface after rinse it with IPA. Because, if we do not use methanol after acetone during the BHF process this event will not be happen. Figure 4.19 shows the final state where methanol not be used.

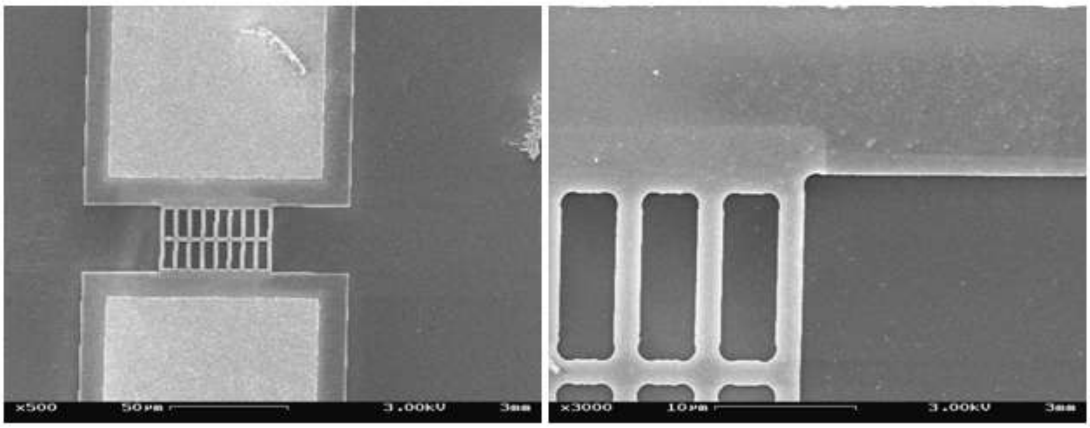

Figure 4.19: Final state with removing photoresist.

4.3. Conclusion Of Fabrication Section

Final state of structures, reveal us that long polysilicon membrane cannot be produced. Because due to the compressive stress which is imposed by phosphorous doping majority of structures are buckled down. Dektak device obtain this result before and after doping phosphorous by measuring curvature of surface and calculating it by below formula (4)

$$\sigma_f = -\frac{1}{6}\frac{E_s}{1-\nu_s}\frac{h_s^{\,2}}{h_f}\left(\frac{1}{R}-\frac{1}{R_o}\right)$$

Where R_o and R are the curvature radius of the substrate before and after deposition of the film, respectively.

By putting achieved results of Dektak in formula for polysilicon, stress has a negative value that means compressive stress. The vibration frequency of the beam as well as decreases with the compressive stress up to the vibration frequency becomes zero. Hence, the beam buckles as it is shown in Figure 4.20.

However, in silicon, calculated stress is positive and it means we have tensile stress and natural frequency will be shifted upper frequency up to buckling again in contrary direction.

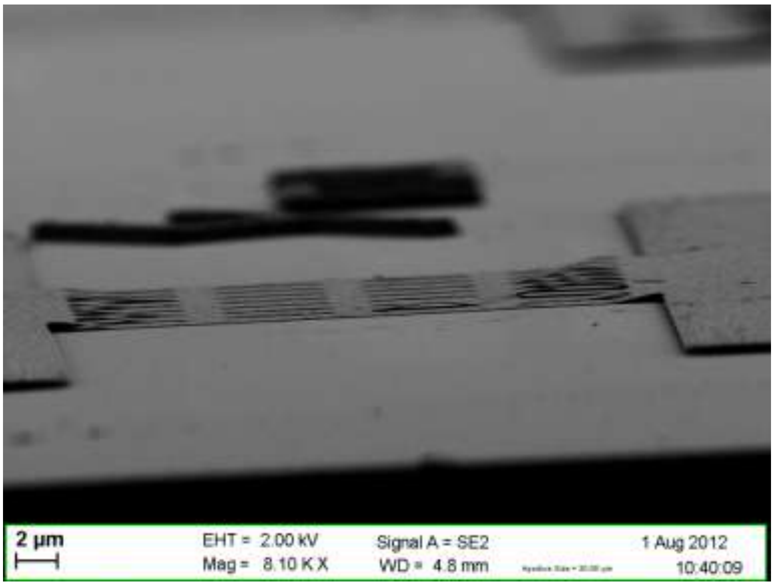

Figure 4.20: Buckling of polysilicon after HF release.

5. SIMULATION

In this section, we performed several simulations with Comsol on based of Finite Element Method (FEM) to obtain modal frequencies at various states as follow:

- Without any thermal or material stress and damping
- With interfering resultant stresses which have been produced by thermal expansion and material property under ambient and vacuum pressure.

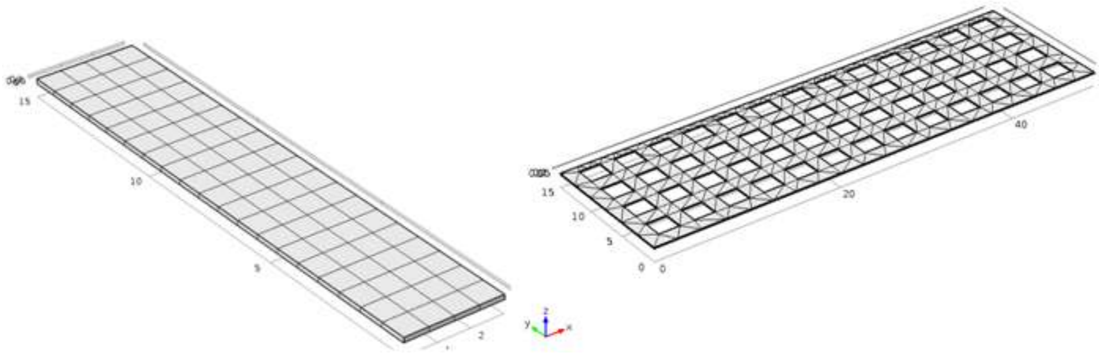

Figure 5. 1: For beams, mapped meshing is used and for membrane with perforation triangular is preferred.

5.1. Resonance Frequency:

Generally, each beam or membrane, due to the shape of design has a natural mechanical frequency at infinite modal frequency. Mainly, common frequency that is

Used at resonant sensor is first mode, where the majority of dissipation of energy and vibrating with large amplitude take place. In addition, first mode frequency is calculated by Eq. (3.5), but as it is seen from the formula the effect of the width of the beam and dimension of holes inside the membrane did not take into account. Therefore, by using Comsol we try to show these differences at identical length of the membrane and compare them with each other.

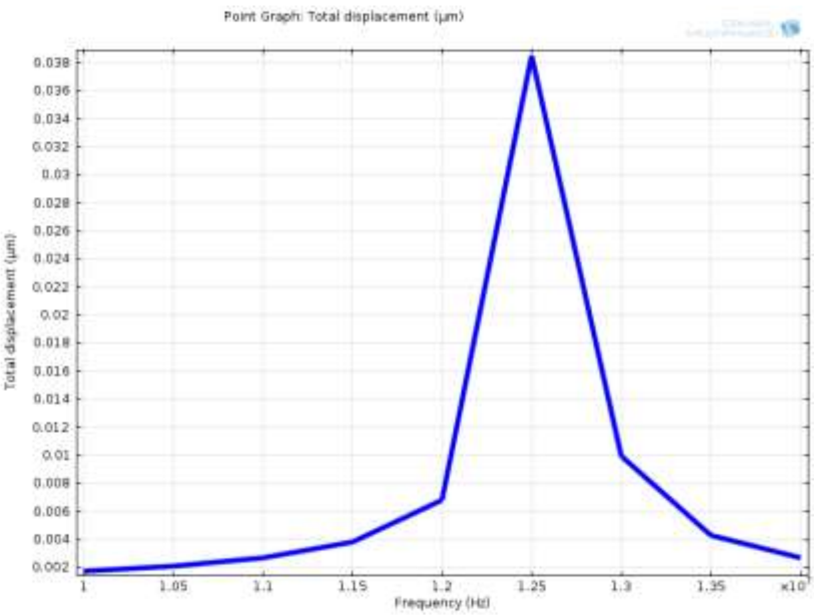

Figure 5. 2: First mode frequency where maximum displacement happen.

5.1.1. First mode resonant frequency of samples:

We designed five types of samples in terms of beam's length. For each length, there are five or six types of membrane's width with various perforation dimensions.

We simulate several of them to observe the effect of the perforation and width of the structures at natural frequency. At below table the changing of the natural frequency on base of the beam's length with identical width have been tabulated. As we expected with increasing length, natural frequency of the beam is reduced, as well as other parameter that affect extremely on natural frequency is thickness, which is fixed in all of the simulation at 140nm.

Table 5. 1: Natural frequency shifting with length of beam

Length of Beam [μm]	**Width of Beam [μm]**	**Thickness [nm]**	**First mode Frequency [Hz]**
10	3	140	1.26E+07
20	3	140	3.14E+06
30	3	140	1.39E+06
50	3	140	4.99E+05
100	3	140	1.24E+05

As it observed from above table, the length of the beam compels major shifting at natural frequency, while the widths of the structures with identical length did not any effect on natural frequency shifting of course with identical perforated dimension.

Table5.2 demonstrates this fact obviously with the approximate same hole's dimension. Numbers of holes at row declare how many holes present at row that in fact it shows number of column in membrane. For instance, "Number of holes" 13, 8 at third row pronounces, in membrane with length 30μm and width 50μm there are 8 and 13 Column and Row respectively (Figure 5.3).

The dimension of hole, which is for example 2.062 × 2, defines the side length of rectangle at length, and width direction of membrane respectively.

Table 5. 2: Not changing natural frequency with varying of beam's width at fixed length and similar perforated dimension.

Length of Beam [μm]	Width of Beam [μm]	Number		Dimension of a hole [μm]	First mode Frequency [Hz]
		Row	Column		
30	5	1	8	2.062 × 2	1.35E+06
30	30	8	8	2.062 × 2.062	1.37E+06
30	50	13	8	2.062 × 2.231	1.36E+06
30	100	28	8	2.062 × 2.018	1.37E+06
50	30	8	8	4.562 × 2.062	4.92E+05
50	100	28	8	4.562 × 2.018	4.91E+05
100	30	8	28	2.018 × 2.062	1.19E+05
100	100	28	28	2.018 × 2.018	1.18E+05

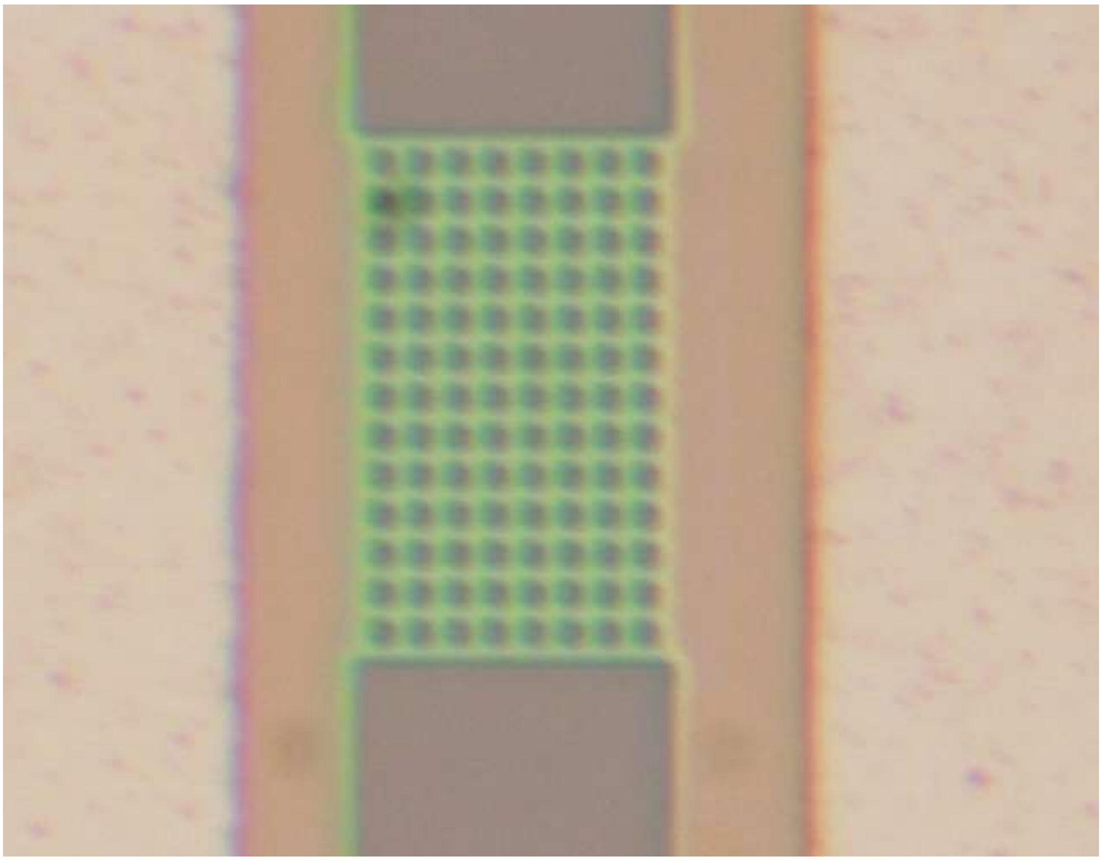

Figure 5. 3: Membrane with length 30μm and width 50μm and 8 and 13 Column and Row respectively.

Until here, all of the results were predictable somehow with analytical formula. However, effect of the hole's dimension in membrane has not been investigated. These holes is necessary in membrane because for etching thermal oxidation and reducing squeeze film damping to get higher quality factor value. At below table as it is observed there are some examples, which show, there is a direct proportional between increasing natural frequencies with increasing hole's side at longitude direction of membrane.

Table5. 3: effect of hole's dimension at natural frequency

Length of Beam [μm]	Width of Beam [μm]	Number of		Dimension of a hole[μm]	First mode Frequency[Hz]
		Row	Column		
100	50	4	28	2.018 × 10.625	8.47E+04
100	50	4	18	3.972 × 10.625	9.16E+04
100	50	4	8	10.813 × 10.625	1.06E+05
100	100	28	28	2.018 × 2.018	1.18E+05
100	100	28	18	3.972 × 2.018	1.21E+05
100	100	28	8	10.813 × 2.018	1.26E+05

The first three rows demonstrate membranes, which are similar to each other only by differences regarding hole’s size at longitude direction of beam and each membrane has 4 rows and 28, 18, 8 columns which are presented two of them at Figure 5.4. As it seen with increasing hole’s side at longitude of membrane, natural frequency is increasing, too. This rule is reliable in all structures with identical size of resonant beam or membrane.

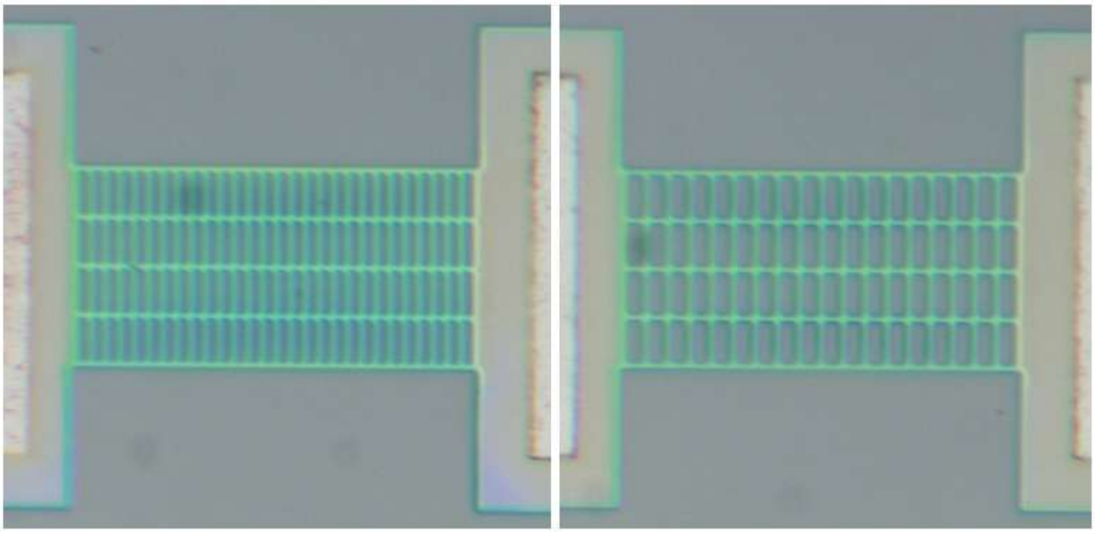

Figure 5. 4: The first two row sample’s structure from table 5.3.

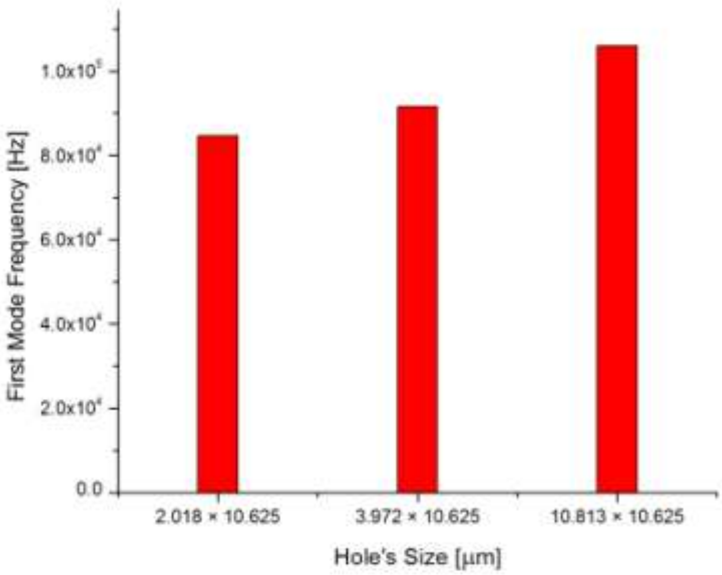

Figure 5. 5: Different hole's size for 100µm length × 50µm width membrane.

Contrarily, with increasing hole's size at width direction of membrane first mode frequency of structures descend. At table5.4, there are some samples from different membrane size.

Table5. 4: effect of the hole's size at natural frequency

Length of Beam [μm]	Width of Beam [μm]	Number of		Dimension of a hole[μm]	First mode Frequency[Hz]
		Row	Column		
30	100	28	8	2.062 × 2.018	1.37E+06
30	100	18	8	2.062 × 3.972	1.25E+06
30	100	8	8	2.062 × 10.813	9.41E+05
30	100	3	8	2.062 × 31.334	5.58E+05
50	100	28	8	4.562 × 2.018	4.91E+05
50	100	18	8	4.562 × 3.972	4.58E+05
50	100	8	8	4.562 × 10.813	3.67E+05

Figure5.6 schematically illustrates this concept for first four rows from table5.4 where length and width of the structures are 30, and 100 μm respectively.

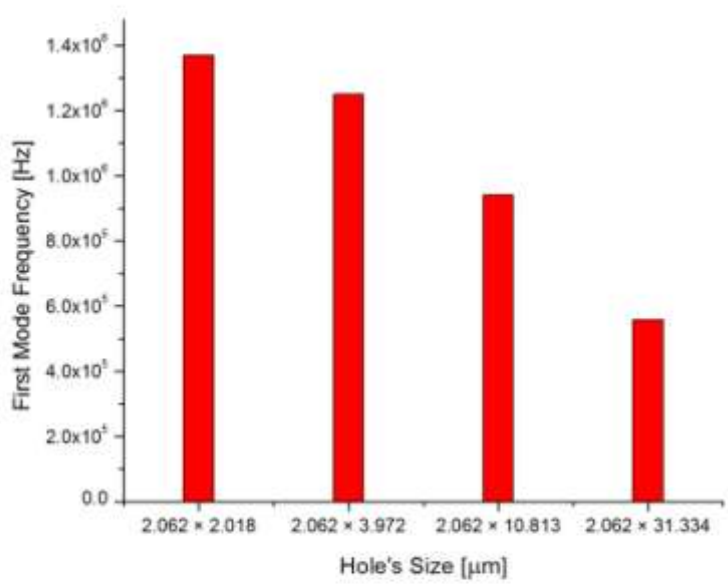

Figure 5. 6: Different hole's size for 30μm length × 100μm width membrane.

5.1.2. First mode frequency shifting with initial stress:

In the Fabrication section, initial stress, which has been produced due to the doping Phosphorous, was calculated. With putting this value at 'initial stress and strain' part of Comsol, first mode natural frequency is shifted. Because of the positive value of the stress, it declares that stress is tensile, natural frequency is moved to higher frequency. Table5.5 shows this fact perceptibly.

Table 5. 5: shifting first natural frequency by take into account of initial stress.

Length of Beam [μm]	Width of Beam [μm]	First mode Frequency with initial stress [Hz]	First mode Frequency without initial stress [Hz]
10	3	1.60E+07	1.26E+07
20	3	5.79E+06	3.14E+06
30	3	3.48E+06	1.39E+06
50	3	1.94E+06	4.99E+05
100	3	9.26E+05	1.24E+05

5.2. Eigenfrequency in Comsol

In working with Comsol, Eigenfrequency is used for studying frequency behavior subject to some parameters like stress, and damping. For example with increasing stress value more or negative (compressive stress), for Silicon Eigenfrequency will appear completely as imaginary value which means, membrane is buckled and it is irreversible.

As it was described in previous section with calculated initial stress, natural frequency was shifted higher frequency without of changing to imaginary part. However, commonly imaginary part is produced by damping. During the simulation two effective damping which are playing dominant role at ambient and vacuum pressure, were taken into account. At ambient pressure air damping is predominant and at vacuum, material losses.From the eigenfrequency value, we are able to calculate quality factor. As we know eigenfrequency subject to damping, has imaginary part. Therefore, if we assume Gamma is the real part and Sigma is the imaginary part, the first frequency of the structures will oscillate:

$$f_{damp} = \sqrt{\gamma^2 - \sigma^2}$$

In addition, we can compute quality factor of structures by:

$$\omega_{damp} = \omega_{ideal} \sqrt{1 - \frac{1}{2Q}}$$

Where ω_{ideal} is undamped frequency.

The dimension of the structures and hole's size also affect significantly quality factor of samples which will discuss it in continue.

5.3. Quality Factor

In general, most of the clamped-clamped resonators because of the lower quality factor at ambient pressure, they are measured at vacuum condition.

Also from the simulation results quality factor of them are explicit in Figure5.7 for samples which were shown in table5.5

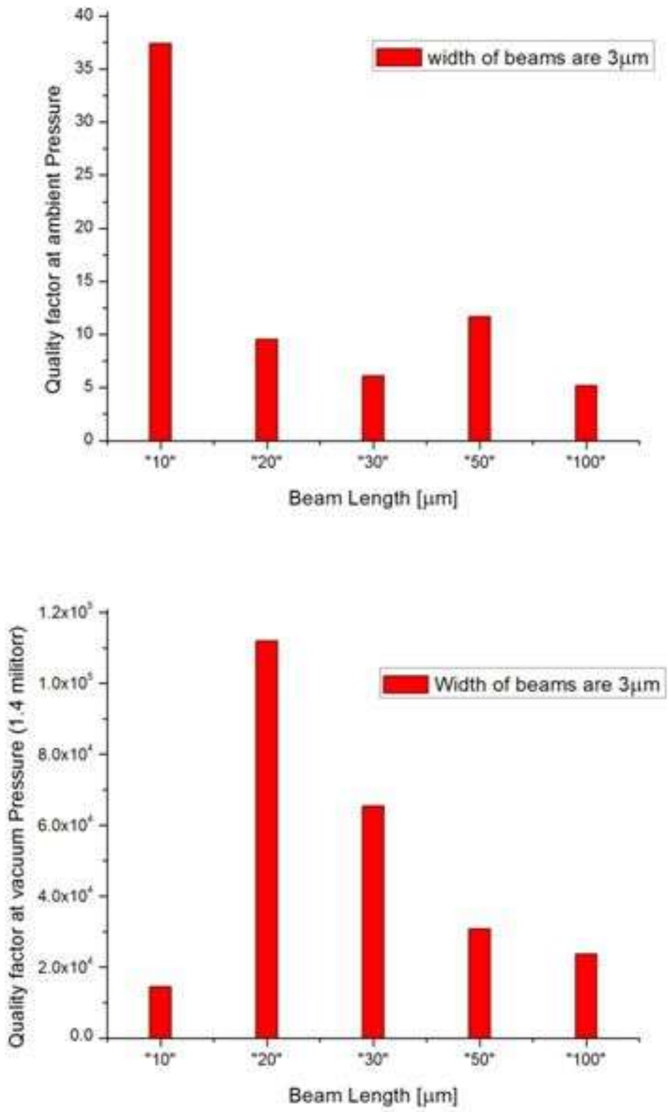

Figure 5. 7: Quality factor differences for the same samples with two type of the pressure.

Now as influence of the holes size on changing quality factor value from simulation, we can observe that commonly quality factor of the samples with identical dimension, those have higher natural frequency as well as have higher quality factor at ambient and vacuum pressure, too. For instance, table5.6 demonstrates this fact very well.

Table 5. 6: behavior of hole's size with quality factor

Length of Beam [μm]	Width of Beam [μm]	Number of		First Mode Frequency[Hz]	Quality factor at Ambient	Quality factor at Vacuum
		Row	Column			
20	20	5	4	5.51E+06	2.53E+01	8.20E+04
20	20	2	4	4.25E+06	2.42E+01	7.81E+03
20	50	13	4	5.80E+06	2.75E+01	8.17E+04
20	50	6	4	4.77E+06	2.71E+01	9.40E+03
30	10	2	8	3.03E+06	1.30E+01	1.35E+04
30	10	2	2	3.42E+06	1.66E+01	9.76E+04
30	100	28	2	3.58E+06	1.81E+01	2.28E+06
30	100	8	2	2.88E+06	2.07E+01	9.74E+04
50	50	13	8	1.82E+06	7.22E+00	1.37E+04
50	50	8	8	1.63E+06	6.66E+00	7.81E+03
100	10	2	18	8.34E+05	3.98E+00	1.12E+04
100	10	2	8	8.83E+05	4.47E+00	1.62E+04
100	50	4	28	5.27E+05	2.32E+00	1.33E+03
100	50	4	8	7.24E+05	3.65E+00	2.04E+03

Every sample with fixed length has been distinguished by same color. Previously the role of the hole's dimension was discussed about the changing of natural frequency, and as it seen with increasing width of membrane and producing more or it is better to say maximum numbers of rows and minimum numbers of columns for perforated membrane we reached max quality factor at vacuum condition.

5.4. Joule Heating and Thermal Expansion

During the measuring of the resistance, we faced with collapsing membranes particularly at longest ones (100µm) when contact area is touched by measuring needles. Therefore, for estimating the max value of current that we are able to apply to structures is calculated by joule heating and thermal expansion function in Comsol.

For instance by applying various current density to membrane, the results in stress and changing temperature is achieved. Furthermore, with knowing fractural or failure strength and melting point of silicon, it will be predictable to get an idea about the amount of current flow for each sensor.

We assume that the design failure stress should be the fracture strength of silicon. The fracture strength of silicon is given by Petersen as being 7000 MPa. This extremely high failure stress is contradicted by experience with under etched membranes where failures stresses are estimated to be in the order of 300 MPa.

In addition, from physical properties of silicon we know that melting point is around 1700˚K. Hence, if the outcomes of simulation to reach more than this value then we can say, the respective sample has been fractured or melted.

Table5.7 demonstrates changing von Mises stress and produced temperature of silicon beams with current flow at five simple beams with identical 3µm width.

As it is observed in all results, beams reach the failures stress (Green area) before melting point (Blue area) of silicon. Hence, during the investigation of other structures, failure stress will be taken into account. Moreover, we should not have any concern about which failure stress is reliable to us, 7000 MPa or 300 MPa?! Because, after increasing current - several milli ampere in shorter beams and tenth milli ampere in longer ones - they reach to melting point of the silicon.

As it is observed from simulation results, for the shorter beams endurance of loading current is higher than longer beams. For instance for 10µm length beam, 12.2mA is the supreme value of current and for 100µm length beam, 1.4mA.

In continue we simulate thermal expansion for same samples, which previously did it at resonant frequency section to be able easier comparison with them, too.

Table 5. 7: Behavior of five types beam with identical width versus various current flows to demonstrate critical fractural strength and temperature.

3µm width of beam														
1_1			2_17			8_11			18_14			22_9		
10µm length			20µm length			30µm length			50µm length			100µm length		
Current [mA]	von Mises stress [N/m^2]	Temperature [K]	Current [mA]	von Mises stress [N/m^2]	Temperature [K]	Current [mA]	von Mises stress [N/m^2]	Temperature [K]	Current [mA]	von Mises stress [N/m^2]	Temperature [K]	Current [mA]	von Mises stress [N/m^2]	Temperature [K]
1	1.45E+06	296.2065688	1	4.10E+06	305.455017	0.6	3.19E+06	303.1285714	0.4	3.89E+06	305.4534565	0.1	9.65E+05	296.2047535
2	5.83E+06	305.4552399	2	1.68E+07	343.6743018	0.7	4.36E+06	306.7937549	0.5	6.11E+06	312.4676865	0.2	3.88E+06	305.4478866
3	1.32E+07	321.1379372	3	3.94E+07	412.0729978	0.8	5.66E+06	310.8604841	0.6	8.87E+06	321.2138194	0.3	8.83E+06	321.1210393
4	2.39E+07	343.6752403	4	7.46E+07	519.1236272	0.9	7.21E+06	315.6923051	0.7	1.22E+07	331.6995616	0.4	1.59E+07	343.6442865
5	3.80E+07	373.6946816	5	1.27E+08	680.3924947	1	8.95E+06	321.1365709	0.8	1.59E+07	343.4482432	0.5	2.54E+07	373.644385
6	5.62E+07	412.4363928	6	2.07E+08	927.7297508	2	3.79E+07	412.0691542	0.9	2.03E+07	357.5657359	0.6	3.75E+07	412.3600872
7	7.89E+07	460.9106076	6.1	2.15E+08	953.7400442	3	9.48E+07	591.5815445	1	2.54E+07	373.6824828	0.7	5.27E+07	460.8001023
8	1.05E+08	518.0314935	6.2	2.29E+08	994.6993569	4	2.00E+08	925.1564737	2	1.21E+08	680.3313076	0.8	7.06E+07	517.8783302
9	1.39E+08	590.9264782	6.3	2.38E+08	1023.381231	4.1	2.15E+08	972.5262406	2.1	1.38E+08	732.5334056	0.9	9.33E+07	590.7151814
10	1.81E+08	680.4012371	6.4	2.47E+08	1053.232744	4.2	2.30E+08	1023.348838	2.2	1.56E+08	790.5817064	1	1.21E+08	680.1129357
11	2.31E+08	790.6767302	6.5	2.62E+08	1100.344965	4.3	2.45E+08	1068.58192	2.3	1.75E+08	852.443448	1.1	1.55E+08	789.2661936
12	2.94E+08	927.7459279	6.6	2.73E+08	1133.412563	4.4	2.67E+08	1141.858109	2.4	1.97E+08	924.4357168	1.2	1.97E+08	924.6687228
12.2	3.06E+08	953.7570864	6.7	2.84E+08	1167.897265	4.5	2.84E+08	1194.697845	2.5	2.22E+08	1005.190271	1.3	2.49E+08	1094.797658
12.4	3.21E+08	987.7227449	6.8	3.01E+08	1222.466319	4.6	3.02E+08	1251.06702	2.6	2.50E+08	1096.152808	1.4	3.16E+08	1312.447498
12.6	3.37E+08	1023.400667	6.9	3.14E+08	1260.875118	4.7	3.30E+08	1342.975396	2.7	2.82E+08	1199.11759	1.5	4.04E+08	1597.829083
12.8	3.54E+08	1060.906576	7	3.33E+08	1321.788137	4.8	3.51E+08	1409.715872	2.8	3.16E+08	1311.13432	1.6	5.22E+08	1984.794984
13	3.68E+08	1092.312199	7.1	3.47E+08	1364.762088	4.9	3.85E+08	1519.168016	2.9	3.57E+08	1444.697855	1.7	6.90E+08	2534.612064
14	4.67E+08	1311.378582	7.2	3.61E+08	1409.773829	5	4.10E+08	1599.149145	3	4.04E+08	1598.91686	1.8	9.44E+08	3370.655187
15	5.96E+08	1599.265319	7.3	3.84E+08	1481.416663	5.1	4.37E+08	1685.475783	3.1	4.59E+08	1778.608341	1.9	1.37E+09	4783.662699
15.2	6.28E+08	1670.742863	7.4	4.00E+08	1532.153118	5.2	4.81E+08	1828.517518	3.2	5.24E+08	1990.228864	2	2.24E+09	7660.832913
15.4	6.62E+08	1747.049497	7.5	4.25E+08	1613.151321	5.3	5.14E+08	1934.222485	3.3	5.98E+08	2231.156943			
15.6	6.91E+08	1811.892058	7.6	4.43E+08	1670.695763	5.4	5.68E+08	2111.03853	3.4	6.90E+08	2534.30005			
15.8	7.30E+08	1898.1443	7.7	4.63E+08	1731.329506	5.5	6.09E+08	2243.059973						
16	7.71E+08	1990.743699	7.8	4.93E+08	1828.609722	5.6	6.54E+08	2388.31977						
17	1.02E+09	2549.113168	7.9	5.15E+08	1898.085172	5.7	7.30E+08	2635.584371						
18	1.37E+09	3358.491103	8	5.38E+08	1971.62075	5.8	7.88E+08	2823.803306						
19	2.00E+09	4778.138426	9	9.72E+08	3358.326198	5.9	8.53E+08	3034.558292						
20	3.27E+09	7686.079002	10	2.31E+09	7685.311449	6	9.67E+08	3402.450771						

At table5.8 as we expected in wider beams with the same length because of the scattering heating in whole structures and consequently convective cooling, the supreme applying current become higher.

Table 5. 8: Compare different sensor's maximum applicable current with same hole's dimension.

Length of beam[μm]	Width of beam[μm]	Number of		Dimension of a hole[μm]	Von Mises Stress [N/m^2]	Current [mA]
		Row	Column			
30	5	1	8	2.062 × 2	3.07E+08	4.7
30	30	8	8	2.062 × 2.062	3.08E+08	6.5
30	50	13	8	2.062 × 2.231	3.06E+08	27
30	100	28	8	2.062 × 2.018	3.03E+08	53
50	30	8	8	4.562 × 2.062	3.10E+08	11.6
50	100	28	8	4.562 × 2.018	3.02E+08	31.8
100	30	8	28	2.018 × 2.062	3.02E+08	6.2
100	100	28	28	2.018 × 2.018	3.04E+08	14.8

Table5.9 and 5.10 demonstrate samples with identical length and width that only differences between them is perforation's size inside membrane.

Table 5. 9: 100μm Length-100μm Width membrane

Number of		Dimension of a hole[μm]	Von Mises Stress [N/m^2]	Current [mA]
Row	Column			
28	28	2.018 × 2.018	3.14E+8	15
28	18	3.972 × 2.018	3.07E+8	16.5
28	8	10.813 × 2.018	3.08E+8	17.2

Table 5. 10: 50μm Length-100μm Width membrane

Number of		Dimension of a hole[μm]	Von Mises Stress [N/m^2]	Current [mA]
Row	Column			
28	8	4.562 × 2.018	3.15E+8	32
18	8	4.562 × 3.972	3.16E+8	22
8	8	4.562 × 10.813	3.16E+8	10.8

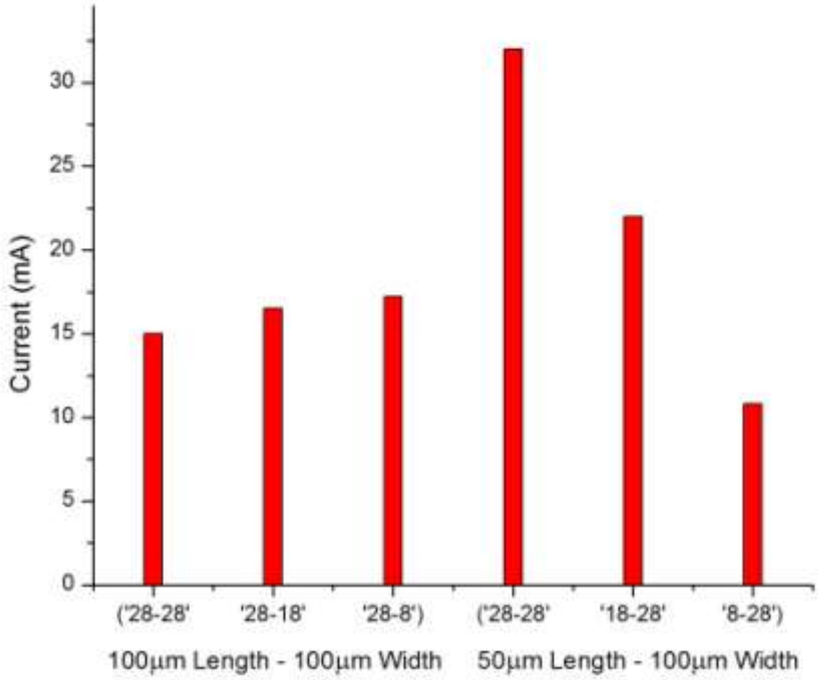

Figure 5. 8: Maximum current for each sample.

As their related diagrams illustrate, same as behavior that we saw in resonant frequency section is observed here for current. The endurance of structures regarding current flow rise and fall with increasing hole's side in length and width direction of beam respectively.

After knowing each sample's maximum applicable current we can find now maximum deflection of every ones while we do not face with destroying them.

5.5. Displacement

During the previous subsection, we obtained maximum applicable current for each structure. Hence, with placing them at defined magnetic field Lorentz force is achieved by right hand rule. Therefore, by applying force to central edge of each sensor (Figure5.9), we can observe that how much deflection will be acquired.

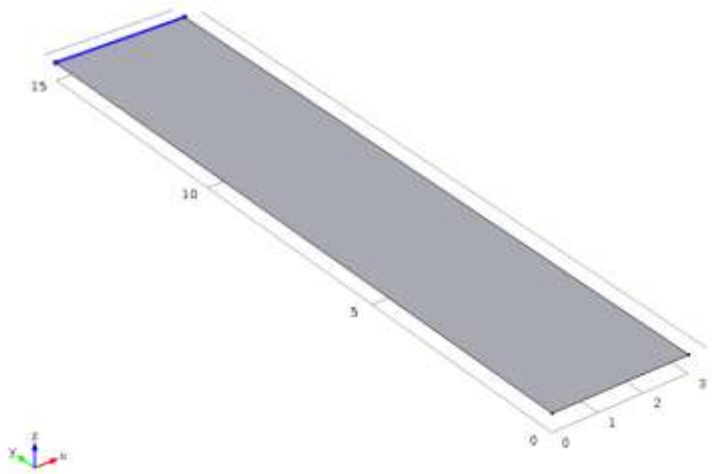

Figure 5. 9: Apply force to half symmetry edge (It has defined by blue line).

As we expected for the longer beams, deflections are more that shorter ones subject to the same amount of force. Figure 5.10 illustrate it for sensors with five different length beams with identical 3µm width regarding to the 3.00E-5 F/m.

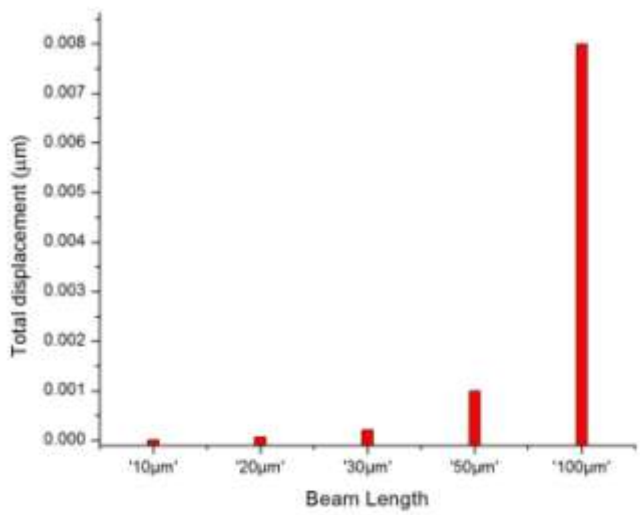

Figure 5.10: Displacement of 5 type of the structures by static force.

Consequently, we applied these types of static force for perforated membranes and we observed that changing hole's side in both directions of the structures, deflection is not differed subject to them. In this situation, maximum deflection is happen to structures, which have less mass.

Figure5.11 illustrates the displacement of the structures, which have been defined at table5.11.

Table 5. 11: 100µm Length-100µm Width membrane

Number of		Dimension of a hole[µm]	Force per meter [F/m]	Displacement [µm]	Mass [Kg]
Row	Column				
28	28	2.018 × 2.018	7.5E-7	0.0036	2.22E-12
28	18	3.972 × 2.018	7.5E-7	0.004	1.94E-12
28	8	10.813 × 2.018	7.5E-7	0.0043	1.67E-12

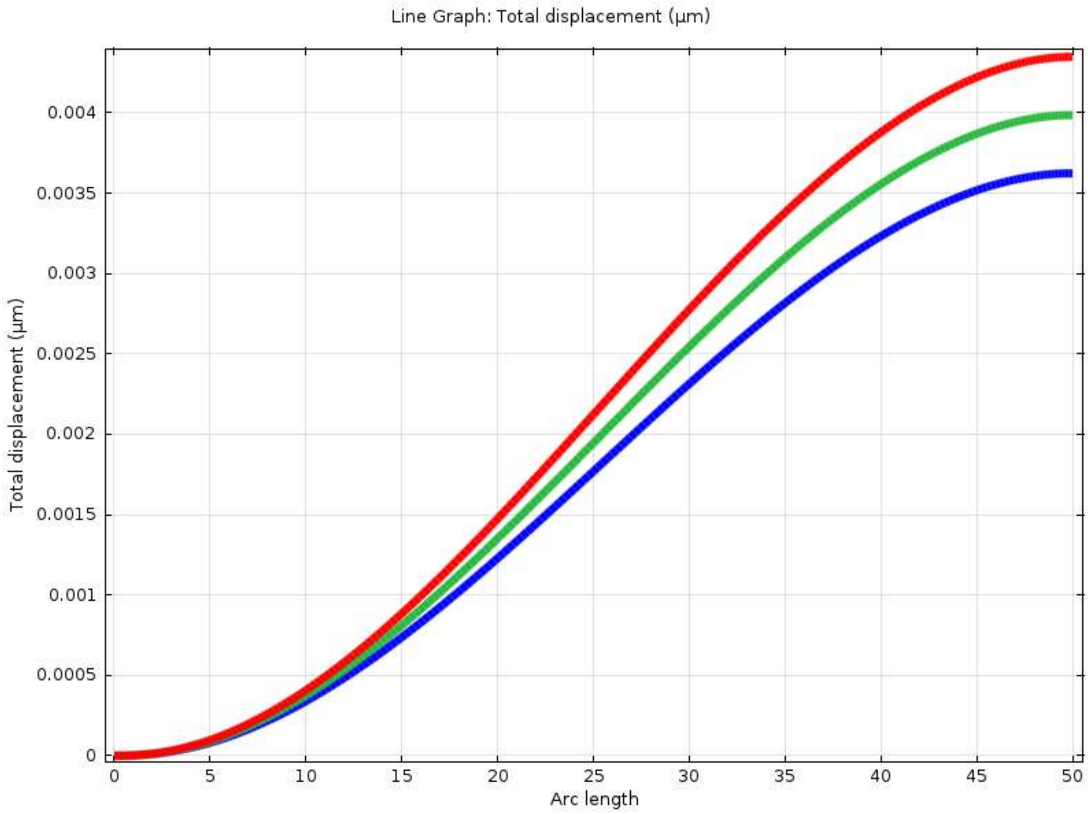

Figure 5.11: Displacement of three structures with different perforation size at identical condition.

As it seen from diagram at the same current (10mA) that means under same force, displacement of structures are relate to their mass. Membrane by lower mass has higher displacement regarding to fixed current.

Until here, all of the displacements were due to the static force on sensors. However, during the measurement AC current is applied. Then, in Comsol this behavior is simulated by dynamic force around natural frequency, but as we know without of the any damping factor, displacement will go to infinity. Hereby, in simulation we assume that these trials are taken happen into vacuum situation, so only material damping is taken into account.

For instance, figure5.12 exhibit dynamic force for above table.

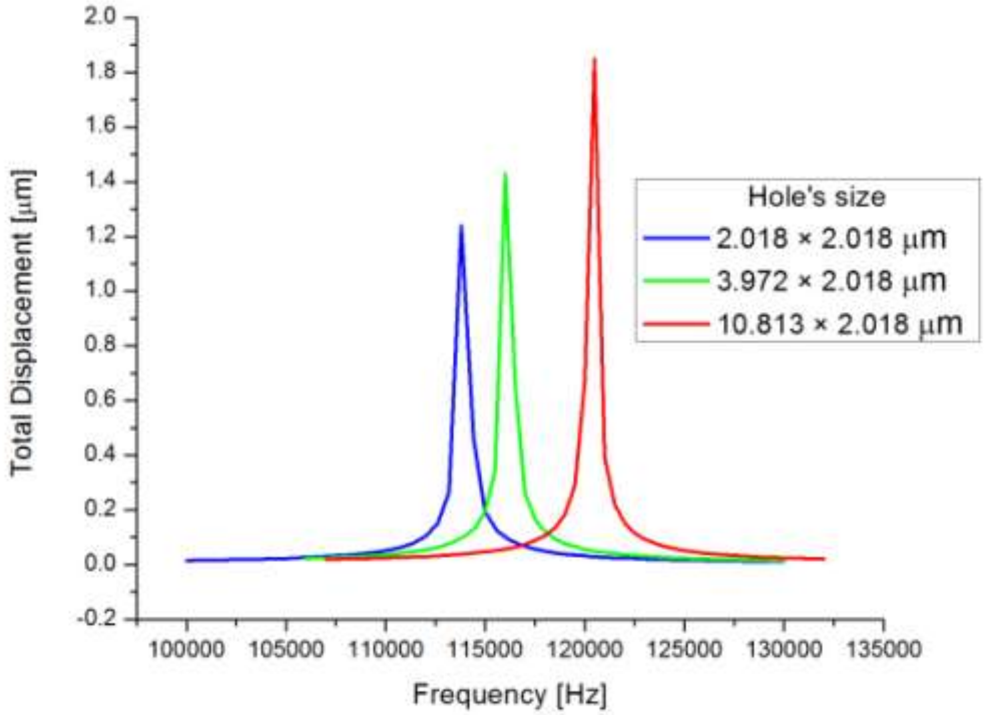

Figure 5.12: Dynamic displacement of three identical sensors with only different perforated membrane.

6. EXPERIMENTAL MEASUREMENT

Polytec MSA-500 is the device, which is used for the characterization of MEMS microstructures.

In addition to the white light interferometry to determine the topography of a structure, Polytec offers laser vibrometry based on the Doppler effect to measure a moving velocity off-plane at high resolution. Integrating these data at different points of the structure allows evaluating the movement. The measurement is performed with two lasers. The first scans the surface at several points and measures the speed of travel. The second laser called "Reference Beam", fixed point of the structure, which serves as a reference and thus allows a differential measurement of the displacement.

The measurement is synchronized with an excitation signal according to the selected measurement type:

- For spectrum measurement, the excitation signal is a signal used "periodic chirp" to excite all frequencies of the spectrum simultaneously with identical amplitude for all frequencies. Polytec generates the phases between the different signals by means of an algorithm that maximizes the energy to maximum amplitude given

- For displacement measurement, the excitation signal is a signal used "sine" to measure the deflection profile at a particular frequency and offers a very good signal to noise ratio.

We must also take into account the time that the Polytec must "wait" between the beginning of the excitement and the first measurement. This setting is controlled by the option Polytec Steady-State and to measure the device in its optimal state after the transition period following the excitation.

We did this measurement for more than half sensors, and unfortunately except four of them did not show us any sensible and proper displacement by Polytec. Especially for the shorter beams, we did not get any observable result even at vacuum condition.

However, as we mentioned before for only four samples only in vacuum circumstances, some results obtained that Even, for those four structures, the results are a little bit unreliable. Because, as it is shown in figure6.1 the suggested first mode shape that has derived from frequency diagram is strange as well as maximum deflection did not happen at assumed first frequency. for instance number 7 or 8 should be first mode but from the shape of the displacement which has been illustrated at figure6.2 number 3 or 4 are more similar to first mode than others.

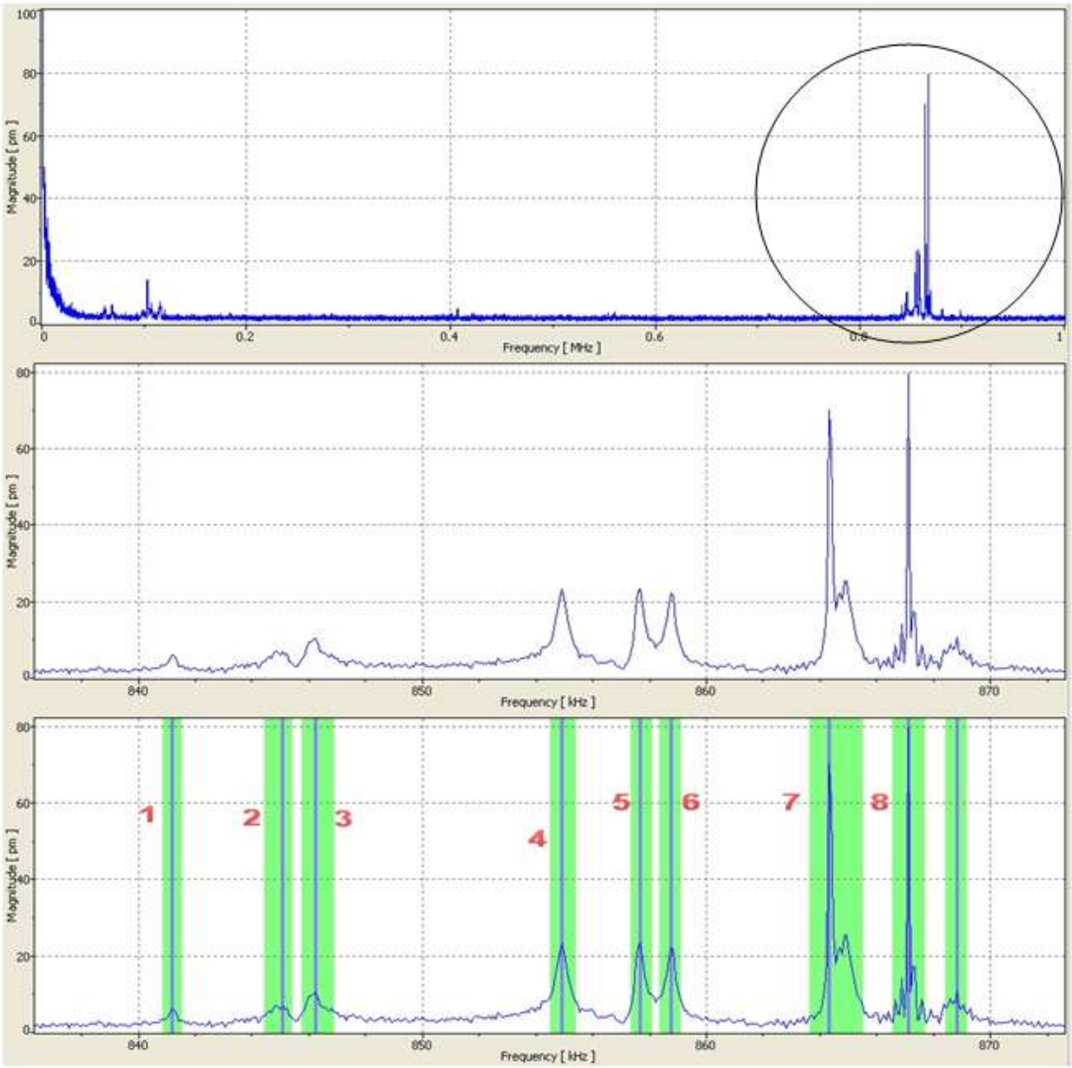

Figure 6. 1: Apply periodic chirp to resonator to find first mode.

It is mentionable that, for measuring displacement of membranes into vacuum condition, we did not apply any current to contact area of sensors or using any magnet to produce magnetic field, but the piece of sample attached to the piezoceramic. By applying any signals i.e. periodic chirp, each membrane should have highest displacement at its natural frequency.

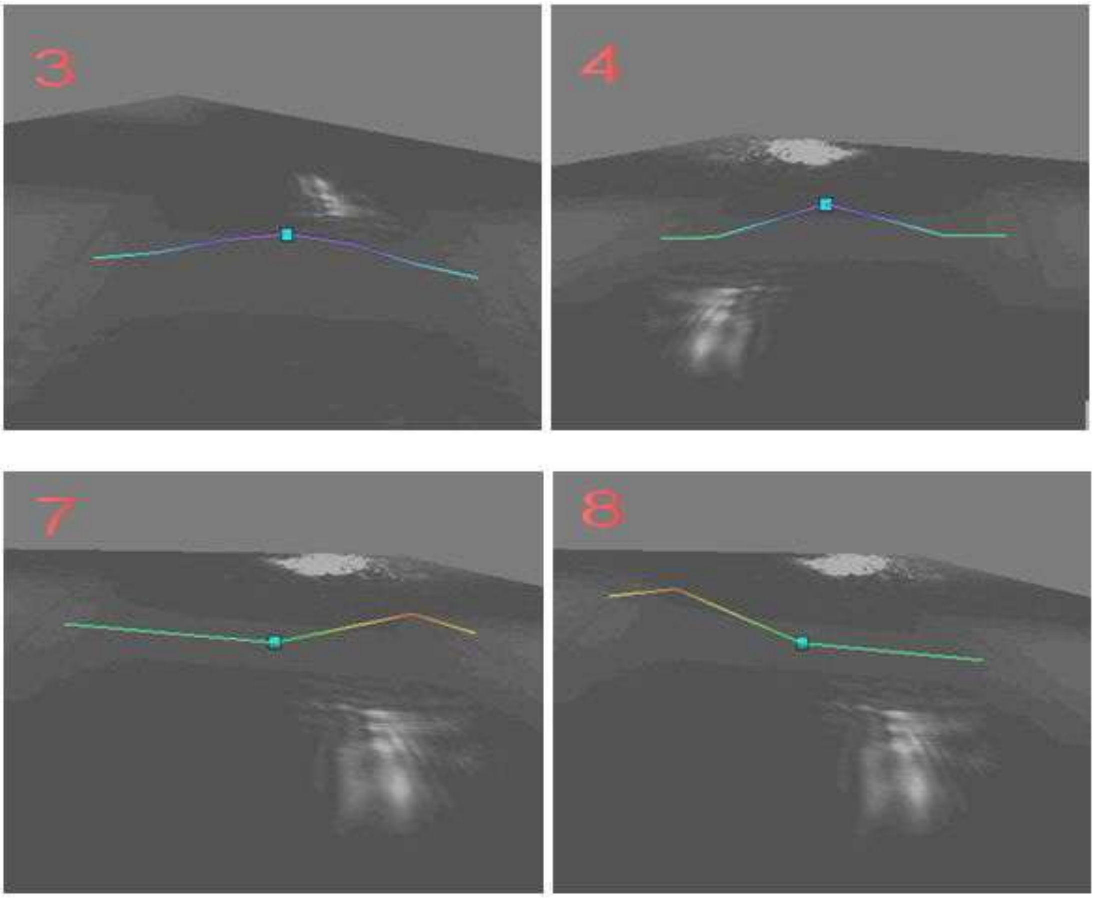

Figure 6. 2: Displacement shape regarding the frequencies which have defined at previous figure.

On base of 3 or 4 as first mode natural frequency, even we applied sinusoidal input at defined frequency, maximum deflection as a dynamic displacement are 2.390nm and 3.706nm respectively.

7. CONCLUSION & RECOMMENDATION

In this paper, several MEMS clamped-clamped magnetic sensors have been designed by Cadence, and have been fabricated on base of SOI Wafer and polysilicon deposition on silicon bulk and have been simulated them by Comsol and Coventorware softwares.

In Designing sector at first for polysilicon-based resonator, two light masks by names of POLY and METAL-PAD were designed, and in continue for SOI wafer based resonator another dark mask (CAVITY) was proposed, too.

During the fabrication process especially at releasing sacrificial layer (final part), several alternative methods have been tested. At first, we tried to implement it by polysilicon as actuated beams, which faced with stick problem to substrate before vibration. Therefore, we started to carry it out on SOI wafer.

These sensors before experiment them in measurement laboratory, were investigated by Comsol and Coventorware simulation softwares. Form these softwares particularly Comsol some information such as probable natural frequency, maximum applicable current, effect of hole's dimension on them and their displacement has been achieved.

In simulation section at first, natural frequency of various resonators considering width, length, and perforation of membranes were simulated. Even, effect of hole's side in both direction of length and width were explored.

The quality factor of sensors were calculated in two condition: 1.Ambient Pressure 2.Vacuum pressure (1.4mtorr). the two damping or it is better to say energy dissipation system were taken into account at calculation quality factor: a) material losses, and b) air damping.

In addition, for actuation of resonators as we know current is needed, but excessive current bring about high stress that lead to collapsing membrane. Hence, by simulation generated stress which is acquired by current, the maximum applicable current was estimated for each sensor.

Finally, some measurement was carried out on some structures. If we compare the simulated results with the experimental outcomes, we noticed huge differences; approximately one thousand magnitudes. Thus, the experimental work should be carried out again for the future job, with more accuracy and of course new method in my opinion.

REFERENCES

1. **Bahreyni B, Shafai C**. A Resonant Micromachined Magnetic Field Sensor. *IEEE Sensors Journal* 7: 1326–1334, 2007.

2. **Bao M, Wang W**. Future of microelectromechanical systems (MEMS). *Sensors and Actuators A: Physical* 56: 135–141, 1996.

3. **Beroulle V, Bertrand Y, Latorre L, Nouet P**. Monolithic piezoresistive CMOS magnetic field sensors. *Sensors and Actuators A: Physical* 103: 23–32, 2003.

4. **Boé A, Safi A, Coulombier M, Pardoen T, Raskin J-P**. Internal stress relaxation based method for elastic stiffness characterization of very thin films. *Thin Solid Films* 518: 260–264, 2009.

5. **Dario P, Carrozza MC, Benvenuto A, Menciassi A**. Micro-systems in biomedical applications. *Journal of Micromechanics and Microengineering* 10: 235–244, 2000.

6. **Emmerich H, Schofthaler M**. Magnetic field measurements with a novel surface micromachined magnetic-field sensor. *IEEE Transactions on Electron Devices* 47: 972–977, 2000.

7. **Franssila S**. *Introduction to Microfabrication*. 1st ed. Wiley, 2004.

8. **Herrera-May AL, Aguilera-Cortés LA, García-Gonzalez L, Figueras-Costa E**. Mechanical behavior of a novel resonant microstructure for magnetic applications considering the squeeze-film damping. *Microsystem Technologies* 15: 259–268, 2008.

9. **Herrera-May AL, García-Ramírez PJ, Aguilera-Cortés LA, Martínez-Castillo J, Sauceda-Carvajal A, García-González L, Figueras-Costa E**. A resonant magnetic field microsensor with high quality factor at atmospheric pressure. *Journal of Micromechanics and Microengineering* 19: 015016, 2009.

10. **Janusz B**. Impact of MEMS technology on society. *Sensors and Actuators A: Physical* 56: 1–9, 1996.

11. **Jr WW, Timoshenko SP, Young DH**. *Vibration Problems in Engineering*. 5th ed. Wiley-Interscience, 1990.

12. **Kaajakari V**. *Practical MEMS: Design of microsystems, accelerometers, gyroscopes, RF MEMS, optical MEMS, and microfluidic systems*. Small Gear Publishing, 2009.

13. **Kádár Z, Bossche A, Sarro PM, Mollinger JR**. Magnetic-field measurements using an integrated resonant magnetic-field sensor. *Sensor Actuat APhys* 70: 225–232, 1998.

14. **Kang JW, Guckel H, Ahn Y**. Amplitude detecting micromechanical resonating beam magnetometer. In: , *The Eleventh Annual International Workshop on Micro Electro Mechanical Systems, 1998. MEMS 98. Proceedings*. , The Eleventh Annual International Workshop on Micro Electro Mechanical Systems, 1998. MEMS 98. Proceedings. IEEE, 1998, p. 372–377.

15. **Keplinger F, Kvasnica S, Hauser H, Grossinger R**. Optical readouts of cantilever bending designed for high magnetic field application. *IEEE Transactions on Magnetics* 39: 3304– 3306, 2003.

16. **Korvink JG, Paul O**. *MEMS: A Practical Guide to Design, Analysis and Applications*. Noyes Pubn, 2005.

17. **Kotzar G, Freas M, Abel P, Fleischman A, Roy S, Zorman C, Moran JM, Melzak J**. Evaluation of MEMS materials of construction for implantable medical devices. *Biomaterials* 23: 2737–2750, 2002.

18. **Noykov S, Lozanova S, Roumenin C**. Two-axis magnetometer using circular parallel-field Hall microsensor for contactless angle measurement. *Electronics Letters* 46: 1130–1132, 2010.

19. **Palaniapan M, Khine L**. Nonlinear behavior of SOI free-free micromechanical beam resonator. *Sensors and Actuators A: Physical* 142: 203–210, 2008.

20. **Petridis C, Dimitropoulos PD, Hristoforou E**. New Magnetic Field Sensor Based on Combined Flux-Gate/Hall-Effect Arrangement. *IEEE Sensors Journal* 9: 128–134, 2009.

21. **Randall RH, Rose FC, Zener C**. Intercrystalline Thermal Currents as a Source of Internal Friction. *Phys. Rev.* 56: 343–348, 1939.

22. **Randjelovic ZB, Kayal M, Popovic R, Blanchard H**. Highly sensitive Hall magnetic sensor microsystem in CMOS technology. *IEEE Journal of Solid-State Circuits* 37: 151–159, 2002.

23. **Rao SS**. *Mechanical Vibrations*. 4th ed. Prentice Hall, 2003.

24. **Ren D, Wu L, Yan M, Cui M, You Z, Hu M**. Design and Analyses of a MEMS Based Resonant Magnetometer. *Sensors* 9: 6951–6966, 2009.

25. **Srikar VT, Senturia SD**. Thermoelastic damping in fine-grained polysilicon flexural beam resonators. *Journal of Microelectromechanical Systems* 11: 499–504, 2002.

26. **Sunier R, Vancura T, Yue Li, Kirstein K-U, Baltes H, Brand O**. Resonant Magnetic Field Sensor With Frequency Output. *Journal of Microelectromechanical Systems* 15: 1098–1107, 2006.

27. **Tapia JA, Herrera-May AL, García-Ramírez PJ, Martinez-Castillo J, Figueras E, Flores A, Manjarrez E**. Sensing magnetic flux density of artificial neurons with a MEMS device. *Biomed Microdevices* 13: 303–313, 2011.

28. **Thompson MJ, Horsley DA**. Resonant MEMS magnetometer with capacitive read-out. In: *2009 IEEE Sensors*. 2009 IEEE Sensors. IEEE, 2009, p. 992–995.

29. **Tucker J, Wesoleck D, Wickenden D**. An integrated CMOS MEMS xylophone magnetometer with capacitive sense electronics. *2000 NanoTech*. .

30. **Veijola T, Kuisma H, Lahdenperä J, Ryhänen T**. Equivalent-circuit model of the squeezed gas film in a silicon accelerometer. 48: 239–248, 1995.

31. **Wickenden DK, Champion JL, Osiander R, Givens RB, Lamb JL, Miragliotta JA, Oursler DA, Kistenmacher TJ**. Micromachined polysilicon resonating xylophone bar magnetometer. *Acta Astronautica* 52: 421–425, 2003.

32. **Won-Youl Choi, Jun-Sik Hwang, Sang-On Choi**. The microfluxgate magnetic sensor having closed magnetic path. *IEEE Sensors Journal* 4: 768–771, 2004.

33. **Zanetti LJ, Potemra TA, Oursler DA, Lohr DA, Anderson BJ, Givens RB, Wickenden DK, Osiander R, Kistenmacher TJ, Jenkins RE**. Miniature Magnetic Field Sensors Based on Xylophone Resonators. [date unknown].

34. **Zener C**. Internal Friction in Solids. I. Theory of Internal Friction in Reeds. *Phys. Rev.* 52: 230–235, 1937.

35. **Zook JD, Burns DW, Guckel H, Sniegowski JJ, Engelstad RL, Feng Z**. Characteristics of polysilicon resonant microbeams. *Sensors and Actuators A: Physical* 35: 51–59, 1992.

CURRICULUM VITAE

Name Surname: Omid TAYEFEH GHALEHBEYGI

Place and Date of Birth: Urmia/ Iran 22.05.1984

Permanent Address: Ataturk Cad. 137 Sok No:6/19 Sisli/Istanbul Turkey

Universities and
Colleges attended: **M.Sc.** Electronic Engineering, Istanbul Technical University
B.Sc. Electronic Engineering, Urmia University

Publications:

- Omid Tayefeh Ghalehbeygi, V. Kara, L. Trabzon, S. Akturk, H. Kizil, ”Fabrication and Characterization of Si Nano-columns by Femtosecond Laser,” Journal of Nano Research Vol. 16, pp.15-20, 2011. (ISI)